NON-ION CHANNEL PROTEIN-MEDIATED SONOGENETICS

WU YONG

PhD

The Hong Kong Polytechnic University

2026

The Hong Kong Polytechnic University

Department of Biomedical Engineering

Non-ion channel protein-mediated sonogenetics

WU Yong

A thesis submitted in partial fulfillment of the requirements for

the degree of Doctor of Philosophy

Aug, 2025

CERTIFICATE OF ORIGINALITY

I hereby declare that this thesis is my own work and that, to the best of my knowledge and belief, it reproduces no material previously published or written, nor material that has been accepted for the award of any other degree or diploma, except where due acknowledgment has been made in the text.

_____(Signed)

____WU Yong_____(Name of student)

ACKNOWLEDGMENTS

The completion of this doctoral dissertation would not have been possible without the guidance, support, and encouragement of many individuals. To all who have contributed to this journey, I extend my deepest gratitude.

First and foremost, I am profoundly grateful to my supervisor, Professor Sun Lei, for his exceptional expertise, rigorous scholarship, and unwavering passion for science, which have been a constant source of inspiration. Throughout my doctoral research, his insightful guidance and patience consistently helped me overcome challenges and find clarity in moments of uncertainty. I would also like to express my sincere appreciation to Dr. Guo Jinghui for her invaluable advice and steadfast support. Her thought-provoking discussions not only enriched this work but also made the research process deeply rewarding.

I am deeply indebted to Dr. Ruan Yechun from our department for her generous assistance in facilitating the research platform. My thanks also go to the Laboratory Animal Center of The Hong Kong Polytechnic University for providing essential resources.

I would like to acknowledge my senior colleagues, Dr. Xian Quanxiang and Dr. Jiang Yizhou, for their insightful suggestions throughout my research. I am also grateful to Dr. Su Min for his technical expertise and support with experimental equipment. Special thanks go to my juniors, Liu Langzhou, Chen Congmin, and Shashwati Kala, for their assistance in experiments and manuscript revisions. Their companionship made this demanding journey far more joyful. To all those not mentioned here but who have supported me in countless ways, I offer my heartfelt thanks.

Finally, and most importantly, I owe an immeasurable debt of gratitude to my parents for their unconditional love, which enabled me to pursue higher education without hesitation. My deepest appreciation goes to my wife, Xu Zhiyi, and my son, Wu Yang, for their endless patience, understanding, and unwavering support during the most challenging phases of this endeavor.

WU Yong

July 29, 2025

ABSTRACT

The advancement of neuromodulation technologies has significantly enhanced our understanding of brain function and provided novel approaches for intervening neuronal activity in treating neurological disorders. In recent decades, various techniques including electrical stimulation, magnetic modulation, optogenetics, and chemogenetics have emerged. However, these methods present limitations in terms of invasiveness, precision, or tissue penetration depth.

Ultrasound (US) neuromodulation has emerged as one of the most rapidly developing technologies due to its non-invasive nature, high spatiotemporal resolution, and deep tissue penetration capability, finding applications in both disease research and therapeutic interventions. Sonogenetics—an innovative neuromodulation approach that genetically modifies specific cells (e.g., neurons) with ultrasound-sensitive elements (e.g., mechanosensitive channels) to enable non-invasive manipulation of target cell activity through external ultrasound—has further improved its precision. Nevertheless, the expression of exogenous ion channels in neurons may potentially alter their intrinsic electrophysiological properties, necessitating the development of alternative strategies.

This study proposes a novel ion channel-independent sonogenetic strategy utilizing the cell adhesion molecule E-cadherin as a new mediator for ultrasound-responsive neural modulation. Our key findings include: 1) Through systematic screening, we first identified E-cadherin as a highly efficient US sensor; 2) Mechanistic studies revealed that E-cadherin-mediated sonogenetic effects depend on Piezo1 channels; 3) Demonstrated that E-cadherin expression significantly enhances ultrasound-evoked calcium responses and c-fos induction in primary neurons; 4) *In vivo* experiments showed that targeted E-cadherin expression in mouse motor cortex induces ultrasound-dependent calcium transients and contralateral limb tremors; 5) Expression E-cadherin in D1 neurons of the

DMS elicits robust motor behaviors; uncovering a cooperative mechanotransduction mechanism between adhesion molecules and ion channels.

This work establishes the first non-ion channel protein-based sonogenetic approach, circumventing the limitations associated with neuronal exogenous expression of mechanosensitive ion channels while maintaining high spatiotemporal precision and biosafety. Our findings expand the current sonogenetics toolkit and pave the way for developing innovative neural modulation strategies.

Keywords Ultrasound, Neuromodulation, Sonogenetics, Non-ion-channel protein, E-cadherin, Mechanotransduction.

PUBLICATIONS ARISING FROM THE THESIS

Journal publications

1. **Wu Y**, Zhao X, Jiang Y, Chen C, Liu L, Hou X, Xian Q, Guo J, Sun L. Microbubble-enhanced ultrasound stimulation of β-cells improves insulin release and glycemic control in mice. J Nanobiotechnology. 2025 Dec 16. doi: 10.1186/s12951-025-03926-6. Epub ahead of print. PMID: 41402805.
2. Guo J, **Wu Y***, Gong Z, Chen X, Cao F, Kala S, Qiu Z, Zhao X, Chen JJ, He D, Chen T, Zeng R, Zhu J, Wong KF, Murugappan S, Zhu T, Xian Q, Hou X, Ruan YC, Li B, Li YC, Zhang Y, Sun L. Photonic Nanojet-Mediated Optogenetics. Adv Sci (Weinh). 2022 Apr;9(12):e2104140. doi: 10.1002/advs.202104140. Epub 2022 Feb 20. Erratum in: Adv Sci (Weinh). 2022 Sep;9(27):e2204667. doi: 10.1002/advs.202204667. PMID: 35187865; PMCID: PMC9036029. (*co-first author) **(*co-first author)**
3. **Yong W**, He D, Chen T, Rui Z, Wen Y, Wong KF, Sun L, Qi X, Guo J. Activation of N-Methyl-D-aspartate receptor contributed to the ultrasonic modulation of neurons in vitro. Biochem Biophys Res Commun. 2023 Oct 8;676:42-47. doi: 10.1016/j.bbrc.2023.07.034. Epub 2023 Jul 17. PMID: 37481942.
4. **Wu Y**, Que Y, Chen J, Sun L, Guo J, Ruan YC. CFTR Modulates Hypothalamic Neuron Excitability to Maintain Female Cycle. Int J Mol Sci. 2023 Aug 8;24(16):12572. doi: 10.3390/ijms241612572.
5. Sun M*, **Wu Y***, Yuan C, Lyu J, Zhao X, Ruan YC, Guo J, Huang WQ, Chen H. Androgen-induced upregulation of CFTR in pancreatic β-cell contributes to hyperinsulinemia in PCOS model. Endocrine. 2023 Nov 3. doi: 10.1007/s12020-023-03516-2. **(*co-first author)**

6. Zhu T, Guo J, **Wu Y**, Lei T, Zhu J, Chen H, Kala S, Wong KF, Cheung CP, Huang X, Zhao X, Yang M, Sun L. The mechanosensitive ion channel Piezo1 modulates the migration and immune response of microglia. iScience. 2023 Jan 16;26(2):105993. doi: 10.1016/j.isci.2023.105993.
7. Xue-Lian Zhang, Xinyi Zhao, **Yong Wu**, Wen-qing Huang, Jun-jiang Chen, Peijie Hu, Wei Liu, Yi-Wen Chen, Jin Hao, Rong-Rong Xie, Hsiao Chang Chan, Ye Chun Ruan, Hui Chen, Jinghui Guo#. Angiotensin (1–7) activates MAS-1 and upregulates CFTR to promote insulin secretion in pancreatic β-cells: the association with type 2 diabetes. Endocrine Connection. 2022 Jan 11;11(1):e210357. doi: 10.1530/EC-21-0357.
8. Chun Yuan*, Wen Qing Huang*, Jing Hui Guo*, Xing Yan Liu, Jian Zhi Yang, Jun Jiang Chen, **Yong Wu**, Ye Chun Ruan, Jia Yin Liu, Yu Gui Cui, Fei Yang Diao#, Hsiao Chang Chan# Involvement of kisspeptin in androgen-induced hypothalamic endoplasmic reticulum stress and its rescuing effect in PCOS rats Biochim Biophys Acta Mol Basis Dis. 2021 Dec 1;1867(12):166242.
9. Quanxiang Xian, Zhihai Qiu, Suresh Murugappan, Shashwati Kala, Kin Fung Wong, Danni Li, Guofeng Li, Yizhou Jiang, **Yong Wu**, Min Su, Xuandi Hou, Jiejun Zhu, Jinghui Guo, Weibao Qiu, Lei Sun Modulation of deep neural circuits with sonogenetics. Proc Natl Acad Sci U S A 2023 May 30;120(22):e2220575120. doi: 10.1073/pnas.2220575120. Epub 2023 May 22.
10. Jiejun Zhu, Quanxiang Xian, Xuandi Hou, Kin Fung Wong, Tingting Zhu, Zihao Chen, Dongming He, Shashwati Kala, Suresh Murugappan, Jianing Jing, **Yong Wu**, Xinyi Zhao, Danni Li, Jinghui Guo, Zhihai Qiu, Lei Sun The mechanosensitive ion channel Piezo1 contributes to ultrasound neuromodulation Proc Natl Acad Sci U S A. 2023 May 2;120(18):e2300291120. doi: 10.1073/pnas.2300291120. Epub 2023 Apr

25.

11. Tianting Zhong, Zhihai Qiu, **Yong Wu,** Jinghui Guo, Huanhao Li, Zhipeng Yu, Shengfu Cheng, Yingying Zhou, Jiejun Zhu, Jie Tian, Lei Sun, Puxiang Lai Optically Selective Neuron Stimulation with a Wavefront Shaping-Empowered Multimode Fiber. Advanced Photonics Research 3 (3), 2100231

Articles under review

1. **Yong WU**, Congmin CHEN, Langzhou LIU, Yizhou JIANG, Min SU, Quanxiang XIAN, Dongshuai ZHAO, Zihao CHEN, Jinghui GUO, Lei SUN. Non-ion channel protein mediated-sonogenetics.

Conference presentations

1. Dr. Hanna LU, Prof. Lei SUN, Prof. Zhihai Qiu, Prof. Yuping Ning, Prof. Zhen YUAN. 1st Meeting of Neuromodulation Society in Great Bay Area, Zhuhai, China, 2024/06/07-08. **(Poster)**
2. Yong WU, Congmin CHEN, Langzhou LIU, Yizhou JIANG, Min SU, Quanxiang XIAN, Dongshuai ZHAO, Zihao CHEN, Jinghui GUO, Lei SUN. Non-ion channel protein mediated sonogenetics. Focused Ultrasound Neuromodulation Conference FUN25, HongKong, China, 2025/07/08-09. **(Poster Pitch)**

Awards

1. The winners of the Best Teaching Assistant Award of 2022/23 Sem 1.
2. The winners of the Best Teaching Assistant Award of 2023/24 Sem 1.

TABLE OF CONTENT

LIST OF FIGURES

INDEX OF ABBREVIATIONS

Deep brain stimulation	DBS
Transcranial direct currents stimulation	tDSC
Transcranial magnetic stimulation	TMS
Transcranial focused ultrasound stimulation	tFUS
Transcranial alternating current stimulation	tACS
Subthalamic nucleus	STN
Globus pallidus internus	Gpi
Food and Drug Administration	FDA
Channelrhodopsin-2	ChR2
Clozapine-N-oxide	CNO
Designer Receptors Exclusively Activated by Designer Drugs	DREADDs
High - intensity focus ultrasound	HIFU
Sonodynamic therapy	SDT
Microelectromechanical ultrasound stimulation systems	MEMS
Mechanosensitive channels	MSCs
Low - intensity focus ultrasound	LIFU
Somatosensory evoked potential	SSEP
Frontal eye field	FEF
Magnetic resonance-guided focused ultrasound	MRgFUS
Extracellular matrix	ECM
G protein-coupled receptors	GPCRs
Phospholipase C	PLC
Control	Ctrl
Vascular endothelial growth factor receptors	VEGFRs

Cytochalasin D	CD
Microtubule-associated protein 2	MAP-2
Dulbecco's Modified Eagle Medium	DMEM
Fetal bovine serum	FBS
Electromyograms	EMG
Phosphate-buffered saline	PBS
Radioimmunoprecipitation assay	RIPA
Bicinchoninic acid	BCA
Sodium dodecyl sulfate–polyacrylamide gel electrophoresis	SDS-PAGE
Tris-buffered saline with Tween	TBST
Enhanced chemiluminescence	ECL
Horseradish peroxidase	HRP
4′,6-diamidino-2-phenylindole	DAPI
Paraformaldehyde	PFA
Bovine serum albumin	BSA
Glial fibrillary acidic protein	GFAP
Ionized calcium-binding adapter molecule 1	Iba-1
Genetically encoded calcium indicator (green fluorescent)	GCaMP6s
Calcium/calmodulin-dependent protein kinase II alpha	CaMKIIα
Electromyography	EMG
Dopamine receptor D1-expressing neurons	D1
Chinese hamster ovary	CHO
Transient Receptor Potential Polycystin 2	TRPP2
Transient receptor potential canonical 1	TRPC1

Transient receptor potential ankyrin 1	TRPA1
Quantitative reverse transcription polymerase chain reaction	qRT-PCR
Pulse repetition frequency	PRF
Human embryonic kidney 293T cells	HEK293T
Poly-L-lysine	PLL
Multiplicity of infection	MOI
Dorsomedial striatum	DMS

CHAPTER 1 Introduction

1.1 Brain Stimulation Techniques

Brain stimulation techniques represent a critical research direction in modern neuroscience and clinical medicine, aiming to modulate neuronal activity through physical, chemical, or genetic methods to explore brain function mechanisms or treat neurological disorders. With advancements in neuroscience, various brain stimulation techniques have been developed and applied in both fundamental research and clinical practice. These techniques can be categorized by their operating principles into electrical stimulation, magnetic stimulation, optogenetics, sonogenetics, chemogenetics, and others, each with distinct advantages and limitations. An ideal brain stimulation technique should possess high spatiotemporal resolution, non-invasiveness, deep-tissue stimulation capability, and long-term safety. However, no single existing technology fully meets all these requirements.

1.1.1 Overview of Neuromodulation

The human brain consists of approximately 100 billion neurons and an even greater number of glial cells, with its function relying on intricate electrochemical signaling [1]. Disruptions in the levels of key neurotransmitters, including dopamine, glutamate, and γ-aminobutyric acid, along with neuromodulators such as somatostatin and neuropeptides, are associated with the pathogenesis of several neuropsychiatric disorders. A representative example is Parkinson's disease, which is primarily caused by the degeneration of dopaminergic neurons in the substantia nigra [2], epilepsy (dysfunction of inhibitory neurons) [3], and depression (prefrontal cortex dysfunction) [4]. Conventional treatments (e.g., pharmacological agents) often lack specificity and may

induce systemic side effects. In contrast, neuromodulation refers to the regulation of neural function through external interventions to alleviate disease symptoms. Compared to traditional methods, neuromodulation technologies enable more precise targeting of specific brain regions or neural circuits, thereby improving therapeutic efficacy while minimizing adverse effects. Currently, the primary neuromodulation approaches include electrical stimulation (e.g., Deep Brain Stimulation, DBS; transcranial direct current stimulation, tDCS; transcranial alternating current stimulation, tACS), magnetic stimulation (e.g., Transcranial Magnetic Stimulation, TMS), ultrasound stimulation (e.g., transcranial Focused Ultrasound, tFUS), optogenetics, and chemogenetics.

1.1.2 Electrical Stimulation Techniques

Electrical stimulation is one of the earliest techniques applied in neuromodulation, influencing neuronal membrane potential either directly or indirectly via electric currents to alter neuronal excitability. Based on the stimulation approach, electrical stimulation can be classified into invasive (e.g., DBS) and non-invasive (e.g., tDCS and tACS) methods (Fig. 1).

DBS utilizes stereotactic surgical methods to implant electrodes within targeted brain structures, such as the subthalamic nucleus (STN) or the globus pallidus internus (GPi). These electrodes deliver continuous high-frequency electrical stimulation, which modulates pathological neural activity [5]. Currently, this approach is approved by the U.S. Food and Drug Administration (FDA) for the treatment of Parkinson's disease, essential tremor, and refractory obsessive-compulsive disorder [6, 7]. DBS offers several advantages, including sustained therapeutic efficacy—particularly in alleviating motor symptoms (e.g., tremor, rigidity) [8]—and reversibility/adjustability compared to ablative

surgeries (e.g., pallidotomy) [9]. However, its limitations include surgical risks (e.g., hemorrhage, infection, electrode displacement) [10], strong dependence on target accuracy (misplacement may reduce efficacy or cause adverse effects such as speech impairment or mood alterations) [11], and unclear mechanisms (long-term modulation may induce neural plasticity changes) [12].

tDCS is a non-invasive neuromodulation method in which low-intensity direct current is delivered via electrodes placed on the scalp to alter cortical excitability [13]. Anodal stimulation typically enhances neuronal firing, whereas cathodal stimulation suppresses it [13]. tDCS has been widely explored for cognitive enhancement (e.g., working memory, learning capacity) [14], neurorehabilitation (e.g., post-stroke motor recovery) [15], and psychiatric disorders (e.g., depression, schizophrenia) [16-19]. Its benefits include non-invasiveness, low cost, and ease of operation, allowing combination with other therapies (e.g., cognitive training). However, tDCS effects are influenced by individual anatomical variations (e.g., brain volume, age) [20], and its long-term safety requires further investigation [21].

tACS employs sinusoidal alternating currents (typically 1–100 Hz) to modulate brain rhythms (e.g., α-waves [8–12 Hz] or γ-waves [30–80 Hz]), facilitating research on neural oscillations and cognitive functions [22, 23]. Potential applications include sleep improvement [24], memory enhancement [23], and psychiatric treatment [25]. Nevertheless, tACS mechanisms remain poorly understood, clinical evidence is limited, and outcomes are susceptible to individual baseline electroencephalographic differences [26].

Transcranial Magnetic Stimulation (TMS) utilizes the principle of electromagnetic induction to generate eddy currents in the cortical tissue via rapidly changing magnetic fields, thereby modulating neuronal activity [27]. Based on stimulation patterns, TMS can

be classified into single-pulse TMS and repetitive TMS [27]. TMS has significant clinical applications in depression (FDA-approved for treatment-resistant cases) [28, 29], chronic pain (modulation of pain-related cortical areas) [30], and stroke rehabilitation [31]. Recent advancements demonstrate that magnetic nanoparticles (e.g., iron oxide nanoparticles) can enhance neuronal sensitivity to magnetic fields [32], and mechanosensitive channels (e.g., Piezo1) have been employed to amplify magnetomechanical stimulation effects [33]. However, TMS exhibits limitations including low spatial resolution, limited penetration depth, and seizure risk (high-frequency stimulation may induce abnormal discharges) [34].

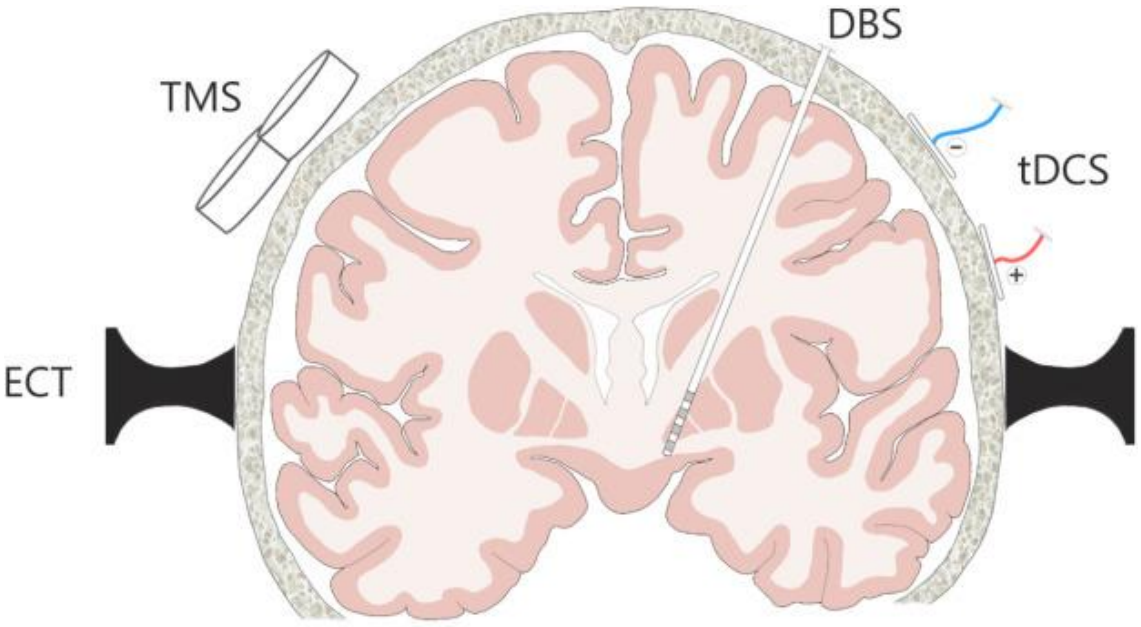

Figure 1. Electrical Stimulation Techniques. (Adapted from[35])

1.1.3 Optogenetics

Optogenetics integrates genetic engineering with optical stimulation to achieve precise neuronal control through the expression of light-sensitive proteins (e.g., channelrhodopsin-2, ChR2) [36] (Fig. 2). This technology is widely applied in fundamental research areas such as deciphering learning and memory mechanisms

(hippocampal CA1 region) [37], investigating emotional circuits [38], and exploring sleep-wake regulation [39]. For clinical translation, optogenetics shows potential in Parkinson's disease (light-controlled STN neurons) [40], epilepsy (inhibition of hyperactive neurons) [41, 42], and vision restoration (retinal photosensitization) [43]. Nevertheless, it faces major challenges including invasiveness (requiring viral vector transfection and fiber optic implantation) [44], limited light penetration depth [45], and dependence on genetic modification.

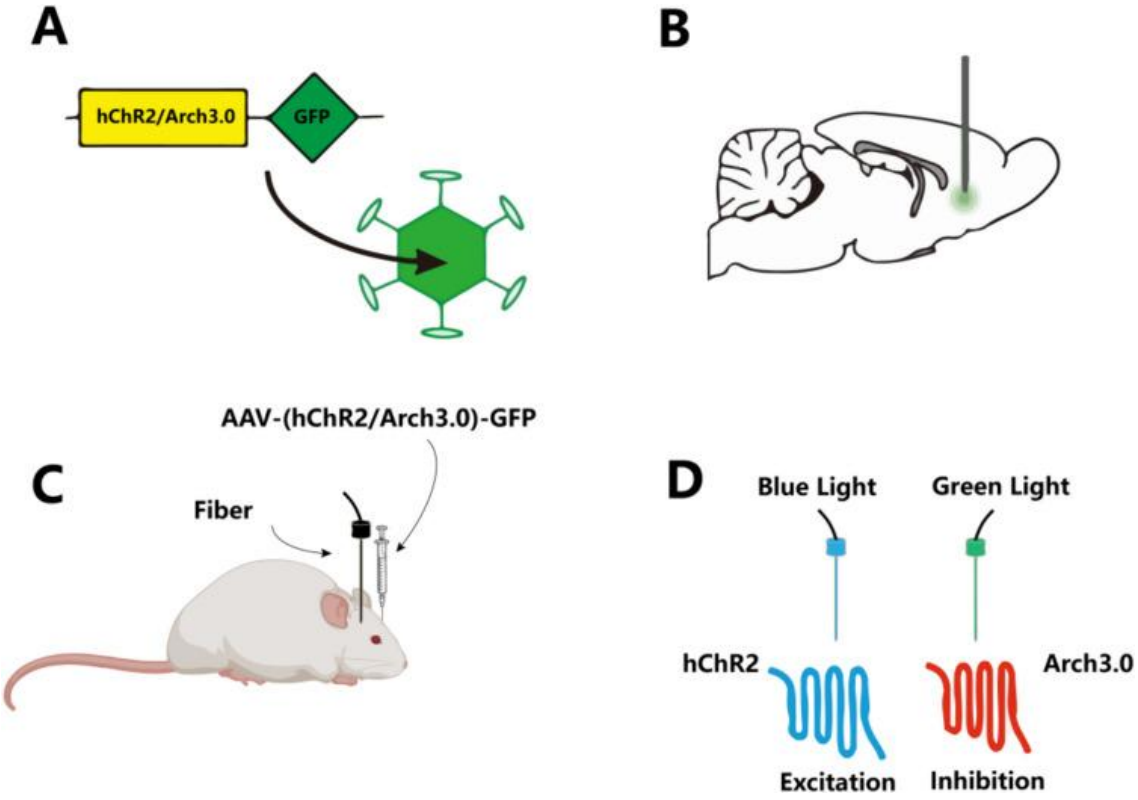

Figure 2. *In vivo* application process of optogenetics. (A) AAV delivery of GFP-fused hChR2/Arch3.0 constructs. (B) Stereotaxic vector injection for localized brain expression. (C) Fiber-optic light delivery (473 nm/532 nm) for neuronal modulation. (D) hChR2 (blue light/excitation) vs. Arch3.0 (green light/inhibition) photoresponses. (Adapted from [46])

1.1.4 Chemogenetics

Chemogenetics is a revolutionary technique that enables cell-type-specific modulation via engineered receptor-ligand systems, with its core principle being the design of artificial receptors that exclusively respond to exogenous synthetic ligands [47]. The technology operates through three key steps: (1) engineering native receptors to eliminate endogenous ligand responsiveness; (2) developing highly selective synthetic ligands (e.g., clozapine-N-oxide, CNO); and (3) triggering specific signaling pathways (e.g., Gi inhibition or Gq activation) upon ligand-receptor binding. The most established Designer Receptors Exclusively Activated by Designer Drugs (DREADDs) system has been extensively used in neuroscience research (Fig. 3), yielding breakthroughs in elucidating neural mechanisms of learning and memory [48], spatial memory encoding [49], and pathological underpinnings of mood disorders (e.g., depression and anxiety) [50]. Compared to other neuromodulation techniques, chemogenetics offers superior cell-type specificity, hardware-free operation, and suitability for long-term observation [51], though it suffers from low temporal resolution (response delays ranging from minutes to hours) [52].

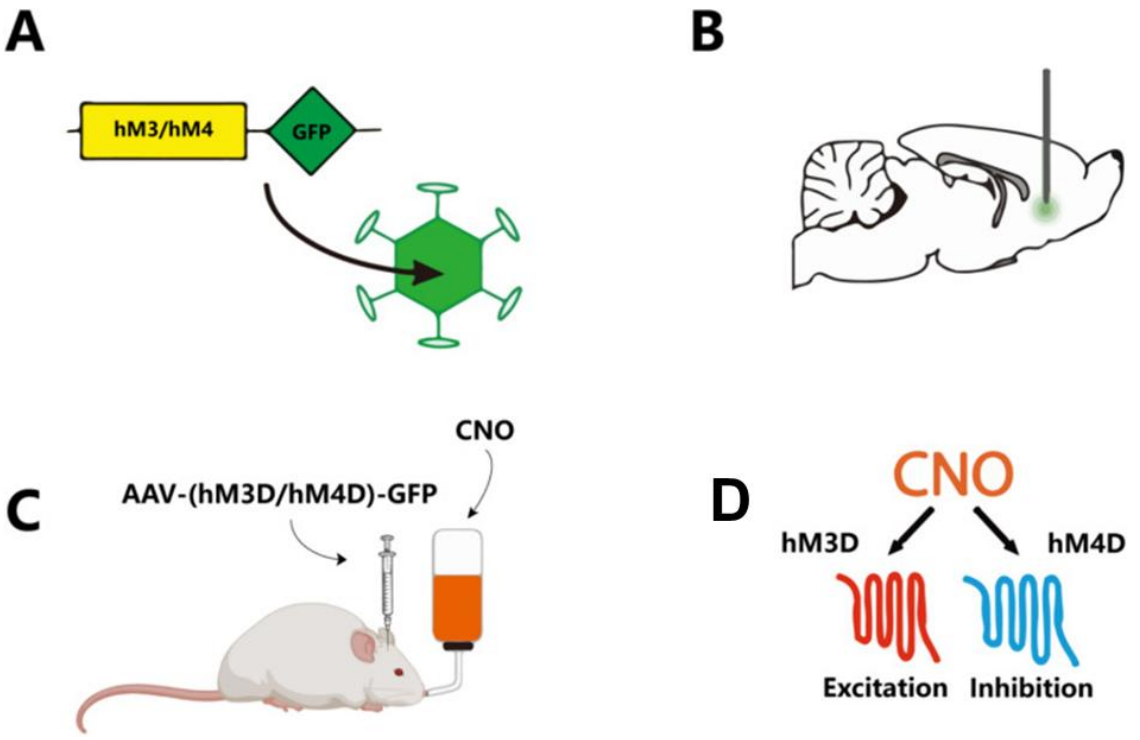

Figure 3. *In vivo* application process of chemogenetics. (A) AAV delivery of CNO-sensitive DREADDs (hM3q/hM4i) with GFP reporter. **(B)** Stereotaxic viral injection for region-specific receptor expression. **(C)** Systemic CNO administration induces targeted neuronal modulation. **(D)** CNO (hM3q/excitation) vs. CNO (hM4D/inhibition) photoresponses. (Adapted from [46])

1.1.5 Summary and Perspectives

Current brain stimulation technologies each possess unique advantages in neuromodulation. However, significant challenges remain:

- Invasiveness and safety: DBS requires craniotomy; tDCS has limited penetration depth; tACS and TMS exhibit poor spatial resolution; optogenetics necessitates fiber implantation and genetic modification; chemogenetics lacks spatiotemporal precision.
- Mechanistic understanding: The operational principles of different stimulation modalities require further exploration.

In conclusion, elucidating these multi-level regulatory mechanisms will facilitate the optimization of existing technologies and development of novel approaches. The pursuit

of non-invasive, high-precision, and deep-tissue-capable brain stimulation techniques remains a critical objective in neuroscience and clinical medicine.

1.2 Ultrasound Technology

1.2.1 Biological Effects and Applications of Ultrasound Stimulation Technology

Ultrasound has been widely utilized in biomedical engineering, including conventional diagnostics [53] and drug delivery [54]. Understanding the biological effects of US is crucial for clinicians and scientists working in this field, as permanent tissue damage may occur at high exposure levels [55]. The interaction between US and biological systems primarily occurs through two fundamental mechanisms: thermal effects and non-thermal effects (Fig. 4).

Thermal Effects: When US energy propagates through tissues, it is converted into heat, leading to temperature elevation [56]. High-intensity focused ultrasound (HIFU) can induce significant temperature increases, resulting in cellular and tissue destruction. This thermal effect has been applied in cancer therapy [56], where tumor cells are ablated through localized heating [56].

Cavitation: The cavitation process involves the formation, growth, and implosion of microbubbles [57, 58]. Cavitation can be either stable or inertial. Inertial cavitation describes the process whereby bubbles undergo rapid expansion followed by violent collapse when subjected to ultrasound, generating localized high temperatures and pressures that cause cellular damage [59]. Stable cavitation, in contrast, describes controlled oscillations of bubbles within the ultrasonic field without catastrophic collapse [60]. Sonodynamic therapy (SDT) exploits cavitation effects by combining low-intensity US with sonosensitizers to produce lethal reactive oxygen species. Due to its deep tissue

penetration, high spatiotemporal selectivity, and non-invasive nature, SDT has been employed in treating deep-seated tumors and multidrug-resistant bacterial infections [61].

Mechanical Effects： The mechanical effects of US are primarily associated with the presence of gas and refer to forces and related phenomena (e.g., acoustic radiation force, acoustic streaming, and cavitation) exerted on tissues during wave propagation. These effects can enhance cell membrane permeability via sonoporation, facilitating the intracellular delivery of drugs [62], proteins, and DNA [63]. Additionally, mechanical effects have broad applications in tissue engineering [63] and material processing [64].

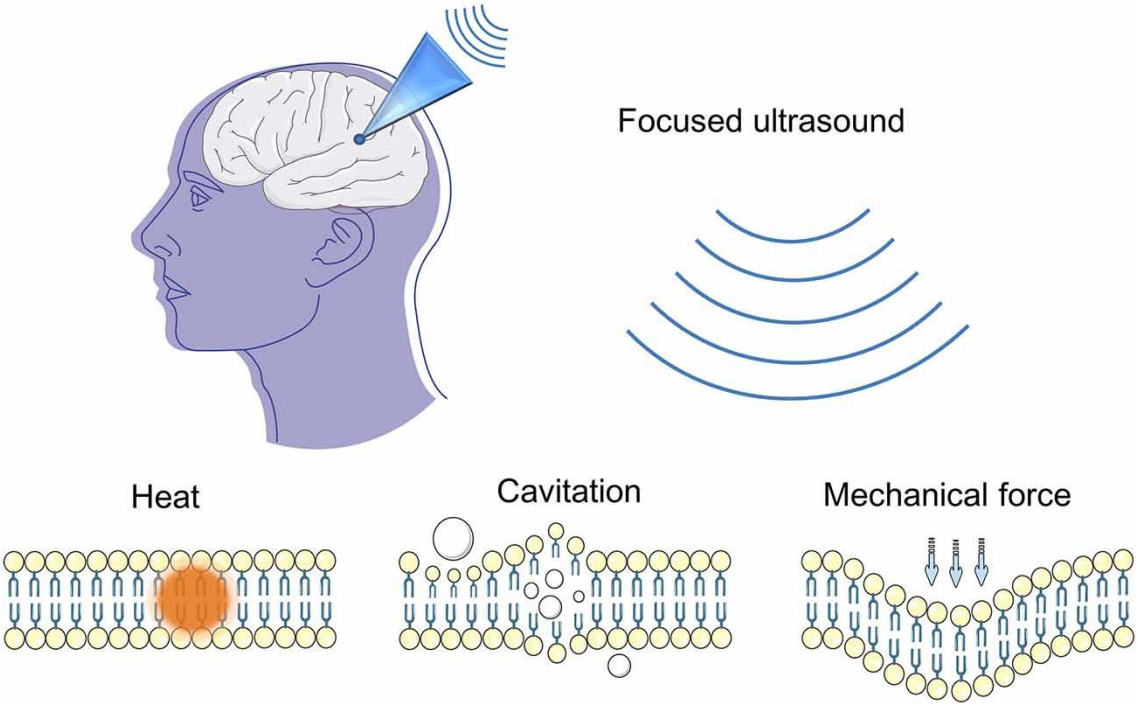

Figure 4. The biophysical effects underlying ultrasound-mediated neuromodulation Safety Considerations. (Adapted from [65])

It should be noted that ultrasound-tissue interactions may produce adverse biological effects, particularly in sensitive organs (e.g., brain, eyes, heart, lungs, and gastrointestinal tract) and embryos/fetuses [66]. Therefore, strict control of output intensity and real-time

monitoring of thermal and mechanical indices are essential to assess potential bioeffects during US applications [66, 67].

1.2.2 Ultrasonic Neuromodulation

Ultrasonic neuromodulation, as a non-invasive neuromodulation technique, has demonstrated remarkable progress in both fundamental research and clinical applications in recent years. This section systematically reviews the latest research achievements and developmental trends from three perspectives: in vitro mechanistic investigations, animal model validation, and human application studies.

In Vitro Mechanistic Exploration

In vitro studies on ultrasonic neuromodulation have achieved systematic breakthroughs in elucidating underlying mechanisms and developing novel technologies. Regarding electrophysiological properties, the seminal work by Tyler et al. (2008) first confirmed that ultrasonic pulses could induce action potentials in hippocampal CA1 neurons [68] (Fig. 5), while Khraiche et al. further demonstrated enhanced firing frequency in primary hippocampal neurons upon US exposure [69]. From a methodological perspective, microelectromechanical US stimulation systems (MEMS) have enabled subcellular-precision modulation of neural circuits [70]. At the molecular level, mechanosensitive channels (MSCs), particularly Piezo1, have been identified as core targets for US effects, effectively transducing mechanical stimuli into electrochemical signals [71]. Piezo1 activation has been validated as a critical mediator of ultrasonic neuromodulation [72]. Additionally, US can suppress neuronal activity by activating TRAAK K^+ channels through lipid membrane interactions [73].

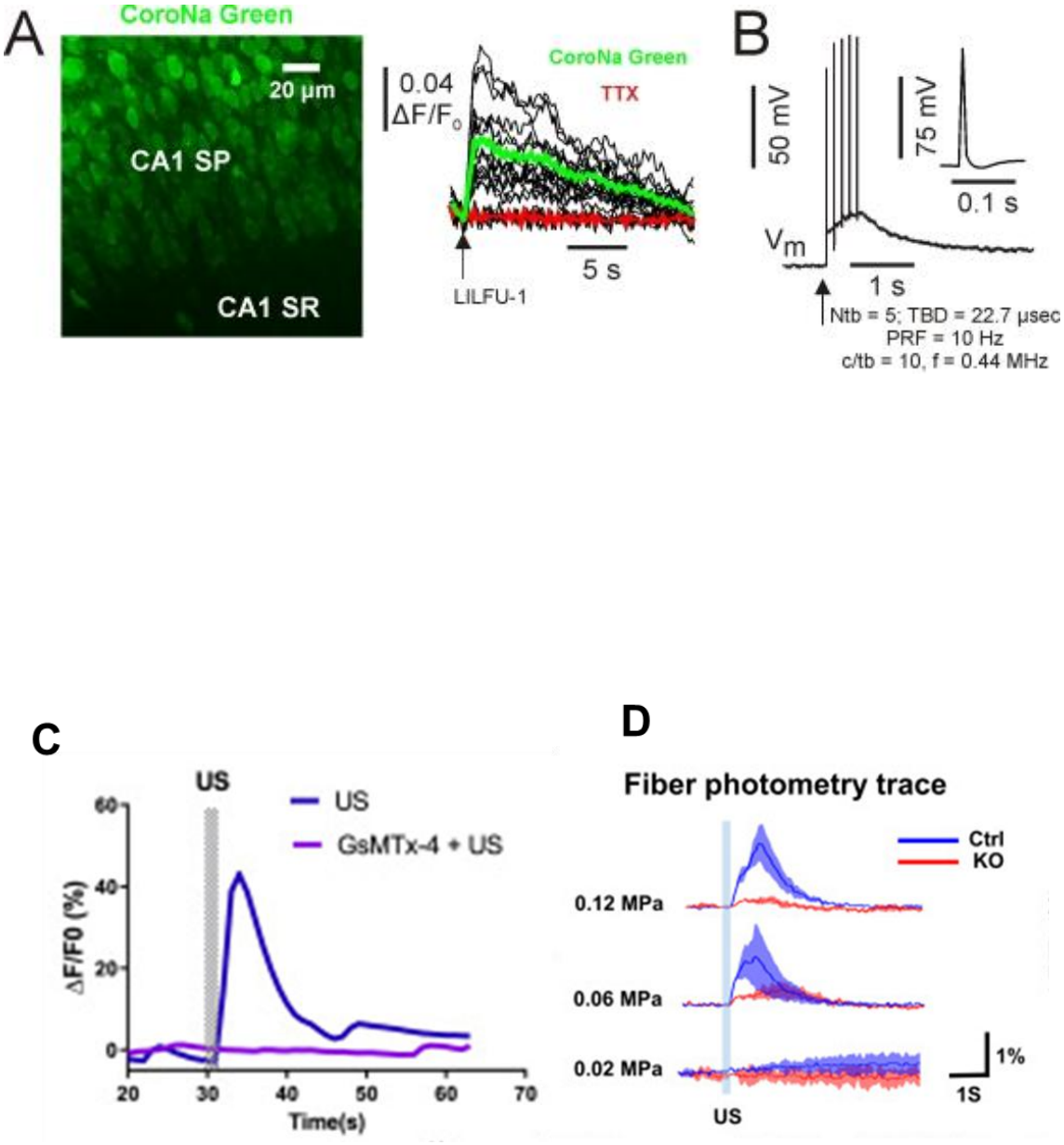

Figure 5. Voltage-gated Na^+ channels in neurons respond to LILFU stimulation (A) Confocal image (left) shows a slice culture loaded with CoroNa Green AM, highlighting hippocampal regions CA1 stratum pyramidale (SP) and stratum radiatum (SR). Na⁺ transients (right) were recorded in CA1 pyramidal neuron somas during LILFU-1 stimulation, with individual (black) and averaged (color) responses under control conditions and after TTX application. **(B)** Current-clamp recordings performed on a CA1 pyramidal neuron demonstrate alterations in membrane voltage in response to a series of five ultrasonic tone bursts delivered at a pulse repetition frequency (PRF) of 10 Hz. (Adapted from [68]) (C) Representative Ca^{2+} imaging traces showing neuronal responses to 0.45 MPa ultrasound, with or without prior

incubation in 40 μM GsMTx-4 (Adapted from [74]). (D) EMG recordings following ultrasound stimulation in control (Top) and Piezo1 KO (Bottom) mice (Adapted from[72]).

In Vivo Therapeutic Applications and Mechanistic Advances

Animal studies have played a pivotal bridging role in ultrasonic neuromodulation, with significant breakthroughs in treating neurological disorders. In stroke models, Qi et al. reported that low-intensity focused ultrasound (LIFUS) stimulation reduced infarct volume and improved neurological function scores [75]. For Parkinson's disease, The combination of LIFU and MBs disrupts the BBB to improve drug penetration, suggesting a promising avenue for PD therapy [76] (Fig. 6). Large-animal studies have provided crucial translational insights. Lee et al. (2016) first demonstrated precise brain region-specific modulation in sheep, where somatomotor cortex stimulation elicited contralateral hindlimb electromyographic responses—a specificity unattainable in rodents due to reduced acoustic interference in larger cranial cavities [77]. Dallapiazza et al. subsequently observed altered somatosensory evoked potential (SSEP) amplitudes upon ventral posterolateral thalamic nucleus stimulation in porcine models [78]. Non-human primate studies have offered unique perspectives on higher cognitive functions: Kubanek et al. found that frontal eye field (FEF) US stimulation biased choice preferences during visual decision-making tasks in macaques[79].

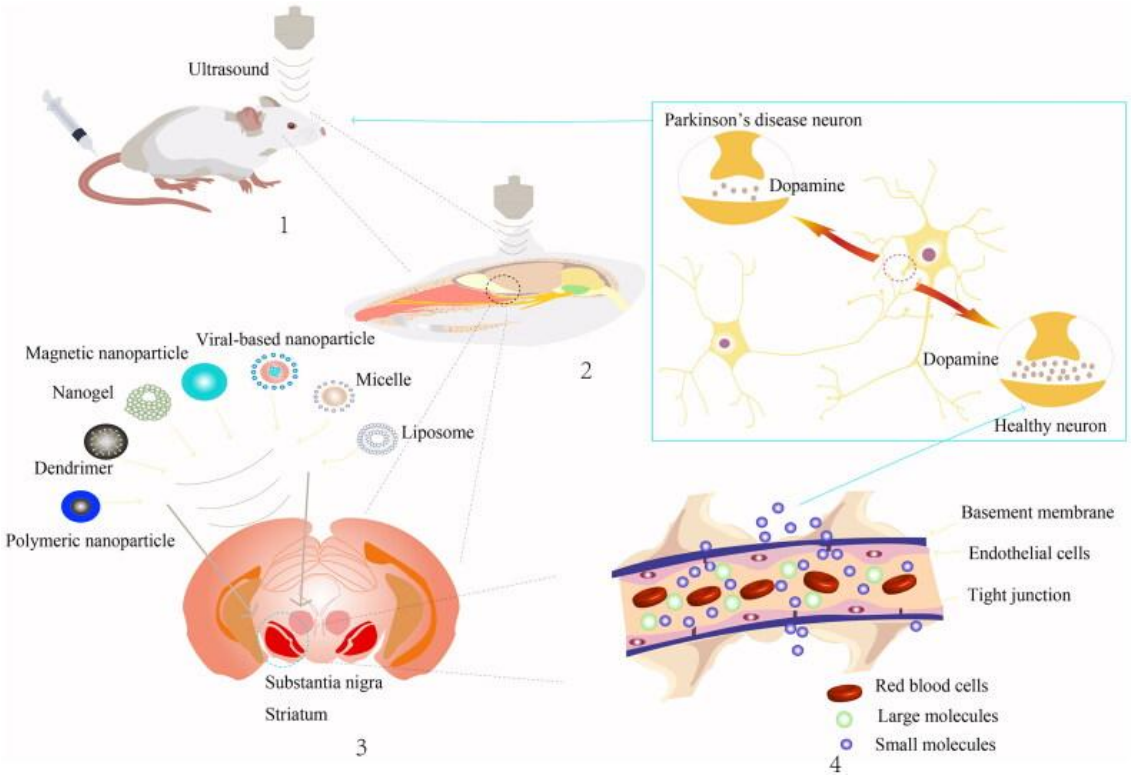

Figure 6. Therapeutic Mechanisms and Applications of LIFU in Parkinson's Disease (PD) **(1)**. BBB Modulation – LIFU, when combined with microbubbles (MBs), induces transient blood-brain barrier (BBB) opening, enabling targeted drug delivery. **(2)**. Precise Neuromodulation – LIFU selectively stimulates motor-related brain regions in mice, including the motor cortex, substantia nigra, and striatum. **(3)**. Nanocarrier-Mediated Delivery – Therapeutic agents (e.g., genes, drugs) are transported via microvesicles or nanoparticles, such as polymeric NPs, dendrimers, nanogels, magnetic NPs, viral vectors, micelles, and liposomes. **(4)**. Transport Pathways – Once the BBB is opened, drugs primarily cross via paracellular (between cells) or transcellular (through cells) routes. (Adapted from [76])

Clinical Translation and Exploratory Applications

With advancing foundational research, ultrasonic neuromodulation is progressively transitioning to clinical applications. For non-invasive brain modulation, Legon et al. (2014) pioneered the precise activation of hand motor cortex via tFUS in healthy humans [80], while Lee et al. (2016) later confirmed tFUS-induced EEG responses in the primary

visual cortex [81]. In psychiatry, Sanguinetti et al. reported improved mood and altered functional connectivity following frontal lobe US stimulation [82] (Fig. 7). For chronic pain management, US modulation of pain-related brain regions alleviated symptoms and improved mental states [83]. Notably, magnetic resonance-guided focused ultrasound (MRgFUS) has shown promising early outcomes for Parkinsonian tremor [84], marking a step toward routine clinical adoption. Current challenges center on deepening mechanistic understanding and optimizing personalized protocols. With emerging technologies like artificial intelligence, ultrasonic neuromodulation is evolving toward higher precision and greater personalization, positioning itself as a potential cornerstone for neuropsychiatric therapies.

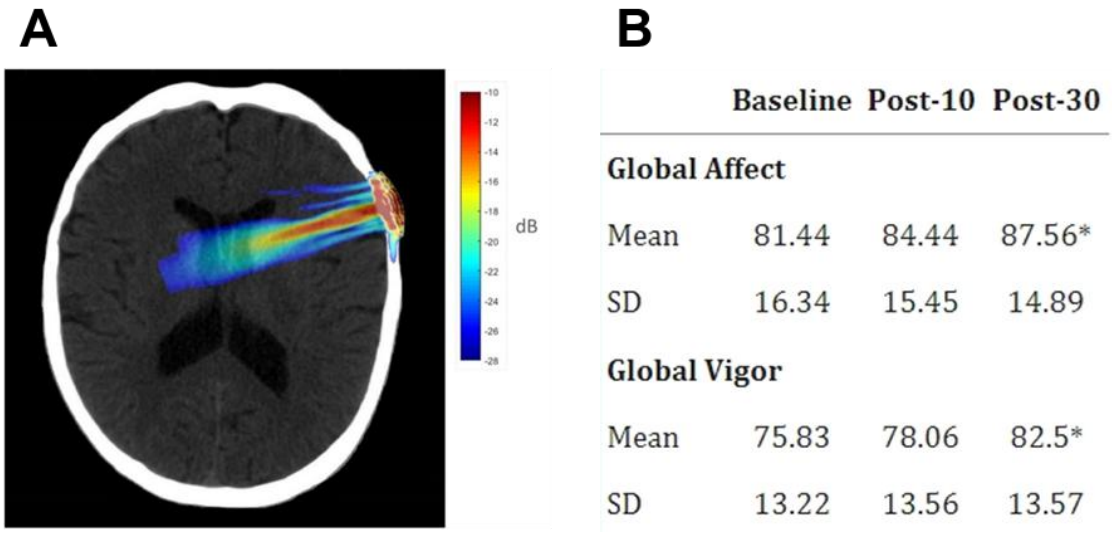

Figure 7. Transcranial US Modulation of Prefrontal Cortex Affects Mood and Connectivity in Humans. (A) Acoustic modeling using representative CT data shows transducer targeting at F8 scalp position (corresponding to rIFG). **(B)** Global Affect and Global Vigor scores. (Adapted from [82])

1.3 Mechanosensitive Ion Channels Based Sonogenetics

US stimulation, as an emerging neuromodulation technology, exhibits significant advantages over conventional methods. Compared to DBS requiring electrode implantation, optogenetics with limited tissue penetration, and TMS with relatively low spatial resolution, US enables precise neural circuit modulation through non-invasive curved transducers [85]. Its mechanisms primarily involve three physical effects: thermal effects mediated by temperature-sensitive channels [86], cavitation effects dependent on microbubble oscillations [74], and mechanical forces transduced by MSCs [84] (Fig. 8A, B). Studies reveal that cortical neurons exhibit heightened US sensitivity via Transient Receptor Potential Polycystin 2 (TRPP2) and Transient receptor potential canonical 1 (TRPC1) channels [87], providing critical guidance for sonogenetic target selection.

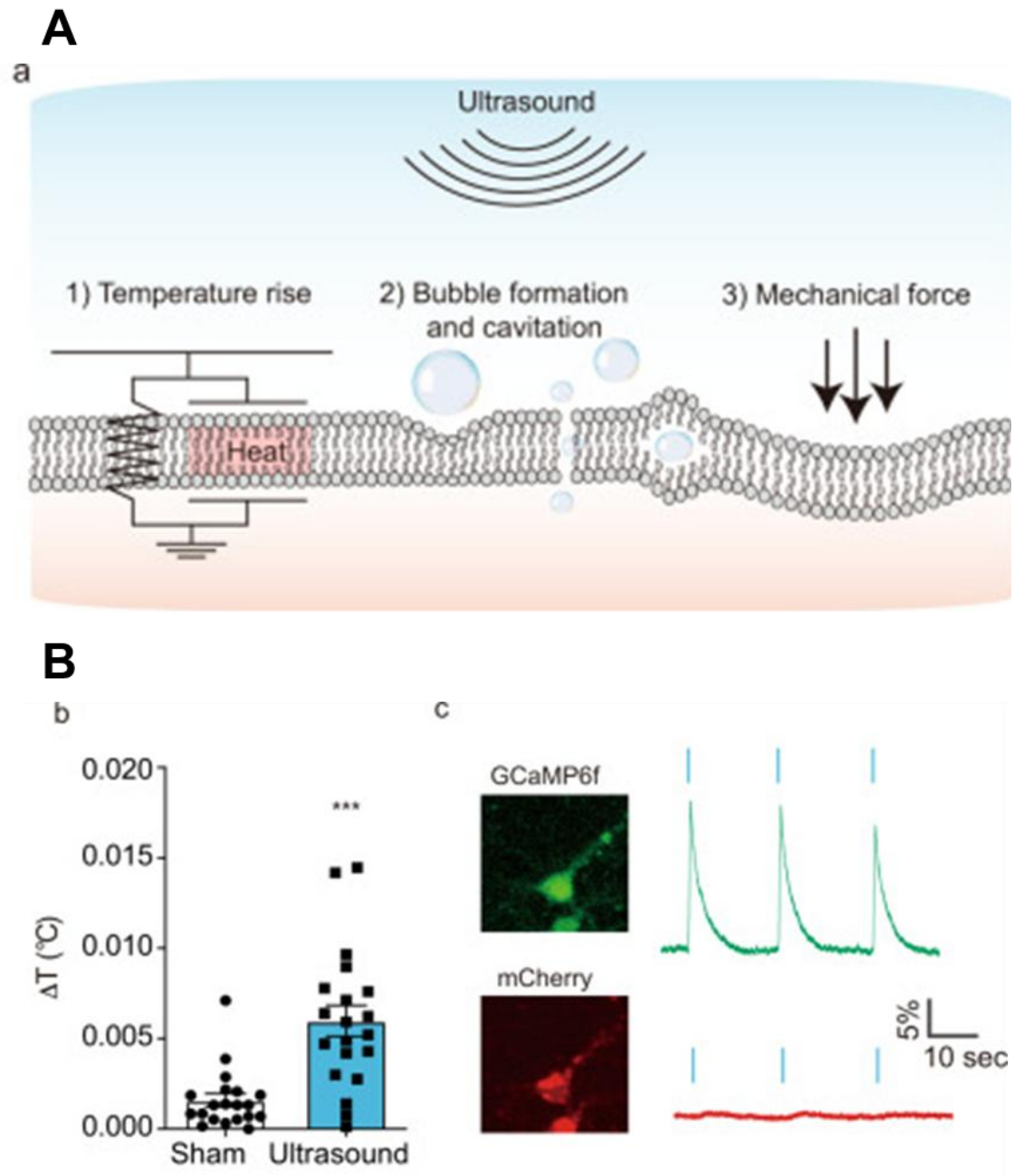

Figure 8. US triggers neuronal responses by mechanical perturbation. (A) Diagram summarizing ultrasound-mediated biophysical interactions. **(B)** Optic hydrophone thermometry detected localized heating during sonication (parameters: 15 W/cm², 500 ms pulses, 20 s intervals; n = 20; two-tailed unpaired t-test, ***p < 0.0001). (Adapted from [87])

Sonogenetics employs genetic engineering to express MSCs in specific neurons for ultrasound-selective responsiveness. The pioneering work by Ibsen et al. (2015) first

demonstrated ultrasound-induced behavioral modulation by expressing TRP-4 channels in Caenorhabditis elegans [88]. The protocol involves: (1) cloning target channel genes into viral vectors; (2) delivering vectors via stereotaxic injection for region-specific transduction; (3) applying LIFUS; and (4) evaluating neural activity and behavior [88]. Multiple MSCs with sonogenetic potential have been identified, including Piezo1 [74], TRPM4, TRPP1/2, TRPC1 [87], mPrestin [89], MscL [90, 91], TREK-1/2[92], TRAAK [73, 92, 93], and human sensitive Transient receptor potential ankyrin 1 (hsTRPA1) [94] (Fig. 9A, B). For instance, hsTRPA1 expression in layer V motor cortical neurons enhanced ultrasound-evoked contralateral limb responses and c-Fos activation [94]. Additionally, thermosensitive TRPV1 has been utilized to amplify neuronal sensitivity to US thermal effects [86]. These discoveries advance precision neuromodulation tool development.

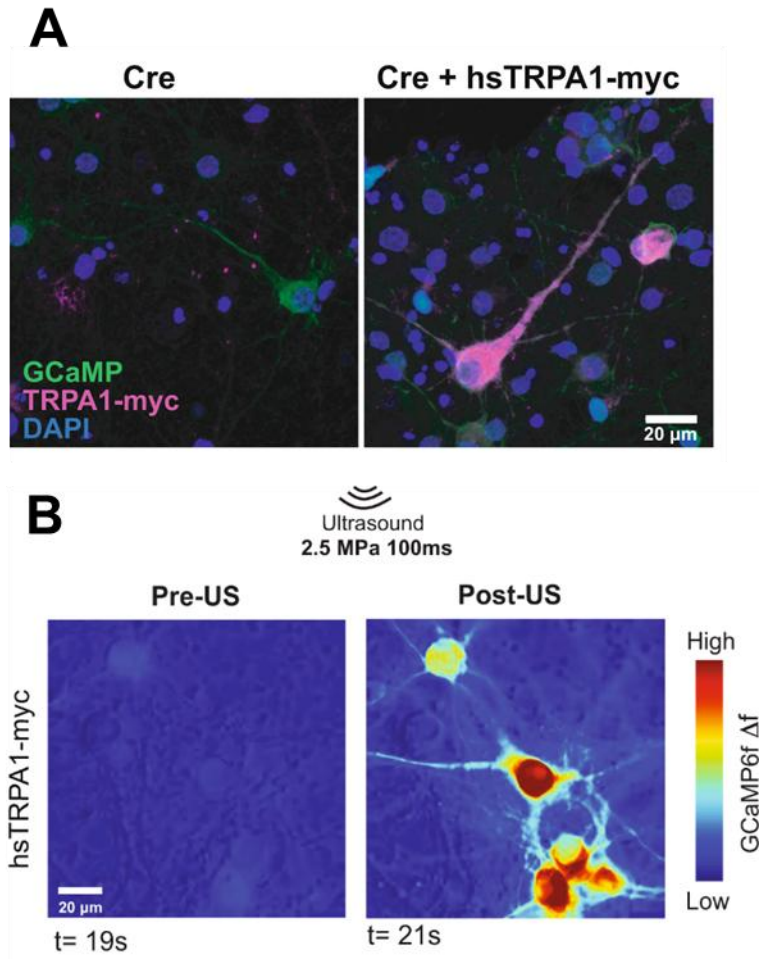

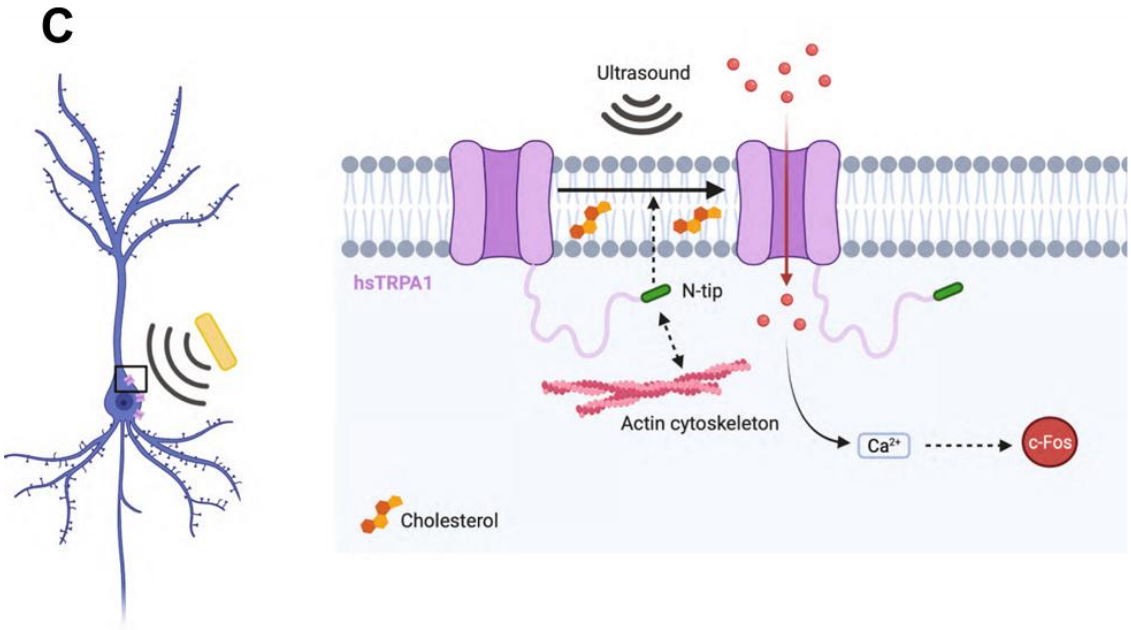

Figure 9. hsTRPA1 enhances calcium signaling and ultrasound-evoked neuronal firing in primary rodent neurons (*in vitro*). (A) Cultured mouse primary neurons (DIV 12) transfected with hsTRPA1 or control constructs. **(B)** Ultrasound-triggered calcium dynamics in hsTRPA1-expressing neurons, visualized by GCaMP6f fluorescence. Graphs depict peak response amplitudes following stimulation. **(C)** Proposed mechanism of hsTRPA1-mediated neuronal activation by ultrasound, highlighting the essential roles of the N-terminal domain, actin cytoskeleton, and cholesterol in promoting ultrasound-evoked calcium influx, neuronal excitation, and c-fos expression (Adapted from [87])

1.4 Non-Ion Channel Mechanosensitive Proteins

Mechanosensitive proteins are defined as proteins capable of responding to mechanical stimuli and transducing them into biological signals. These proteins play crucial roles in various physiological processes including tactile sensation, hearing, osmoregulation, and cell differentiation [95, 96]. Beyond ion channel-type mechanosensitive proteins, there exists another category of non-ion channel mechanosensitive proteins that perceive and respond to mechanical forces through distinct mechanisms.

Integrins represent a prominent class of non-ion channel mechanosensitive proteins. As extracellular matrix (ECM) receptors, integrins mediate cell-ECM adhesion and play pivotal roles in cellular signal transduction by activating multiple pathways such as FAK and MAPK signaling cascades [97]. Through their connection with the cytoskeleton, integrins can transmit mechanical forces into the cell interior, thereby influencing cell morphology, migration, and gene expression [95]. Among various integrins, integrins β2 are particularly important in cell adhesion, migration, and signal transduction, especially in immune cells. Integrins β2 are transmembrane receptors expressed on leukocyte surfaces that mediate both cell-cell and cell-ECM interactions [98]. In quiescent neutrophils, mechanical forces generated by approximately 200 high-affinity integrins β2 bond clusters have been shown to be sufficient to trigger Ca^{2+} influx, suggesting that the magnitude of fluid drag forces can be mechanically transduced into signals that enhance neutrophil recruitment and effector functions [99] (Fig. 10A, B). The cytoskeleton, particularly actin filaments and microtubules, interacts with integrins β2 to collectively regulate cellular mechanosensitive [100]. In summary, integrins β2 respond to mechanical stimulation through multiple mechanisms involving integrin conformational changes, intracellular signaling, cytoskeletal reorganization, and crosstalk with other signaling pathways. These processes are fundamentally important for regulating cell adhesion, migration, and functionality.

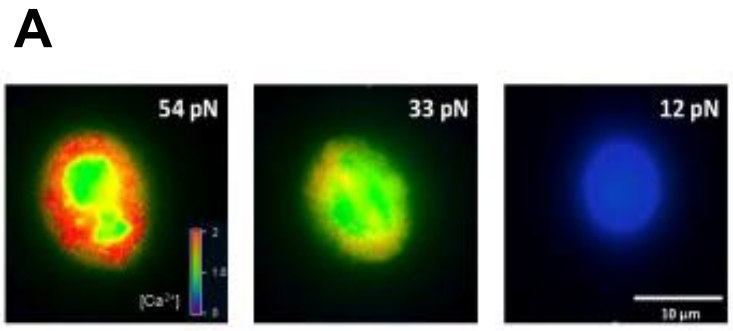

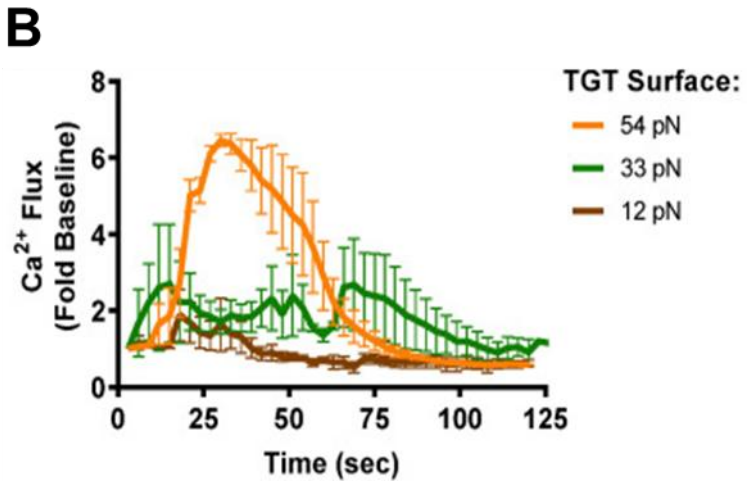

Figure 10. Neutrophil Ca^{2+} signaling dynamics are regulated by HA β2-integrin bond tension. (A) Representative fluorescence images of neutrophils subjected to shear flow on TGT substrates coated with the β2-integrin activator CBR LFA1/2. Intracellular Ca^{2+} was monitored using Fura-2 (scale bar: 10 μm). **(B)** Time-dependent changes in Ca^{2+} levels (normalized to baseline, no shear) under increasing shear stress (0–1 dyn/cm²). Data represent fold-change over initial Ca^{2+} levels (mean ± SEM, n = 3 experiments, >10 cells per field, 7 fields analyzed). A significant difference ($p < 0.01$) was observed between 54 pN and 33/12 pN conditions from 24–48 s. (Adapted from [99])

GPCRs represent a crucial class of transmembrane receptors that activate intracellular signaling pathways upon binding extracellular ligands [101, 102]. GPR68, a member of the GPCR family, plays a pivotal role in vascular biology, particularly in flow-mediated vasodilation. Endothelial GPR68 is essential for shear stress responses [103] and its deficiency leads to vascular dysfunction, impairing blood flow-mediated outward arterial remodeling [103] (Fig. 11). Mechanical stimulation of GPR68 triggers Gq protein-mediated activation of phospholipase C (PLC), modulating intracellular Ca^{2+} levels and ultimately regulating cellular functions [104]. Additionally, GPR68 participates in metabolic regulation and mitochondrial function [105] . In summary, as a multifunctional mechanosensitive receptor, GPR68 senses

mechanical forces and orchestrates intracellular signaling pathways, exerting critical roles in vascular physiology, tumor biology, osteoarthritis, and other physiological/pathological processes.

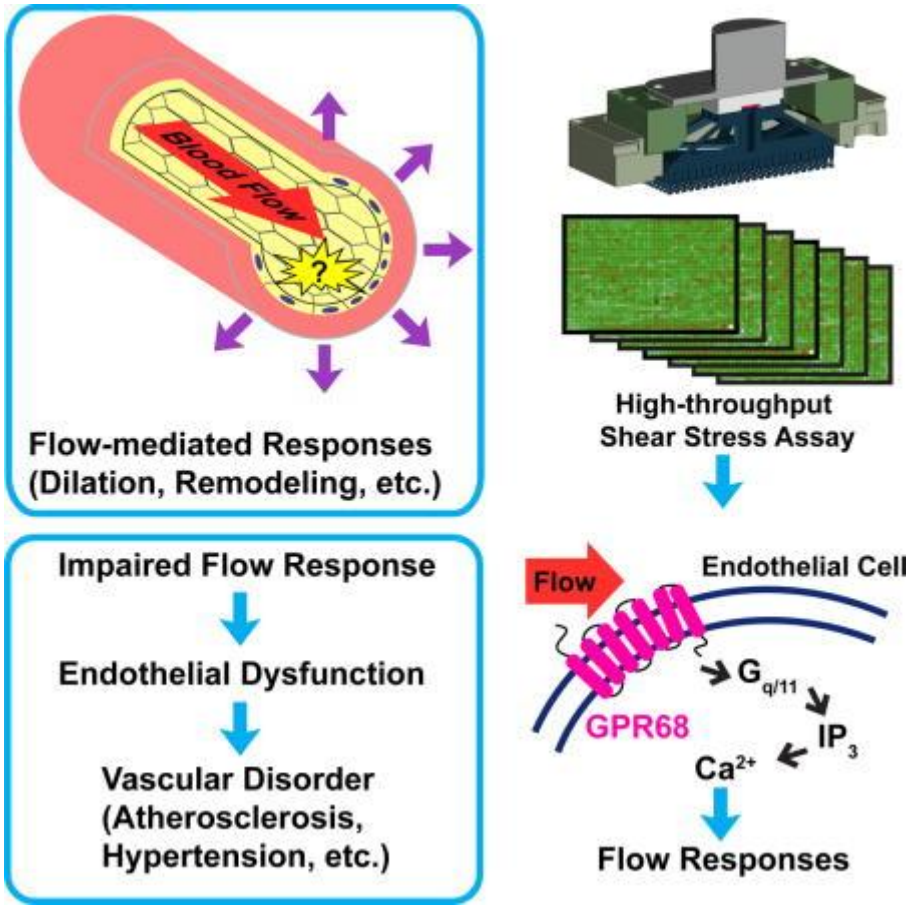

Figure 11. GPR68 responds to fluid shear stress and is essential for normal vascular physiology. (Adapted from [103])

Vascular endothelial growth factor receptors (VEGFRs) represent a critical class of tyrosine kinase receptors that play pivotal roles in angiogenesis and lymphangiogenesis. These receptors and their associated signaling pathways occupy a central position in vascular biology and serve as important therapeutic targets for various diseases. Research has demonstrated that VEGFR2 functions as the primary receptor for VEGF-A, transmitting major pro-angiogenic signals through its potent tyrosine kinase activity [106]. The binding between VEGF-A and VEGFR2 constitutes the principal driving force

behind angiogenesis [107]. Activation of VEGFR2 induces endothelial cell proliferation, migration, and survival - all essential processes during blood vessel formation [108]. However, Emerging evidence indicates that mechanical stimuli modulates both VEGFR2 expression and activation [109-113] (Fig. 12). VEGFR2 plays a crucial role in cellular signal transduction, with its response to mechanical stimulation involving complex molecular mechanisms and activation of multiple signaling pathways.

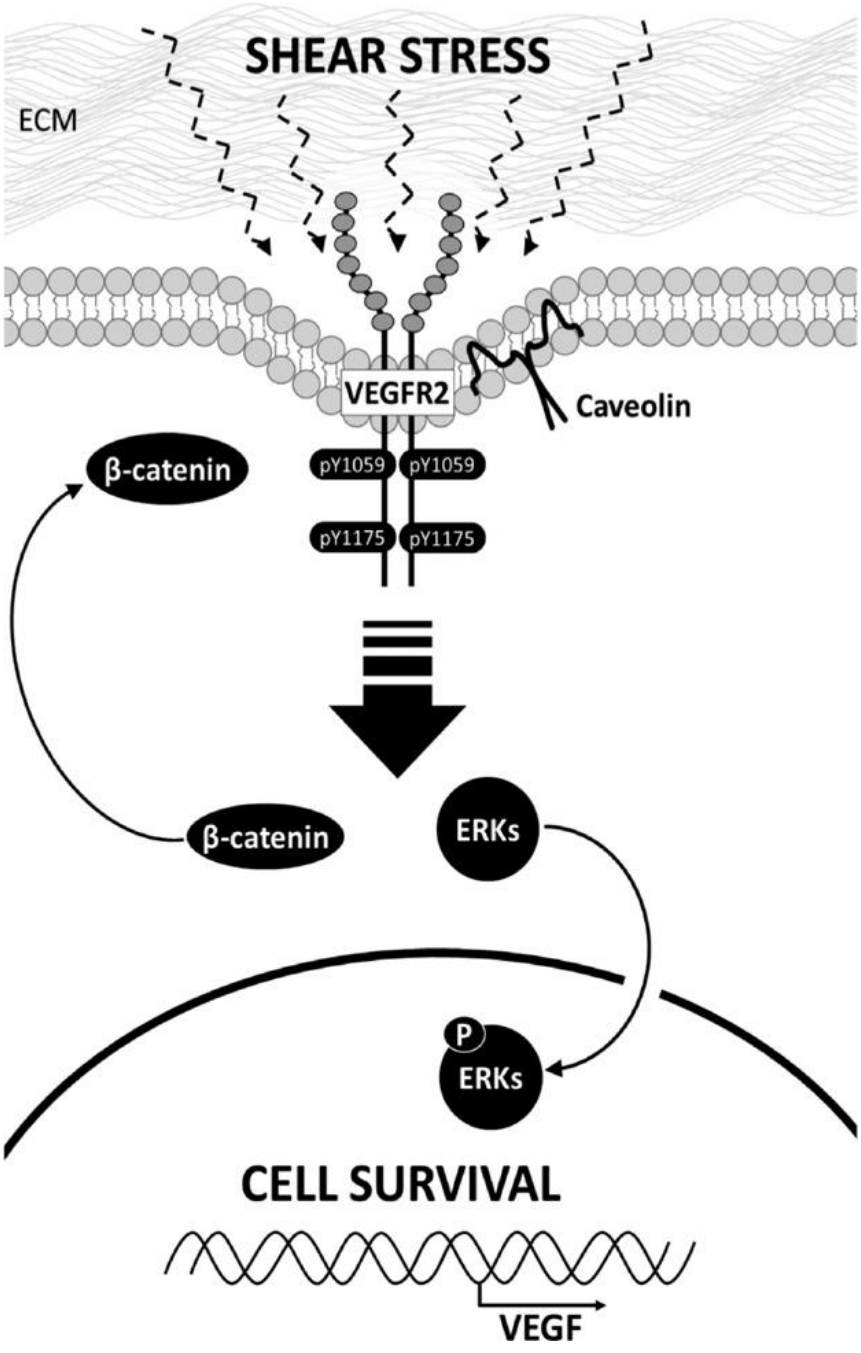

Figure 12. Fluid flow (FF)-induced shear stress promotes VEGFR2 phosphorylation within a mechanosensitive signaling complex involving caveolin-1. This cascade facilitates membrane recruitment of β-catenin and initiates ERK-dependent pro-survival signaling, ultimately upregulating VEGF expression. (Adapted from [110])

E-cadherin, a calcium-dependent transmembrane adhesion molecule predominantly localized at interepithelial junctions, plays crucial roles in cell-cell adhesion [114], tissue morphogenesis, establishment of cell polarity, and signal transduction [115, 116]. Its deficiency has been demonstrated to influence cell fate determination [117].Mechanical forces can directly modulate E-cadherin-mediated intercellular junctions, enhancing adhesive strength to enable cellular resistance to external forces [118] while facilitating cell migration processes [114, 119]. Upon mechanical stimulation, E-cadherin complexes trigger β-catenin recruitment and adhesion reinforcement through α-catenin/vinculin interactions [120] (Fig. 13). Moreover, E-cadherin is essential for maintaining epithelial integrity, with mechanical forces reinforcing tissue stability via functional regulation of E-cadherin [118]. Mechanically activated E-cadherin also initiates intracellular signaling pathways that regulate cytoskeletal remodeling [121].

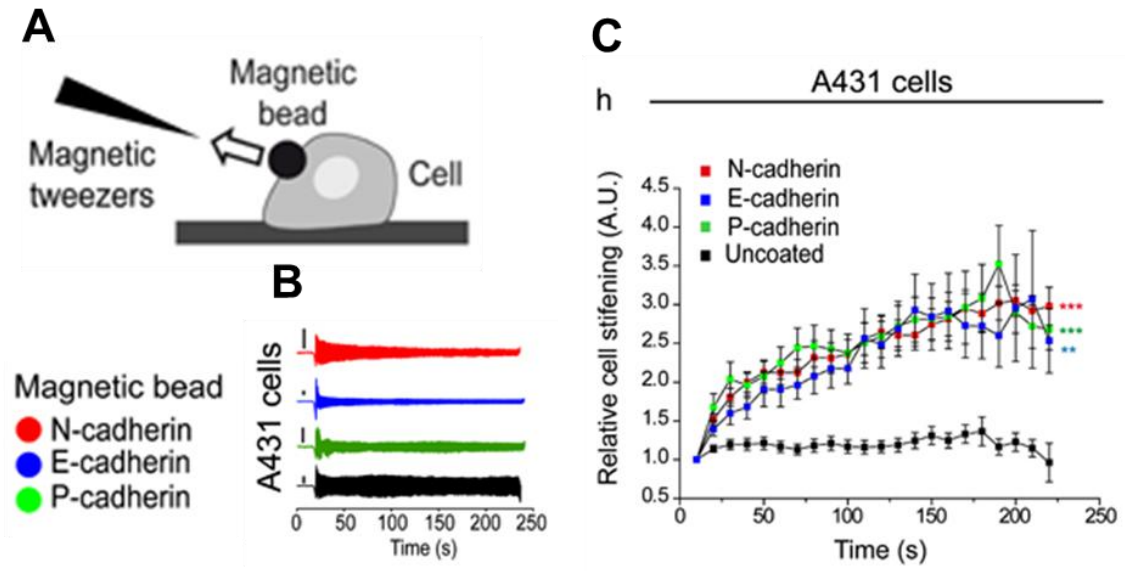

Figure 13. Heterophilic E-cadherin/N-cadherin adhesions confer mechanical resilience and initiate mechanotransduction. (A) Schematic of the magnetic tweezer assay for probing cadherin-mediated cell adhesion mechanics. **(B)** Displacement trajectories of A431 cells (Epidermoid Carcinoma) in response to force pulses applied via N-cadherin (red), E-cadherin (blue), P-cadherin (green), or control (uncoated, black) functionalized beads. Scale bar: 200 nm. **(C)** Mechanical stiffening at the A431 cell-bead interface, quantified as the time-dependent force-displacement ratio ($\Delta F/\Delta x$) normalized to baseline for N-, E-, and P-cadherin-coated beads versus uncoated controls. (Adapted from [120])

Additional mechanosensitive proteins include polycystins PC1 and PC2, whose mutations lead to polycystic kidney disease. These proteins localize to renal primary cilia, where they sense urine flow and participate in mechanotransduction [122]. In summary, non-ion channel mechanosensitive proteins play vital roles in cellular mechanosensation, contributing to diverse physiological and pathological processes.

1.5 Research Gaps

US neuromodulation has emerged as a powerful non-invasive tool for manipulating neural activity across mammalian species, its precision has been advanced by sonogenetics—a cell-type-specific approach relying on engineered MSCs. However, some specific ion channels face inevitable limitations: their ectopic overexpression may disrupt native neuronal physiology [123, 124], trigger aberrant activation [125], or exhibit restricted cellular tropism, thereby constraining therapeutic utility.

To overcome these challenges, recent studies have identified non-channel mechanosensors, such as integrin β2 [126-128], VEGFR2 [109, 129, 130], GPCR68 [103], and E-cadherin[131], that activate downstream mechanotransduction pathways without directly forming ion-conducting pores [132]. Despite their established roles in

mechanotransduction of cells, whether these non-channel mechanosensors can mediate US neuromodulation remains unexplored, presenting an untapped opportunity to expand the sonogenetic toolbox.

1.6 Research Objectives

This study aims to identify a non-channel mechanosensitive protein capable of mediating ultrasonic stimulation, with validation in primary neurons and both anesthetized and freely behaving mice. To achieve this goal, the following objectives are proposed:

1.Screening of Mechanosensitive Proteins:Calcium imaging will be employed to systematically evaluate candidate non-channel mechanosensitive proteins previously reported to sense mechanical forces, with the goal of identifying the protein demonstrating optimal responsiveness to ultrasonic stimulation.

2.Mechanistic Investigation: The underlying mechanisms by which the selected non-channel mechanosensitive protein mediate ultrasonic stimulation will be elucidated.

3.Functional Validation: Real-time effects of non-channel mechanosensitive protein-mediated ultrasonic stimulation will be assessed in primary neuronal cultures, as well as in both anesthetized and freely moving mouse models.

4.Safety Profiling: Expression patterns of the candidate protein in neurons will be characterized, and the biosafety profile of effective ultrasonic stimulation parameters will be thoroughly evaluated.

CHAPTER 2 E-cadherin is a candidate mediator molecule for sonogenetics

2.1 Materials and methods

2.1.1 Cell transfection

Human embryonic kidney (HEK) 293T cells (ATCC) were cultured in Dulbecco's Modified Eagle Medium (DMEM; Gibco) containing 10% fetal bovine serum (FBS) and 1% Penicillin-Streptomycin (Gibco), maintained at 37°C with 5% CO_2 in a humidified incubator. For transfection procedures, cells were seeded into 6-well plates at a density of 1×10^6 cells per well. After 24-hour incubation, plasmid transfection was performed using the Lipofectamine 3000 kit (Invitrogen L3000001). Specifically, 3.0 μg plasmid DNA was combined with 3 μl Lipofectamine 3000 and 6 μl P3000 reagent in Opti-MEM I Reduced Serum Medium (Gibco) to form transfection complexes, strictly following the manufacturer's protocol. These complexes were then introduced into each well. 24 hours post-transfection, cells were harvested via trypsinization and subcultured. For subsequent calcium imaging analysis, a fraction of transfected cells were replated onto glass-bottom confocal dishes (SPL Life Sciences) at 5×10^5 cells per well, allowing 24-hour adherence prior to experimentation.

The Control pcDNA3.1(+)IRES GFP (Ctrl) was a gift from Kathleen_L Collins (Addgene plasmid # 51406 ; http://n2t.net/addgene:51406 ; RRID:Addgene_51406); The E-cadherin-GFP was a gift from Jennifer Stow (Addgene plasmid # 28009 ; http://n2t.net/addgene:28009 ; RRID:Addgene_28009); The GPCR68 (NM_001177676), integrin β2 (NM_000211), and VEGFR2 (NM_002253) plasmids were constructed by the

Miaoling company (Wuhan). The vector backbone of the constructed plasmids was pcDNA3.1 with an inserted GFP tag.

2.1.2 qPCR

Total RNA was isolated from cultured cells employing the mRNA Purification Kit (Takara) following the manufacturer's protocol. RNA concentration and purity were quantified using a NanoDrop One spectrophotometer (Thermo Scientific), with absorbance ratios (A260/A280) consistently ranging between 1.8-2.0. For cDNA synthesis, 1 μg of purified mRNA underwent reverse transcription with the mRNA reverse-transcription kit (Takara) as specified in the technical manual. Quantitative real-time PCR (qPCR) reactions were conducted in 10 μl volumes containing: 1 μl cDNA template, 10 μM forward/reverse primers (final concentration), SsoAdvanced™ Universal SYBR® Green Supermix (Bio-Rad), and nuclease-free water. Amplification cycles were executed on a CFX96 Touch™ system (Bio-Rad) using the thermal profile recommended by the reagent manufacturer. Gene expression data were normalized to the internal reference gene and calculated using the comparative -△△Ct method relative to Ctrl samples. Values represent mean ± SEM from three independent biological replicates. Primer sequences utilized were as follows:

Human GPCR68:

F - CCCGGTGGTCTATGTTACCG, R – AGCCCACGCTGATGTAGATG.

Human Integrin β2:

F - AAGGAGAAAGAGTGCCAGCC, R – CATCAGTGGCAAACACCAGC.

Human VEGFR2:

F - GTAACCCGGAGTGACCAAGG, R – AACCAAGGTACTTCGCAGGG.

Human E-cadherin:

F - AGTGACTGATGCTGATGCCC, R – AATGTACTGCTGCTTGGCCT

2.1.3 Calcium imaging

293T cells underwent three washes with Margo-Ringer bath solution composed of (in mM): 130 NaCl, 5 KCl, 1 $MgCl_2$, 2.5 $CaCl_2$, 10 Glucose, and 20 HEPES (pH adjusted to 7.4 with NaOH). Subsequently, cells were incubated with 3 μM Fura-2 AM fluorescent calcium indicator (Invitrogen, F1200) in the same solution at 37°C for 30 min. Following dye loading, cells were transferred to a recording chamber mounted on an inverted fluorescence microscope (Nikon Eclipse Ti, Tokyo, Japan). Fluorescence-positive cells were identified for calcium imaging using a 20 × objective. Fura-2 was alternately excited at 340 nm and 380 nm wavelengths (3s interval per wavelength) via a high-speed monochromator, with emitted fluorescence captured at 510 ± 20 nm through a band-pass filter. The ratio of fluorescence intensities (F340/F380) served as the quantitative measure of intracellular calcium dynamics. All calcium transients were calculated as $\triangle F/F_0$ (%) relative to baseline fluorescence intensity (F_0), where F_0 represents the average fluorescence during the 5s pre-stimulation period.

The parameter of US stimulation for calcium imaging is depicted in Fig. 15B. The US stimulation setup included a commercially available transducer (I7-0012-P-SU, Olympus) and a function generator as depicted in Fig. 15A. This system generated 200-tone burst pulses with a center frequency of 0.5 MHz, a repetition frequency of 1 kHz, and a duty cycle of 50%. The output intensity was maintained within the range of 0.1 to 0.6 MPa, with a 3 second interval between each pulse according to the experiment. Peak-

to-peak pressure was quantified and spatially mapped using a custom system equipped with a calibrated hydrophone (Onda, HGL400) mounted on a 3D motor. For measurements, the transducer was positioned at a 45° angle relative to the culture dish, while the hydrophone was placed above the dish.

2.1.4 Quantification of membrane mechanical forces

The magnitude of the mechanical force (suction) exerted on the cell via the patch-clamp micropipette is determined by the hydrostatic pressure difference in a U-tube water column and calculated using the conversion formula (1 mmH_2O = 0.07355 mmHg) (Fig. 16A)

2.1.5 Recording of mechanical force-induced inward currents

Prior to patch-clamp recording, cells were perfused with Margo-Ringer solution and transferred to an inverted fluorescence microscope stage (Nikon Eclipse Ti, Tokyo, Japan). Borosilicate glass micropipettes (Sutter Instrument BF150-86-7.5, USA) were fabricated using a P-1000 puller (Sutter Instrument Co, USA), achieving final resistances of 5-7 MΩ when filled with intracellular solution containing (in mM): 138 KCl, 10 NaCl, 1 $MgCl_2$, 10 Glucose, and 10 HEPES (pH 7.4 adjusted with KOH). Membrane potential recordings were acquired through a Multiclamp 700B amplifier coupled to a DigiData 1550B acquisition system (Axon Instruments). Upon establishing whole-cell configuration with GΩ seal resistance, voltage-clamp gap free recording was implemented to continuously monitor membrane currents. Following baseline stabilization, suction is applied to the cells employing a syringe. The results were calculated as current density (pA/pF) for comparison of differences between the two groups.

2.1.6 Statistical analysis

All data were compiled in GraphPad Prism for statistical analysis, which included two-tailed unpaired t-tests or two-way ANOVA followed by Tukey's test for multiple comparisons. The results were then visualized graphically. A P value of less than 0.05 was considered statistically significant, while ns denotes no significance.

2.2 Results and discussion

2.2.1 E-cadherin-expressing groups showed significant calcium responses to low-intensity US stimulation

To systematically screen for optimal sonosensitive molecules and further investigate the role of mechanosensitive molecules in cellular responses to ultrasound stimulation, we established a candidate molecular library encompassing diverse functional categories based on comprehensive literature review and bioinformatic analysis. This library specifically focuses on non-ion channel mechanosensitive membrane proteins, which play pivotal roles in mechanosensation and signal transduction due to their unique structural and functional characteristics.

Based on extensive literature evidence, we selected four promising molecular candidates exhibiting responsiveness to ultrasound stimulation: GPCR68 (a subtype of G protein-coupled receptor), VEGFR2 (vascular endothelial growth factor receptor 2), integrin β2 (an extracellular matrix receptor), and E-cadherin (an epithelial cell-cell adhesion molecule) (Fig. 14A). These molecules were chosen according to the following criteria: (1) they have been clearly reported to respond to mechanical stimuli (including, but not limited to, hemodynamic shear stress and substrate stiffness); (2) these molecules convert mechanical signals into biochemical signals through their specific structural

domains, subsequently transmitting the signals to the nucleus via intricate intracellular mechanotransduction networks. This process ultimately leads to the activation of specific transcription factors and chromatin remodeling, initiating genome-wide transcriptional reprogramming that precisely regulates cellular behaviors such as proliferation, migration, differentiation, and apoptosis [131] (refer to Section 1.4).

To identify the most effective sonosensitive molecules, we constructed corresponding expression vectors using molecular cloning techniques and achieved efficient transfection in HEK293T cells via lipofection. 48 hours post-transfection, we performed RT-qPCR to assess the transcriptional levels of these mechanosensitive molecules. The results demonstrated significant upregulation of target gene mRNA levels in all transfected groups compared to the Ctrl (Fig. 14B). Notably, VEGFR2 exhibited the most pronounced increase (mean $-\triangle\triangle Ct = 21.7 \pm 2.1$), whereas integrin β2 showed relatively moderate upregulation (mean $-\triangle\triangle Ct = 4.4 \pm 0.9$). This discrepancy may be attributed to differences in mRNA stability or post-transcriptional regulatory mechanisms. Meanwhile, confocal microscopy under FITC excitation revealed strong GFP fluorescence signals in both transfected and Ctrl groups (Fig. 14C), confirming successful exogenous protein expression and proper membrane localization. These findings provide a solid foundation for further investigation into the functional responses of these molecules under ultrasound stimulation. Ctrl

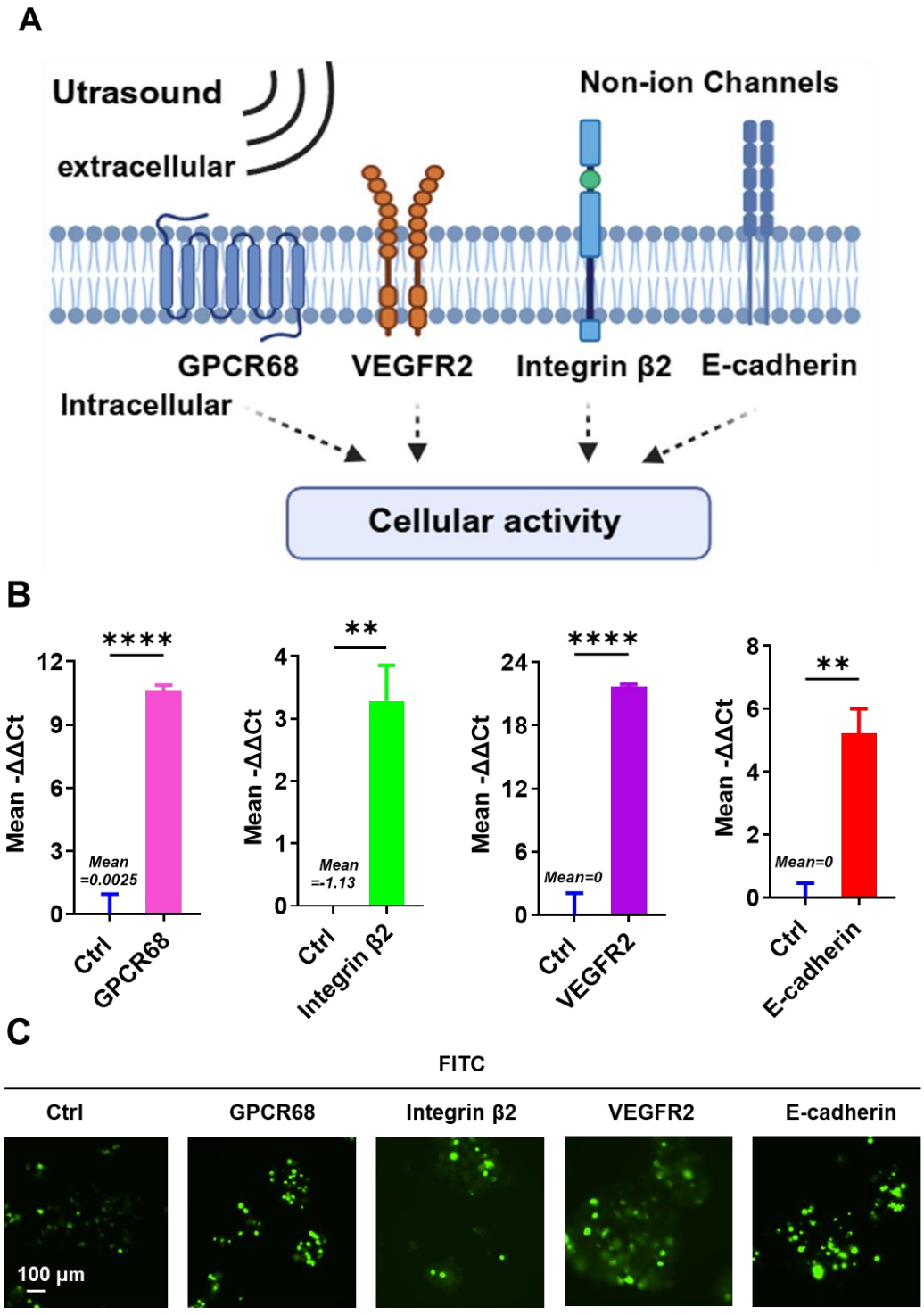

Figure 14. Expression of the non-ion channel protein in 293T cells. **(A)** Schematic workflow for screening non-ion channel proteins (GPCR68, VEGFR2, integrin β2 and E-cadherin) in 293T cells by son-force. **(B)** The mRNA levels and **(C)** fluorescence imaging of non-ion channel proteins (GPCR68, integrin β2, VEGFR2, and E-cadherin) in transfected 293T cells under FITC.

We then implemented a dual-modality platform integrating real-time calcium imaging with a calibrated US transducer to investigate ultrasound-induced calcium response of transfected cells (Fig. 15A). Precisely controlled acoustic parameters were applied while monitoring intracellular Ca^{2+} dynamics (Fig. 15B), These ultrasonic parameters (0.5 MHz central frequency, 1 kHz pulse repetition frequency, 50% duty cycle, 3s intervals) have been applied in in vitro experiments [72]. Given that the cytoskeleton serves as a prerequisite for mechanotransduction [133]— we pharmacologically disrupted actin polymerization using cytochalasin D (CD, 5 μM, 2 hours pretreatment). The results showed that under 0.30 MPa US stimulation, only the E-cadherin transfection group exhibited significant Ca^{2+} influx, as detected by the Fura-2 calcium indicator ($\Delta F/F0$ >20% in GFP^{+} cells, Fig. 15C, D, E), while the responses of the GPCR68, integrin β2, VEGFR2, and Ctrl groups remained at the baseline level (~2%, Fig. 15C). The mechanically induced signal transduction is known to involve the cytoskeleton [133, 134]. As expected, the US-induced calcium response can be abolished by cytochalasin D (CD, 5 μM, 2 hours pretreatment), – A potent inhibitor of actin polymerization that disrupts actin microfilaments. (Fig. 15C, D), confirming that the observed Ca^{2+} influx depended on the integrity of the cytoskeleton, these results corroborate earlier evidence suggesting that the cytoskeletal network, composed of filamentous polymers, functions as a mechanosensitive scaffold that regulates plasma membrane ion channel activity and may propagate mechanical stress from the membrane to intracellular compartments [135].

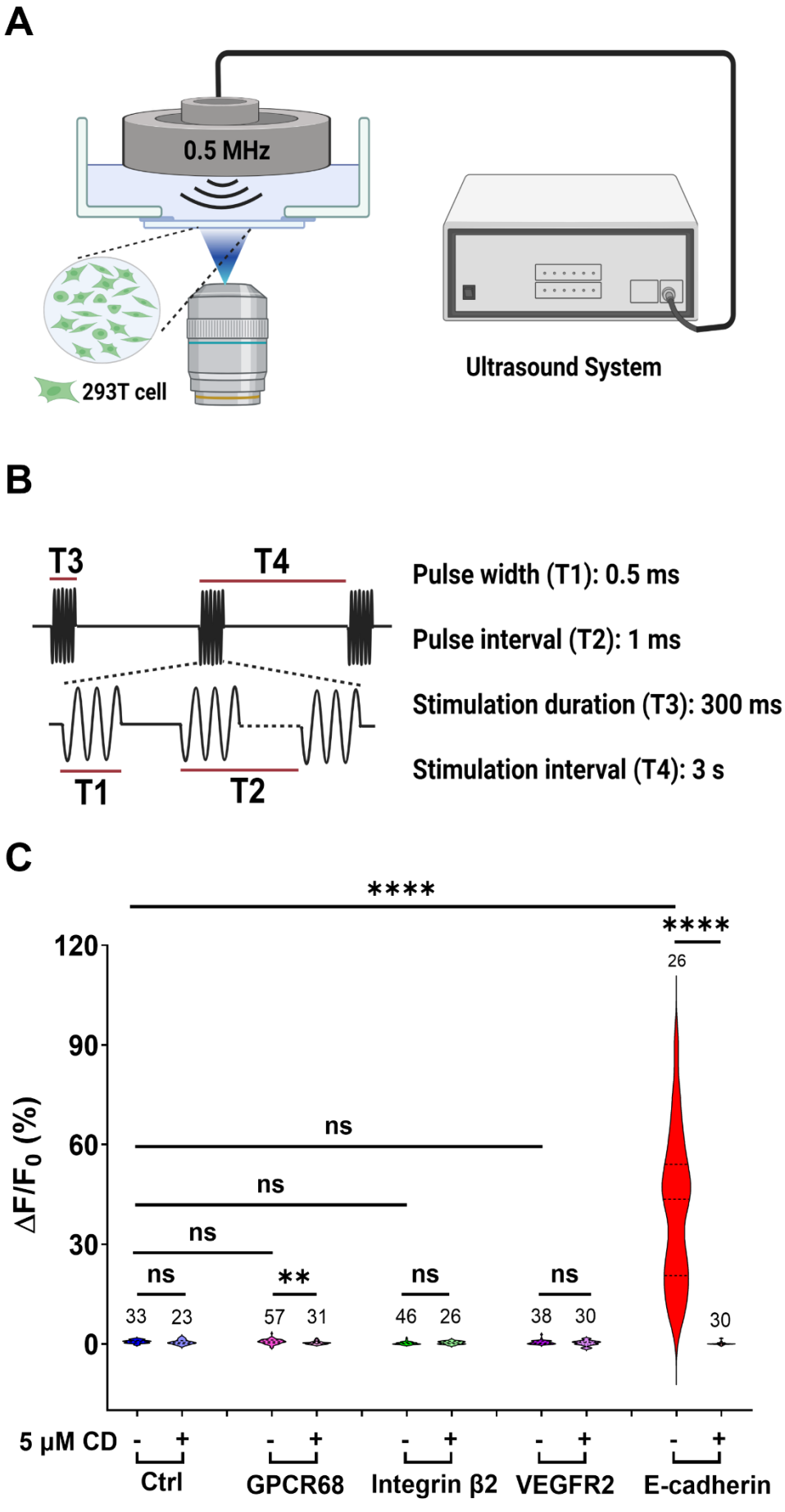
A
0.5 MHz
293T cell
Ultrasound System
B
T3
T4
T1
T2
Pulse width (T1): 0.5 ms
Pulse interval (T2): 1 ms
Stimulation duration (T3): 300 ms
Stimulation interval (T4): 3 s
C
****
****
120
90
60
30
0
ΔF/F0 (%)
ns
ns
ns
ns
**
ns
ns
33 23
57 31
46 26
38 30
26
30
5 μM CD - + - + - + - + - +
Ctrl
GPCR68
Integrin β2
VEGFR2
E-cadherin

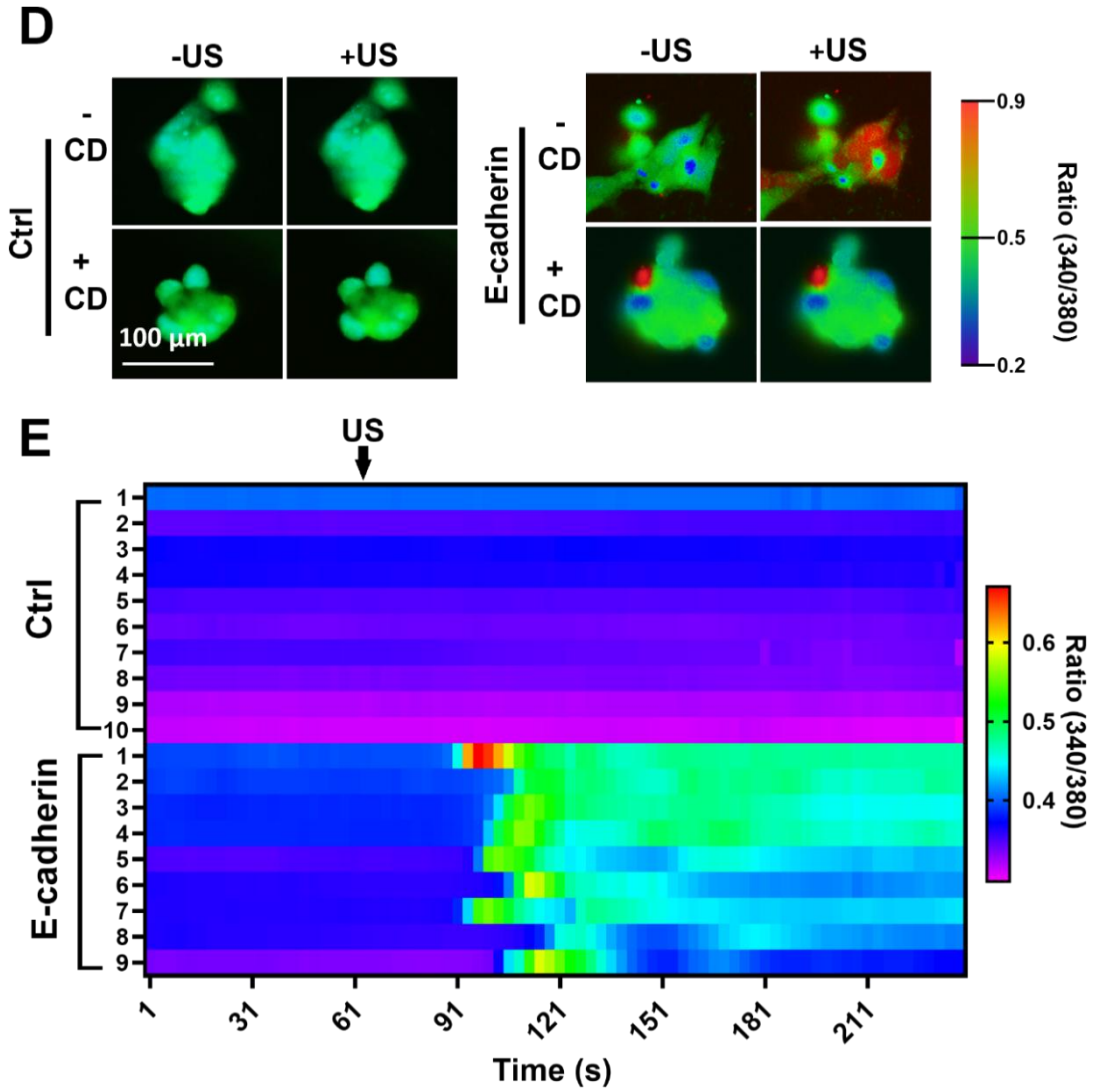

Figure 15. Non-ion channel protein mediate ultrasound-induced activation of 293T cells. **(A)** Schematic workflow for screening non-ion channel proteins (GPCR68, VEGFR2, integrin β2 and E-cadherin) in 293T cells by son-force. **(B)** Ca^{2+} measurement setup in transfected 293T cells under US stimulation (0.5 MHz central frequency, 1 kHz pulse repetition frequency, 50% duty cycle, 3s intervals). **(C)** Quantified Ca^{2+} responses induced by 0.3 MPa US stimulation, cells were treatment with or without 5μM Cytochalasin D for 20 minutes. the number of cells in each group were labeled in graph, mean ± SEM; **P < 0.01, ****P < 0.0001 by two-way ANOVA with Tukey's post hoc test. **(D)** Representative Fura-2 images showing Ca^{2+} dynamics of E-cadherin or Ctrl expressed cells without (-US) and with ultrasound (+US) stimulation, and each group of

cells were treatment with or without 5 μM Cytochalasin D. **(E)** Hot map of Ca^{2+} dynamics of E-cadherin or Ctrl expressed cells before and after US stimulation (0.30 MPa).

2.2.2 Force-dependent increase in currents correlated with mechanical force application in E-cadherin-expressing cells.

After that, we performed single-cell electrophysiological characterization guided by GFP fluorescence localization (Fig. 16B) to functionally validate E-cadherin's direct mechanotransduction capacity, and whole-cell currents were recorded under voltage-clamp mode while negative pressure was applied through the pipette to deliver mechanical stimulation [136, 137] to the cell membrane (Fig. 16B). The magnitude of the mechanical force (suction) exerted on the cell via the patch-clamp micropipette is determined by the hydrostatic pressure difference in a U-tube water column and calculated using the conversion formula (1 mmH_2O = 0.07355 mmHg) (Fig. 16A). We found that the E-cadherin-transfected cells showed a mechanically dependent inward current, while the Ctrl group did not (Fig. 16C). Collectively, these multimodal investigations definitively establish E-cadherin as the principal mechanotransducer mediating ultrasound-evoked cellular activation through a cytoskeleton-dependent pathway.

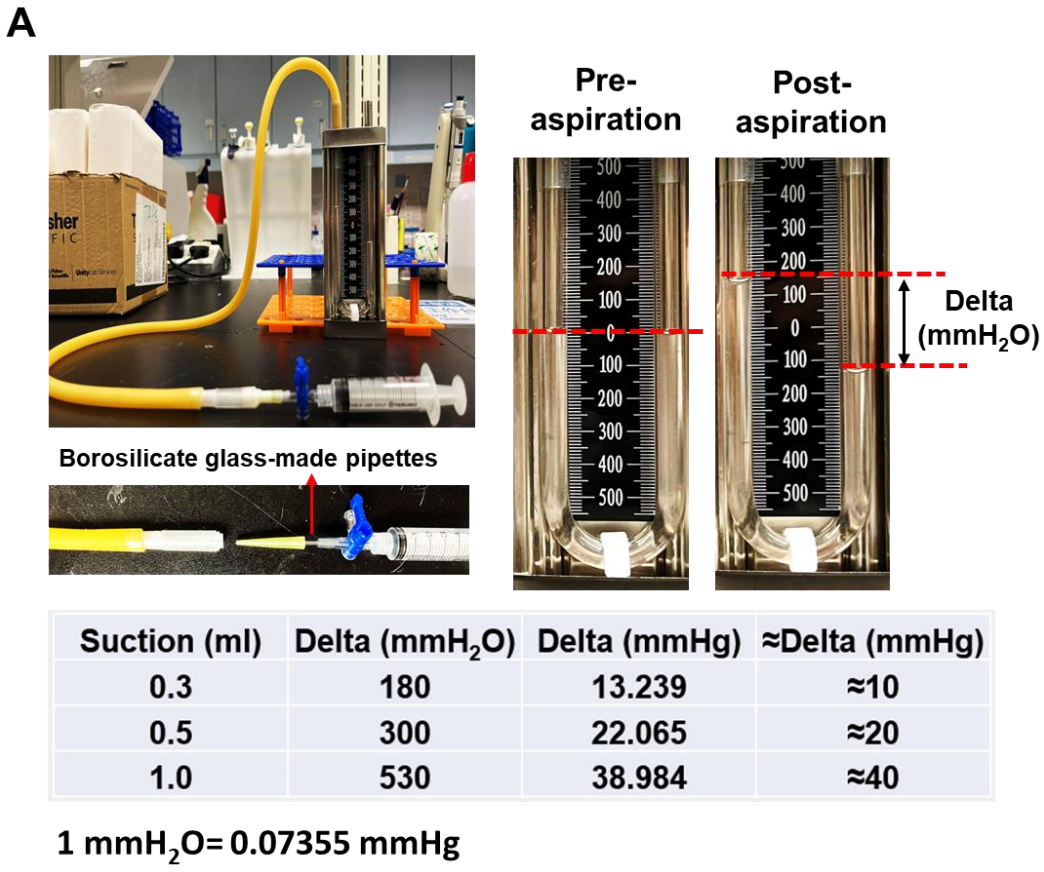

Suction (ml)	Delta (mmH_2O)	Delta (mmHg)	≈Delta (mmHg)
0.3	180	13.239	≈10
0.5	300	22.065	≈20
1.0	530	38.984	≈40

1 mmH_2O= 0.07355 mmHg

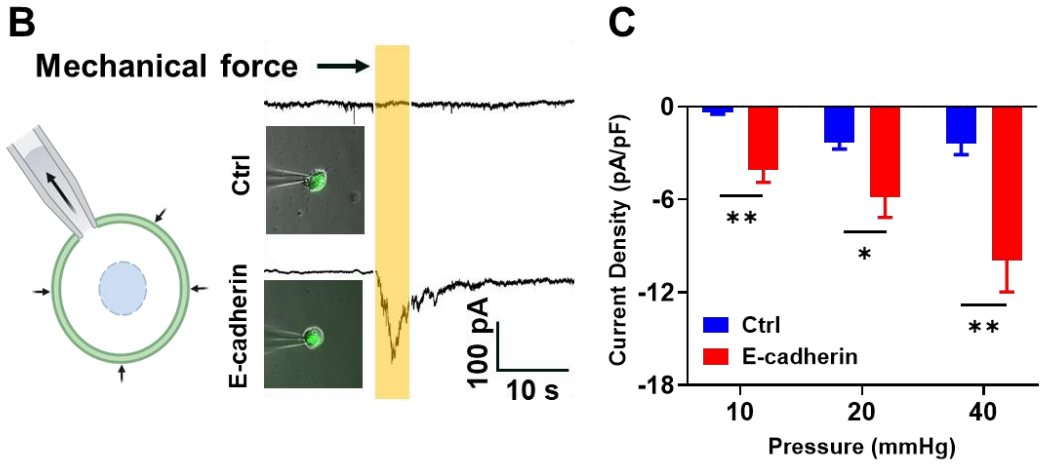

Figure 16. The mechanical force-induced currents in E-cadherin-expressing 293T cells. **(A)** Schematic diagram of mechanical force (aspiration) quantification in pipette applications. A U-tube water manometer (zeroed at the right limb) is connected to the pipette via a sealed rubber tube, with the pipette tip linked to a syringe. Withdrawing 0.3–1.0 mL of negative pressure generates measurable water column height differences, converted to mmHg (1 mmH_2O = 0.07355 mmHg; below). **(B)** *Left*： illustration of mechanical forces exerted on a cell during whole-cell

recording. *Right*： Mechanical force-evoked current traces in E-cadherin/Ctrl transfected cells. **(C)** Current density (pA/pF) under graded mechanical stimulation, n=6 cells in Ctrl group, n=7 cells in E-cadherin group, mean ± SEM; *P < 0.05, **P < 0.01 by two-tailed unpaired t-test.

CHAPTER 3 E-cadherin can enhance the US response of specific MSCs.

3.1 Materials and methods

3.1.1 Cell culture and transfection

Chinese hamster ovary (CHO) cells (ATCC) were maintained under identical culture conditions to 293T cells. For experimental procedures, cells were segregated into four treatment groups and plated onto 35 mm glass-bottom confocal dishes at 2.5×10^5 cells per dish. Following 24-hour incubation at 37°C/5% CO_2, transfection was performed using the Lipofectamine 3000 kit (Invitrogen). Specifically, 3.0 μl Lipofectamine 3000 and 6 μl P3000 reagent were combined in Opti-MEM I Reduced Serum Medium (Gibco) as per manufacturer's protocol to form transfection complexes. After 36-hour post-transfection incubation, cellular expression efficiency was initially assessed via GFP epifluorescence microscopy. Subsequently, transfected cells were rinsed with PBS and loaded with 3 μM Fura-2 calcium indicator (Invitrogen) in Margo-Ringer solution at 37°C for 30 min prior to calcium imaging recording.

For E-cadherin and Piezo1/TRPC1 co-transfection, the transfection groups were as follows：Group 1：Ctrl (3 μg)，Group 2：E-cadherin (1.5 μg)，Group 3：Piezo1/TRPC1 (1.5 μg)，Group 4：E-cadherin (1.5 μg) + Piezo1/TRPC1 (1.5 μg). The E-cadherin and/or Ctrl plasmids in each group were added 6 hours after the addition of Piezo1/TRPC1, Groups 2 and 3 were supplemented with an additional 1.5 μg of empty vector plasmid (without GFP insertion) to balance the total plasmid quantity. The sources of the additional plasmids were as follows: Ctrl, pcDNA3.1(+)IRES GFP was a gift from Kathleen_L Collins (Addgene plasmid # 51406 ; http://n2t.net/addgene:51406 ;

RRID:Addgene_51406)；Murine E-cadherin mCherry was a gift from Alpha Yap (Addgene plasmid # 71366 ; http://n2t.net/addgene:71366 ; RRID:Addgene_71366)；mPiezo1-IRES-eGFP was a gift from Ardem Patapoutian (Addgene plasmid # 80925 ; http://n2t.net/addgene:80925 ; RRID:Addgene_80925)；mTRPC1-GFP (P40179) was constructed by the Miaoling company (Wuhan).

For E-cadherin and TRPA1 co-transfection, the transfection groups were as follows：Group 1：Ctrl (3 μg)，Group 2：E-cadherin (1.5 μg)，Group 3：TRPA1 (1.5 μg)，Group 4：E-cadherin (1.5 μg) + TRPA1 (1.5 μg). The E-cadherin and/or Ctrl plasmids in each group were added 6 hours after the addition of TRPA1, Groups 2 and 3 were supplemented with an additional 1.5 μg of empty vector plasmid (without GFP insertion) to balance the total plasmid quantity. The sources of the additional plasmids were as follows: Ctrl, pcDNA3.1(+)IRES GFP was a gift from Kathleen_L Collins (Addgene plasmid # 51406 ; http://n2t.net/addgene:51406 ; RRID:Addgene_51406)；E-cadherin-GFP was a gift from Jennifer Stow (Addgene plasmid # 28009 ; http://n2t.net/addgene:28009 ; RRID:Addgene_28009)；pcDNA3.1+_hsTRPA1_myc_dTom was a gift from Sreekanth Chalasani (Addgene plasmid # 183179 ; http://n2t.net/addgene:183179 ; RRID:Addgene_183179)；

3.1.2 qPCR

Total RNA was isolated from cultured cells employing the mRNA Purification Kit (Takara) following the manufacturer's protocol. RNA concentration and purity were quantified using a NanoDrop One spectrophotometer (Thermo Scientific), with absorbance ratios (A260/A280) consistently ranging between 1.8-2.0. For cDNA

synthesis, 1 μg of purified mRNA underwent reverse transcription with the mRNA reverse-transcription kit (Takara) as specified in the technical manual. Quantitative real-time PCR (qPCR) reactions were conducted in 10 μl volumes containing: 1 μl cDNA template, 10 μM forward/reverse primers (final concentration), SsoAdvanced™ Universal SYBR® Green Supermix (Bio-Rad), and nuclease-free water. Amplification cycles were executed on a CFX96 Touch™ system (Bio-Rad) using the thermal profile recommended by the reagent manufacturer. Gene expression data were normalized to the internal reference gene and calculated using the comparative -△△Ct method relative to Ctrl samples. Values represent mean ± SEM from at least three independent biological replicates. Primer sequences utilized were as follows:

Mouse Piezo1:

F - GCAGTGGCAGTGAGGAGATT, R - GATATGCAGGCGCCTATCCA.

Mouse TRPC1:

F - CGTGCGACAAGGGTGACTAT, R – CTCCCAAGCACATCTACGCA.

Human TRPA1:

F - CAATGTCGCCAACTGCCAAA, R - AGCGGGGCAAATTTTCCAAC.

3.1.3 Calcium imaging

CHO cells underwent three washes with Margo-Ringer bath solution composed of (in mM): 130 NaCl, 5 KCl, 1 $MgCl_2$, 2.5 $CaCl_2$, 10 Glucose, and 20 HEPES (pH adjusted to 7.4 with NaOH). Subsequently, cells were incubated with 3 μM Fura-2 AM fluorescent calcium indicator (Invitrogen, F1200) in the same solution at 37°C for 30 min. Following dye loading, cells were transferred to a recording chamber mounted on an inverted

fluorescence microscope (Nikon Eclipse Ti, Tokyo, Japan). Fluorescence-positive cells were identified for calcium imaging using a 20 × objective. Fura-2 was alternately excited at 340 nm and 380 nm wavelengths (3s interval per wavelength) via a high-speed monochromator, with emitted fluorescence captured at 510 ± 20 nm through a band-pass filter. The ratio of fluorescence intensities (F340/F380) served as the quantitative measure of intracellular calcium dynamics. All calcium transients were calculated as $\triangle F/F_0$ (%) relative to baseline fluorescence intensity (F_0), where F_0 represents the average fluorescence during the 5s pre-stimulation period.

3.1.4 Whole-cell recording

Prior to patch-clamp recording, cells were perfused with Margo-Ringer solution and transferred to an inverted fluorescence microscope stage (Nikon Eclipse Ti, Tokyo, Japan). Borosilicate glass micropipettes (Sutter Instrument BF150-86-7.5, USA) were fabricated using a P-1000 puller (Sutter Instrument Co, USA), achieving final resistances of 5-7 MΩ when filled with intracellular solution containing (in mM): 138 KCl, 10 NaCl, 1 $MgCl_2$, 10 Glucose, and 10 HEPES (pH 7.4 adjusted with KOH). Membrane potential recordings were acquired through a Multiclamp 700B amplifier coupled to a DigiData 1550B acquisition system (Axon Instruments). Upon establishing whole-cell configuration with GΩ seal resistance, voltage-clamp gap free recording was implemented to continuously monitor membrane currents. The results were calculated as current density (pA/pF) for comparison of differences between the two groups.

3.1.5 Statistical analysis

All data were consolidated in GraphPad Prism for statistical evaluation using two-way ANOVA with Tukey's post hoc test. Graphical representations were subsequently generated based on the analytical outcomes. A significance threshold was set at $P < 0.05$, with ns indicating non-significant results.

3.2 Results and discussion

3.2.1 E-cadherin enhances calcium responses of mechanosensitive channels (Piezo1) to US stimulation

As shown in our preceding findings, US stimulation triggers calcium influx in E-cadherin-overexpressing HEK293T cells, it is critical to note that E-cadherin – a classical intercellular junction protein – lacks the intrinsic capacity to mediate calcium flux [114, 138]. To explore the potential mechanism of E-cadherin mediated US - induced calcium influx, we investigated potential cooperative interactions between E-cadherin and endogenous mechanotransduction pathways. Existing studies have shown that MSCs can endow cells with the ability to respond to US stimulation [73, 74, 87, 89-94], and E-cadherin structurally interacts with specific MSCs[139]. Based on this, we hypothesized that E-cadherin may enhance the sensitivity of cells to US by enhancing the function of MSCs.

To test this hypothesis, we employed CHO cells, which were devoid of endogenous mechanosensitive channel expression, co-transfected with E-cadherin and three mechanosensitive channels: Piezo1, TRPC1, and TRPA1. To exclude confounding effects from differential plasmid expression, we quantified Piezo1 transcript levels via Quantitative reverse transcription polymerase chain reaction (qRT-PCR). The results

showed that the Piezo1 transcription levels in the Piezo1 group and the co-transfected with Piezo1 and E-cadherin (hereafter referred to as Piezo1+E-cadherin) group were significantly higher than those in the Ctrl group and the E-cadherin group. However, there was no significant difference in Piezo1 expression between the Piezo1 group and the Piezo1+E-cadherin group (Fig. 17A). Functional validation using whole-cell voltage-clamp recordings demonstrated that YODA1—a selective Piezo1 agonist—elicited comparable current densities in Piezo1 and Piezo1+E-cadherin groups (Fig. 17B). This transcriptional and electrophysiological congruence confirms that E-cadherin enhances US sensitivity without altering Piezo1 transcription level and intrinsic Piezo1 channel properties. Interestingly, calcium imaging revealed that ultrasound-induced Ca^{2+} transients were higher in Piezo1+E-cadherin cells ($\Delta F/F_0 = 43.02\% \pm 7.39\%$) compared to Piezo1-only cells ($\Delta F/F_0 = 19.95\% \pm 5.73\%$) (Fig. 17 C, D). No detectable responses ($\Delta F/F_0 < 1\%$) were observed in cells expressing E-cadherin alone or Ctrl (Fig. 17C, D).

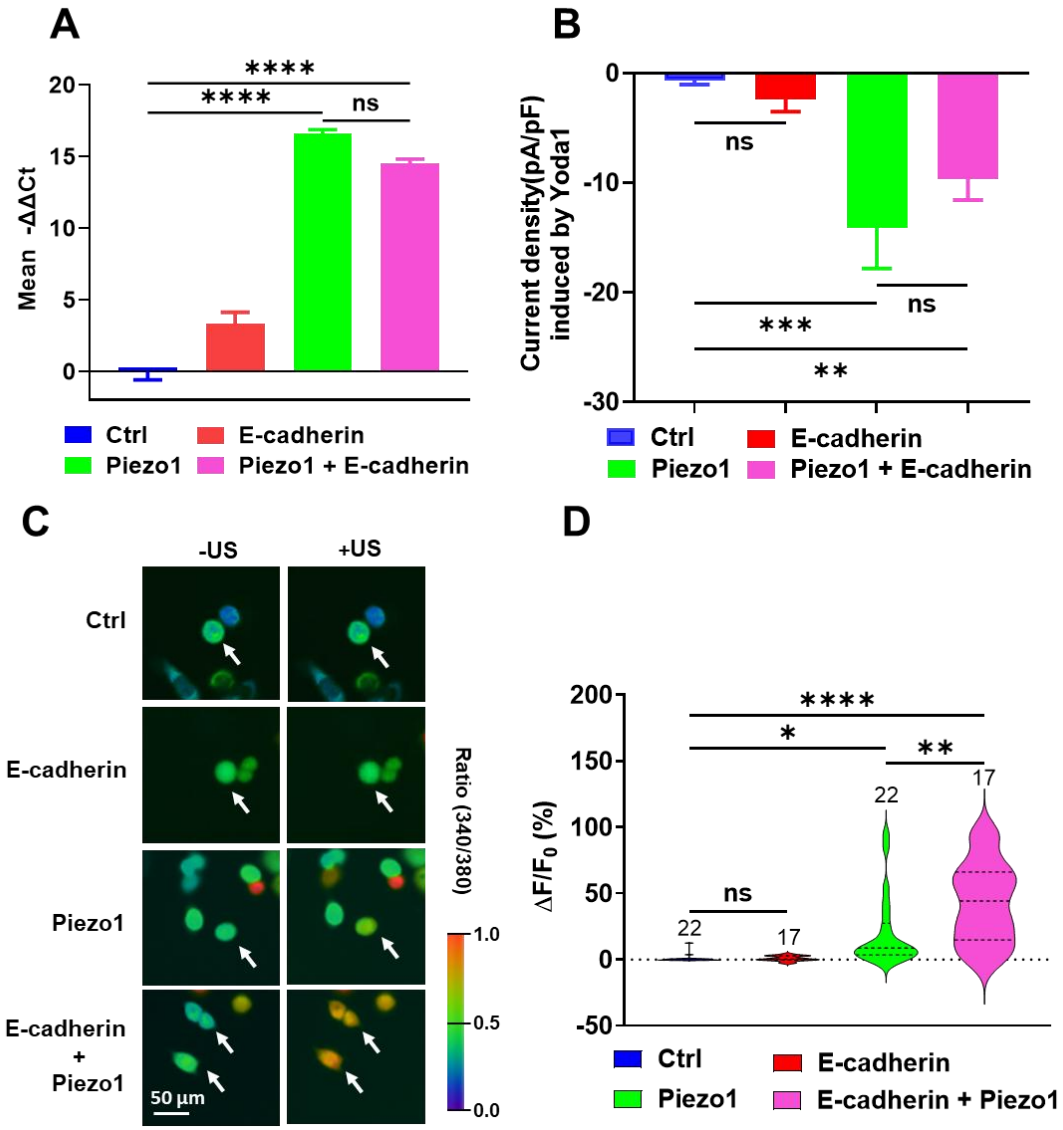

Figure 17. E-cadherin co-expression with Piezo1 significantly enhances Ca^{2+} response upon US stimulation.

(A) The mRNA levels of Piezo1 in CHO cells, the group labels indicated the transfection plasmids. n = 3 biological replicates in each group, mean ± SEM; ****P < 0.0001 by one-way ANOVA with Šídák' test. **(B)** Yoda1 (10 μM)-induced current densities in Ctrl, E-cadherin, Piezo1, Piezo1 + E-cadherin groups respectively, n = 3 to 4 cells in each group, mean ± SEM; **P < 0.01, ***P < 0.001 by one-way ANOVA with Tukey's test. **(C)** Fura-2 imaging of Ctrl, E-cadherin, Piezo1 or E-cadherin+Piezo1 transfected CHO cells with (+US) or without (-US) ultrasound stimulation. Arrows indicate fluorescence positive cells that were selected for analysis. **(D)** Quantified US (0.5 MHz, 0.3 MPa)-induced Ca^{2+} responses. The other US parameters were as follows: duty cycle:

50%, duration: 500 ms, 3 s intervals. **(B, D)** Number of cells n in each group were labeled in graph. mean ± SEM; *P < 0.05, **P < 0.01, ****P < 0.0001 by one-way ANOVA with Tukey's test.

3.2.2 E-cadherin could not enhance calcium responses of mechanosensitive channels (TRPC1 and TRPA1) to US stimulation

We employed the same approach to investigate whether E-cadherin enhances the responsiveness of TRPC1 to US stimulation. The TRPC1 mRNA expression level (Fig. 18A) and the current density (pA/pF) induced by the TRPC1 agonist carbachol also showed a similar trend (Fig. 18B). However, the calcium imaging results indicated that the US -induced Ca^{2+} response in the E-cadherin+TRPC1 and the TRPC1 group was significantly higher than in the Ctrl or the E-cadherin group as expected, but without significant difference between E-cadherin+TRPC1 ($\Delta F/F_0$ = 9.89% ± 1.62%) and the TRPC1 alone group ($\Delta F/F_0$ = 10.78% ± 1.63%) (Fig. 18C).

A similar pattern of results was also observed in the parallel experiment using TRPA1 (comparable response: $\Delta F/F_0$ = 9.72% ± 1.58% in E-cadherin+TRPA1 vs $\Delta F/F_0$ = 9.64% ± 2.03% in TRPA1, no obvious response: $\Delta F/F_0$ = 0.39% ± 2.34% in E-cadherin and $\Delta F/F_0$ = 0.81% ± 2.19% in Ctrl), with the MSC-expressing groups showing comparable levels of TRPA1 expression, and significant response to US, but with no observed enhancement from additional E-cadherin expression (Fig. 18D, E, F). Taken together, these results indicate that E-cadherin specifically enhanced the US-induced Ca^{2+} influx mediated by the mechanosensitive channel Piezo1, thereby improving the cell's sensitivity to US stimulation, but had no obvious effect on the functioning of the TRPC1 and TRPA1 channels.

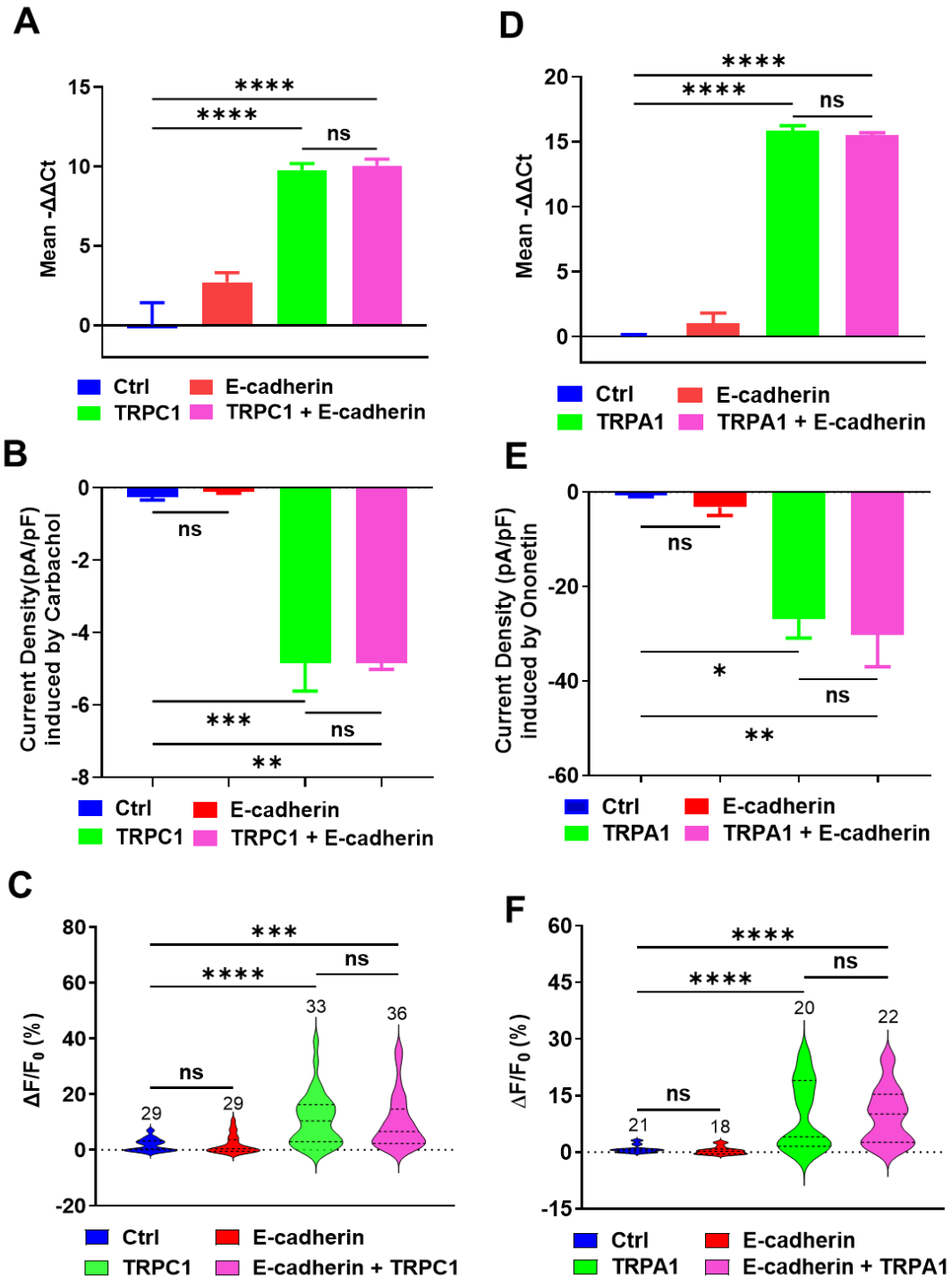

Figure 18. E-cadherin-mediated sonogenetics requires Piezo1 function. **(A)** The mRNA levels of TRPC1 in CHO cells, the group labels indicated the transfection plasmids. (n = 3 biological replicates in each group, mean ± SEM; ****P < 0.0001 by one-way ANOVA with Šídák' test. **(B)** Carbachol (100 mM)-induced current densities in Ctrl, E-cadherin, TRPC1, E-cadherin + TRPC1 groups respectively. n = 3 to 5 cells in each group, mean ± SEM;

P < 0.01, ***P < 0.001 by one-way ANOVA with Tukey's test. **(C) Quantified US (0.5 MHz, 0.3 MPa)-induced Ca^{2+} responses. The other US parameters were as follows: duty cycle: 50%, duration: 500 ms, 3-s intervals. Number of cells n in each groups were labeled in graph. mean ± SEM; ***P < 0.001, ****P < 0.0001 by one-way ANOVA with Tukey's test. **(D)** The mRNA levels of TRPA1 in CHO cells, the group labels indicated the transfection plasmids. (n = 3 biological replicates in each group, mean ± SEM; ****P < 0.0001 by one-way ANOVA with Šídák' test. **(E)** Ononetin (20 μM)-induced current densities in Ctrl, E-cadherin, TRPA1, E-cadherin+TRPA1 groups respectively. n = 3 to 6 cells in each group, mean ± SEM; *P < 0.05, **P < 0.01 by one-way ANOVA with Tukey's test. **(F)** Quantified US (2.25 MHz, 0.25 MPa) induced Ca^{2+} responses. The other US parameters were as follows: duty cycle: 50%, duration: 500 ms, 3-s intervals. Number of cells n in each groups were labeled in graph. mean ± SEM; ****P < 0.0001 by one-way ANOVA with Tukey's test.

CHAPTER 4 E-cadherin expressed heterologously in primary cortical neurons can enhance US-induced Ca^{2+} influx

4.1 Materials and methods

4.1.1 Culture and transfection of rat primary cortical neurons

Primary cortical neurons were dissociated from embryonic day 18 (E18) Sprague-Dawley rat embryos. Cortical tissues were microdissected in ice-cold Neurobasal medium (Gibco, 21103049), followed by enzymatic digestion with 0.25% trypsin (Gibco) at 37°C for 15 min. The digestion was terminated by adding Neurobasal medium supplemented with 10% fetal bovine serum (FBS), 0.25% L-Glutamine, 1% Penicillin-Streptomycin, and 0.1% DNase I (all Gibco). Tissue suspensions were gently triturated using fire-polished Pasteur pipettes and centrifuged at 1000 rpm for 5 min at 25°C. After supernatant removal, cell pellets were resuspended in complete Neurobasal medium (containing 10% FBS, 0.25% Glutamine, 1% Penicillin-Streptomycin) and plated at 1×10^5 cells/well onto poly-L-lysine (PLL, Sigma 25988-63-0) coated 35 mm culture dishes (50 μg/mL coating concentration). After 24-hour incubation, the medium was replaced with serum-free Neurobasal medium containing 2% B27 supplement, 0.25% L-Glutamine, and 1% Penicillin-Streptomycin. Subsequently, 1/2 of medium exchanges were performed every 48 hours until experimental use.

For the calcium imaging and western blot experiment, cells were transfected with pAAV-hSyn-MCS/E-cadherin-3xFLAG-tWPA virus (Multiplicity of infection, MOI: 5×10^4) on day 8. For an immunofluorescence experiment, cells were transfected with pAAV-hSyn-MCS-GFP or pAAV-hSyn-E-cadherin-3xFLAG-tWPA (MOI: 5×10^4) on day 8.

The transfected cells were performed calcium imaging, and harvest for western blot or immunofluorescence experiment on day 10.

4.1.2 Calcium imaging

Primary cortical neurons were perfused three times with oxygenated Margo-Ringer bath solution containing (in mM): 130 NaCl, 5 KCl, 2.5 $CaCl_2$, 1 $MgCl_2$, 20 HEPES，10 Glucose, and (pH 7.4 adjusted with NaOH). Subsequently, cells underwent loading with 3 μM Fura-2 AM calcium indicator (Invitrogen F1200) in the same solution at 37°C for 30 min. After incubation with the dye, neurons were placed on the stage of an inverted fluorescence microscope (Nikon Eclipse Ti, Japan) for subsequent imaging.

Fura-2-loaded cells were identified using a 20 × objective. Dual-wavelength excitation at 340 nm and 380 nm (3s alternation interval) was delivered via a monochromator, with emitted fluorescence captured through a 510 ± 20 nm bandpass filter. Intracellular calcium dynamics were quantified as the ratio of fluorescence intensities (F340/F380). Calcium transients were calculated as $\triangle F/F_0$ (%), where F_0 represents baseline fluorescence averaged over the 5s pre-stimulation period. Ultrasound stimulation parameters are detailed in Fig. 15B.

4.1.3 Western blot

Transfected neurons underwent ultrasound stimulation within a humidified incubator (37°C, 5% CO_2) using parameters identical to calcium imaging experiments, except for 10-second stimulation intervals. Continuous 20-minute US exposure was followed by 90-minute post-stimulation incubation. Cells were washed three times with ice-cold 1× PBS and lysed on ice in RIPA buffer (EMD Millipore) containing protease

and phosphatase inhibitors (Thermo Fisher Scientific). The lysates were then centrifuged at 12,000 g for 15 min at 4°C to pellet cellular debris, and the resulting supernatants were quantified for protein content using a bicinchoninic acid (BCA) assay.

For immunoblotting, protein samples (50 μg per lane) were denatured at 95°C for 5 min, separated on 10% SDS-polyacrylamide gels, and transferred onto nitrocellulose membranes with a semi-dry transfer system. Membranes were blocked with 5% non-fat milk prepared in TBST (Tris-buffered saline with 0.1% Tween-20) for 1 h at room temperature (25°C), followed by overnight incubation with primary antibodies at 4°C. After washing three times with TBST (10 min each), membranes were incubated for 1 h at 25°C with HRP-conjugated secondary antibodies diluted at 1:2000. Following final washes, protein bands were visualized by chemiluminescence using ECL substrate (Pierce) and imaged with a Bio-Rad ChemiDoc MP system.

Primary antibodies c-Fos (rabbit, #2250s) were diluted at 1:250, E-cadherin (rabbit, #3195) and GAPDH (mouse, #97166) antibodies were diluted at 1:500, and all the antibodies were purchased from Cell Signaling Technology. Secondary antibodies included HRP-conjugated goat anti-rabbit IgG (H+L) (#31460) and goat anti-mouse IgG (H+L) (#31431) from Invitrogen, both diluted 1:1000 in blocking buffer. Protein levels were quantified using ImageJ and expressed as fold changes relative to the 0 MPa ultrasound treatment group. Data are presented as mean ± SEM from three independent experiments.

4.1.4 Immunofluorescence staining

Primary neurons received 15-minute Paraformaldehyde (PFA) fixation at 25°C. Following three 5-minute PBS washes, samples were blocked for 1 hour at room

temperature with PBS-based blocking buffer containing 10% goat serum, 5% bovine serum albumin (BSA), and 0.3% Triton X-100. Primary antibody incubation proceeded at 4°C overnight. After additional triple PBS washes (5 min each), neurons were incubated with species-matched secondary antibodies (Alexa Fluor-conjugated, 1:1000) for 1 hour at 25°C. Post-immunostaining, samples were air-dried prior to mounting in 4′,6-diamidino-2-phenylindole (DAPI) - containing Fluoromount-G (SouthernBiotech). Fluorescence images were acquired using a Nikon Eclipse Ti2 microscope equipped with a 20 × objective and NIS-Elements AR software (Japan).

For E-cadherin and colocalized with Microtubule-associated protein 2 (MAP-2) staining，E-cadherin (rabbit, #3195T) were diluted at 1:500, and all purchased from Cell Signaling Technology. MAP-2 (mouse, MAB3418) were purchased from sigma and diluted at 1:500. Secondary antibodies were used Cross-Adsorbed Goat anti-Rabbit IgG (H+L) Secondary Antibody, Alexa Fluor™ 488 (A-11008) and Highly Cross-Adsorbed Goat anti-Mouse IgG (H+L) Secondary Antibody, Alexa Fluor™ Plus 555 (A32727) purchased from Invitrogen, diluted at 1: 1000 in a blocking buffer.

For c-Fos and E-cadherin co-staining in primary neurons. c-Fos primary antibodies (rabbit, #2250s) and E-cadherin (mouse, #3195) were diluted at 1:250 in the blocking buffer, all purchased from Cell Signaling Technology. The following secondary antibodies were applied at a 1:1000 dilution in blocking buffer: Alexa Fluor™ 555-conjugated Cross-Adsorbed Goat anti-Rabbit IgG (H+L) (Invitrogen, A-21428) and Alexa Fluor™ 488-conjugated Goat anti-Mouse IgG, IgM (H+L) (Invitrogen, A-10680). Quantification of c-Fos-positive neurons was performed in a single-blinded manner by an experimenter who was unaware of group allocations.

4.1.5 Statistical analysis

All data were compiled in GraphPad Prism for statistical analysis, which included two-tailed unpaired t-tests or two-way ANOVA followed by Tukey's test or uncorrected Fisher's LSD test for multiple comparisons. The results were then visualized graphically. A significance threshold was set at $p < 0.05$, with ns indicating non-significant results.

4.2 Results and discussion

4.2.1 E-cadherin expressed heterologously in primary cortical neurons can enhance US-induced Ca^{2+} influx

Given the observed enhancement effect of E-cadherin expression significantly enhances Piezo1-mediated ultrasound responsiveness (by 2.1-fold), we sought to investigate its role in ultrasonic neuromodulation. Notably, Piezo1 - a key mechanosensitive ion channel - exhibits widespread expression patterns throughout the mouse central nervous system, as systematically characterized by high-throughput in situ hybridization data from the Allen Mouse Brain Atlas. These data demonstrate abundant Piezo1 expression in multiple brain regions including the cortex, hippocampus, and cerebellum. Our prior work has established that Piezo1 contributes substantially to ultrasound-induced neuromodulation, as evidenced by significantly attenuated calcium responses upon Piezo1 knockout [72].

To establish a robust experimental model, we employed an AAV9-hSyn vector system to achieve targeted E-cadherin expression in cultured rat primary cortical neurons . This delivery system features neuron-specific expression (driven by the hSyn promoter) with high transduction efficiency (>80%) [140]. Immunofluorescence co-localization analysis revealed that E-cadherin signals exhibited over 80% co-localization with the mature neuronal marker MAP-2 (n=9 fields of view), while Ctrl groups showed no

detectable signal (Fig. 19A,B). Western blot semi-quantitative analysis further confirmed significantly higher E-cadherin expression in transfected neurons compared to Ctrl (Fig. 21A).

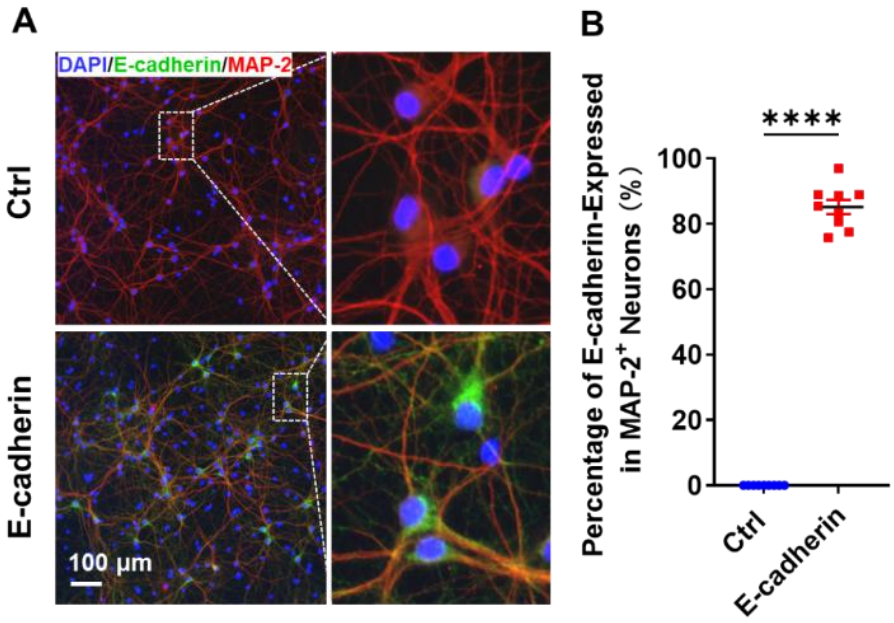

Figure 19. Immunofluorescence of E-cadherins and MAP-2$^+$ in transfected neurons. **(A)** E-cadherin (green) colocalization with MAP-2$^+$ neurons (red) and DAPI (blue). **(B)** The percentage of E-cadherin in MAP-2$^+$ neurons in Ctrl or E-cadherin virus expressed groups. n= 9 field (20×) in Ctrl or E-cadherin group from 3 biological replicates, mean ± SEM; ****P < 0.0001 by two-tailed unpaired t-test.

To elucidate E-cadherin's mechanotransduction function, we employed high spatiotemporal-resolution calcium imaging (20 Hz sampling rate) to monitor neuronal responses to ultrasound stimulation. Results demonstrated that E-cadherin-expressing neurons exhibited substantially enhanced ultrasound-evoked calcium transients ($\Delta F/F_0$ = 26.3 ± 2.2%) compared to Ctrl (8.5 ± 1.2%) at 0.3 MPa stimulation (Fig. 20 A-C). Importantly, this calcium response showed dose-dependent amplification when

ultrasound intensity increased to 0.6 MPa ($\Delta F/F_0 = 62.8 \pm 8.9\%$, Fig. 20C).

Structurally, the mechanotransduction by cadherins enables cells to sense and respond to physical changes in their environment, a process at the heart of which lies the dynamic linkage between the cadherin-catenin adhesion complex and actin filaments (F-actin) [118]. As predicted, pharmacological disruption of actin networks using cytochalasin D (5 μM) completely abolished ultrasound-induced calcium signaling in both experimental and control groups ($\Delta F/F_0 < 10.0\%$, Fig. 20C). These results collectively demonstrate that heterologous expression of E-cadherin in neurons potentiates ultrasound-evoked Ca^{2+} influx.

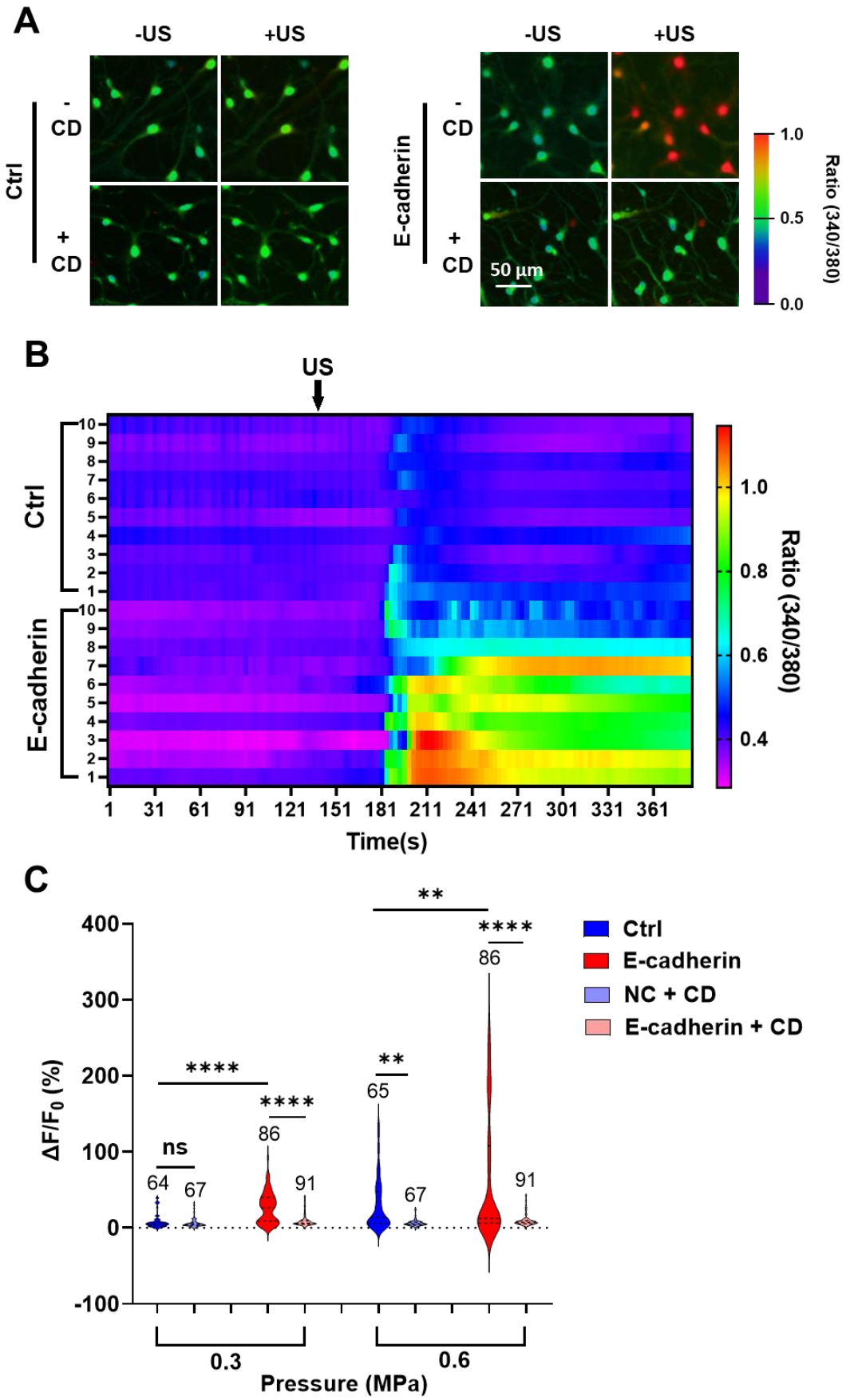
A
-US
+US
Ctrl
-CD
+CD
E-cadherin
50 μm
1.0
0.5
0.0
Ratio (340/380)
B
US
Ctrl
E-cadherin
1.0
0.8
0.6
0.4
Ratio (340/380)
1 31 61 91 121 151 181 211 241 271 301 331 361
Time(s)
C
Ctrl
E-cadherin
NC + CD
E-cadherin + CD
ΔF/F0 (%)
400
300
200
100
0
-100
ns
****
**
64
67
86
91
65
0.3
0.6
Pressure (MPa)

Figure 20. E-cadherin mediates ultrasound-induced Ca^{2+} influx in primary neurons. **(A)** Fura-2 imaging of transfected neurons with or without 0.3 MPa stimulation, cells in E-cadherin or Ctrl groups were pretreated with or without 5μM Cytochalasin D for 2 hours before Ca^{2+} imaging recording. **(B)** Hot map of Ca^{2+} dynamics of E-cadherin or Ctrl expressed neurons before and after US stimulation (0.3 MPa). **(C)** Quantified Ca^{2+} influx of under 0.3 and 0.6 MPa, number of cells n in each groups were labeled in graph, mean ± SEM; **P < 0.01, ****P < 0.0001 by two-way ANOVA with Tukey's test).

4.2.2 E-cadherin expressed heterologously in primary cortical neurons can upregulate ultrasound-induced neuronal activation biomarkers

To evaluate the neuronal activation induced by US stimulation, we evaluated expression level changes of c-Fos, the immediate early gene c-Fos is a well-known molecular marker of neuronal activation triggered by Ca^{2+} influx [141, 142]. The experimental setup depicted in (Fig. 21A). Primary neurons were continuously cultured under standard conditions (37°C, 5% CO_2) during treatment to preserve physiological integrity. After 20 minutes of 0.3 MPa US stimulation, western blot semi-quantitative analysis shows that US-induced c-Fos upregulation in E-cadherin-expressing neurons compared to Ctrl or E-cadherin-expressing only groups (Fig. 21B, C).

To further elucidate whether the observed c-Fos upregulation originated from E-cadherin-transfected neurons, we performed immunofluorescence staining to visualize c-Fos expression, the proportion of US -induced c-Fos-positive neurons (red) in E-cadherin-transfected neurons (green) significantly increased to 46.8 ± 6.0% (compared to 23.0 ± 3.5% in the Ctrl group, $p < 0.01$) (Fig. 21D, E), while both groups remained below 30.0% under unstimulated conditions (Fig. 21D, E). These data together confirm that E-cadherin significantly enhances the sensitivity of primary neurons to US stimulation by

mediating Ca^{2+} influx and neuronal activation.

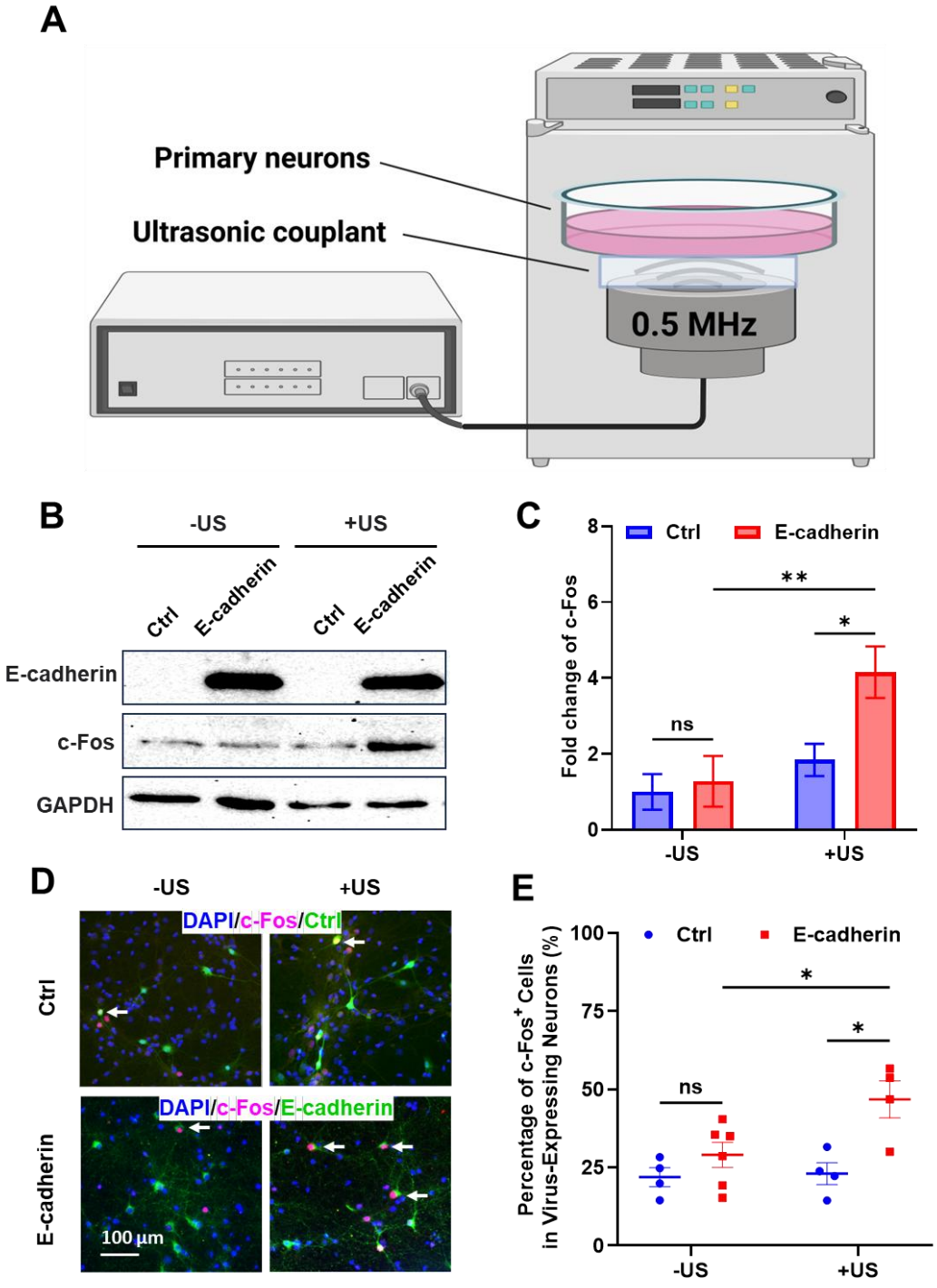

Figure 21. E-cadherin mediates ultrasound-induced c-Fos activation in primary neurons. **(A)** A schematic diagram of the ultrasound device configuration for treating cultured neurons within an incubator, followed by immunofluorescence staining or Western blot analysis. The space between the culture dish and the ultrasound transducer is filled with an ultrasonic coolant

to ensure efficient ultrasonic wave transmission. **(B)** Representative Western blot images for the level of c-Fos in E-cadherin/Ctrl-transfected cells treated with or without US treatment (0.3 MPa). **(C)** Bar chart shows c-Fos protein levels as a fold change compared with the untreated Ctrl, mean ± SEM of 3 independent experiments，*P < 0.05, **P < 0.01 by two-way ANOVA with uncorrected Fisher's LSD. **(D)** Immunofluorescence of c-Fos (red) and Ctrl/E-cadherin (green) with (+ US) or without (- US) 0.3 MPa US treatment. **(E)** The calculation of c-Fos-positive cells of Fig. C, each points n represents a biological replicate, mean ± SEM; *P < 0.05 by two-way ANOVA with Tukey's test.

4.2.3 E-cadherin expression did not affect neurons' electrical properties.

To comprehensively evaluate the biosafety profile of E-cadherin as a novel sonogenetic actuator and its potential impact on fundamental neuronal electrophysiological properties, we subsequently conducted a series of systematic electrophysiological characterization experiments under *in vitro* conditions. Specifically, utilizing whole-cell patch-clamp electrophysiology configured in current-clamp mode, recordings were performed on primary cultured neurons successfully expressing E-cadherin. Crucially, the experimental results demonstrated that key passive electrical properties of neurons, including but not limited to resting membrane potential, neuronal firing frequency, and spike amplitude, showed no statistically significant differences between the E-cadherin group and the Ctrl group (Fig. 22A-D). This finding robustly demonstrates that exogenous expression of E-cadherin does not intrinsically disrupt the neuron's ability to maintain its basic electrophysiological homeostasis.

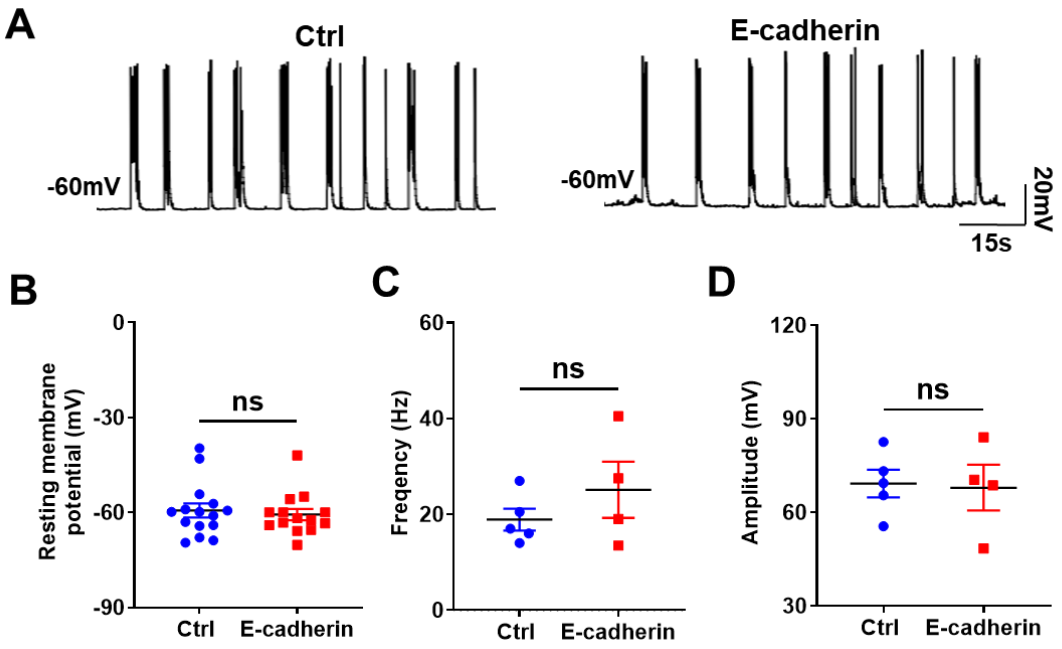

Figure 22. Electrophysiological characterization of E-cadherin-expressing neurons. **(A)** Current-clamp recordings of membrane potential of Ctrl/E-cadherin expressed primary neurons. **(B-D)** Calculation of resting membrane potential, firing frequency and amplitude of Ctrl/E-cadherin expressed neurons. For RMP, n = 10 Ctrl, n = 9 E-cadherin, for frequency and amplitude n = 5 Ctrl, n = 4 E-cadherin, mean ± SEM by two-tailed unpaired t-test.

CHAPTER 5 E-cadherin enables sonogenetic activation of mouse layer V motor cortex neurons and downstream muscular active-tion *in vivo*

5.1 Materials and methods

5.1.1 Experimental animals

All animal experiments utilized 8-week-old male C57BL/6J mice (supplied by The Chinese University of Hong Kong) for *in vivo* ultrasound stimulation. Mice were group-housed under controlled environmental conditions (22 ± 1°C, 55 ± 5% humidity, 12 h light/dark cycle) with ad libitum access to standard rodent chow and autoclaved water. Subjects were randomly assigned to experimental cohorts using computer-generated randomization protocols. All procedures strictly adhered to the ethical standards outlined in the Animals (Control of Experiments) Ordinance administered by the Department of Health, Hong Kong Special Administrative Region Government, China. Veterinary supervision was maintained throughout the study period.

5.1.2 Virus injection

Mice were anesthetized via intraperitoneal injection of ketamine (100 mg/kg) and xylazine (10 mg/kg), followed by placement in a stereotaxic frame. After clipping the fur over the skull, ophthalmic ointment was applied to both eyes to prevent corneal drying. For fiber photometry recording, the cortical brain M1 region (AP 0.25 mm, ML -1.5 mm, DV -1.0 mm) was injected with 0.5 μl of virus (pAAV-CaMKIIα-GCaMP6s, Calcium/calmodulin-dependent protein kinase II alpha, CaMKIIα, Genetically encoded calcium indicator, GCaMP6s, OBiO Technology) + 0.5 μl of virus (Ctrl, pAAV-

CaMKIIα-MCS-3FLAG-tWPA or E-cadherin, pAAV-CaMKIIα-E-cadherin-3FLAG-tWPA, OBiO Technology). For electromyography recording, the cortical brain M1 region was only injected with 1.0 μl of virus (Ctrl, pAAV-CaMKIIα-MCS-3FLAG-tWPA or E-cadherin, pAAV-CaMKIIα-E-cadherin-3FLAG-tWPA, OBiO Technology). Viral injection was performed through a small craniotomy (<1 mm^2) at a rate of 0.1 μl/min using a microinjection system (Nanoliter 2010, WPI Ltd.). Following a 10-minute injection period, the needle was slowly withdrawn. The skull puncture site was disinfected and sutured, after which the mice were returned to their home cages for a 3-week recovery period prior to optic fiber implantation. The fiber was then implanted at the target coordinates (AP: +0.25 mm, ML: −1.5 mm, DV: −1.0 mm) and secured to the skull with dental cement, which was allowed to cure for 20 minutes. After disinfecting the skin around the cement, the animals were returned to their home cages and allowed to acclimate for one week before fiber photometry recording began.

5.1.3 Immunofluorescence staining

Brain tissues were harvested after whole-body perfusion by 4% PFA and fixed by immersion of PFA overnight at 4°C. After washing in PBS, the brain slices were removed along the coronal position with a thickness of 40 μm by vibratomes (Leika VT1200). Slices or primary neurons were blocked with blocking buffers (10% goat serum, 5% BSA, 0.3% Triton X-100 in PBS) at room temperature for 2 hours and incubated with primary antibodies overnight at 4°C. Washed 3 times and incubated the secondary antibody for 90 minutes at room temperature. Following additional washes, the slices were dried and mounted with DAPI. Images were acquired with a fluorescence microscope (Nikon Eclipse Ti2, Japan).

For E-cadherin staining in brain slice in fiber photometry experiments, E-cadherin (rabbit, #3195T) were diluted at 1:250 in the blocking buffer. Secondary antibodies were used Cross-Adsorbed Goat anti-Rabbit IgG (H+L) Secondary Antibody, Alexa Fluor™ 555 (Invitrogen, A-21428) diluted at 1: 1000 in blocking buffer.

For E-cadherin staining in brain slice in EMG experiments, E-cadherin (rabbit, #3195T) were diluted at 1:250 in the blocking buffer. Secondary antibodies were used Cross-Adsorbed Goat anti-Rabbit IgG (H+L) Secondary Antibody, Alexa Fluor™ 488 (Invitrogen, A-11008) diluted at 1: 1000 in blocking buffer.

For Ionized calcium-binding adapter molecule 1 (Iba-1) and Glial fibrillary acidic protein (GFAP) staining in brain slice, Iba-1 (rabbit, #17198S), GFAP (rabbit, #12359S), all purchased from Cell Signaling Technology. Secondary antibodies were used Goat anti-Rabbit IgG (H+L) Cross-Adsorbed Secondary Antibody, Alexa Fluor™ 555 (Invitrogen, A-21428) diluted at 1: 1000 in blocking buffer. The number of E-cadherin, MAP-2, Iba-1 and GFAP in primary neurons or brain slices was counted by single-blind, quantified by an experimenter who did not identify the groups beforehand.

5.1.4 Fiber photometry recording in motor cortex (M1)

Prior to fiber photometry recordings, mice were anesthetized using isoflurane (1.0 to 2.5% in O_2) and surgically implanted with optical fibers targeting cortical regions. GCaMP6s fluorescence signals were acquired through a fiber photometry system (Thinker Tech Nanjing BioScience Inc.) with the following optical parameters: 470 ± 15 nm excitation (30 nm bandwidth) and 510 ± 12.5 nm emission (25 nm bandwidth) filters. Signal acquisition occurred at 100 Hz sampling frequency, with subsequent offline

processing via customized MATLAB algorithms (R2021a). Fluorescence dynamics were quantified as $\Delta F/F_0 = (F - F_0)/F_0$, where F_0 represents the 1-second pre-stimulus baseline fluorescence averaged per experimental session. Ultrasound stimulation protocols consisted of 5 repeated 10-second intervals at identical intensity, with all other parameters matching those specified for calcium imaging experiments in Fig. 15B.

5.1.5 Electromyography recording in motor cortex (M1)

Four weeks post-viral injection, mice transduced with either the empty vector or the E-cadherin virus underwent experimental preparation under 2% isoflurane anesthesia (ophthalmic ointment applied to both eyes). Following removal of head hair and application of ultrasound coupling gel, a 0.5MHz transducer was secured. The recording electrode, consisting of two electromyographic (EMG) needles, was inserted into the left forelimb triceps brachii muscle at a 3-5 mm spacing to capture the muscle biopotential difference. A ground electrode was attached to the mouse tail. Five minutes prior to EMG recording initiation, the isoflurane concentration was reduced to 0.5%, inducing a light anesthesia state. Subsequently, five ultrasound stimuli were delivered to each mouse using identical sonication intensity parameters, with an inter-stimulus interval of 10 seconds. EMG signals were acquired using a multi-channel recording system (Medus, Bio-Signal Technologies).

EMG data analysis was performed in MATLAB (The MathWorks, Inc.): The raw signal was initially processed with a 50 Hz notch filter and a 10-150 Hz bandpass filter. The initial 200 ms segment of the recording was designated as the resting period window for baseline value determination. For stimulation-period data, the filtered signal was rectified relative to its mean value. A smoothed envelope was then constructed by

calculating the root mean square (RMS) using a 200 ms sliding window. The relative amplitude was calculated as (peak EMG event amplitude - baseline value) / baseline value (denoted as $\Delta F/F_0$). The response latency was defined as the time difference between the onset of the ultrasound stimulus and the initiation point of the response.

5.1.6 Statistical analysis

All data were compiled in GraphPad Prism for statistical analysis using two-tailed unpaired t-tests or two-way ANOVA followed by Tukey's test for multiple comparisons. Results were then visualized in graphical form. A p-value threshold of <0.05 was set for statistical significance, and ns denotes non-significant findings.

5.2 Results and discussion

5.2.1 Enhanced synchronized calcium signals in motor cortex (M1) of E-cadherin mice following US stimulation

Based upon our finding of successful *in vitro* neuronal activation induced by our E-cadherin-mediated sonogenetic system, we next evaluated the feasibility of E-cadherin as a *in vivo* sonogenetic tool. Stereotaxic co-injection of an E-cadherin and a GCaMP6s virus was performed in the right M1 region of the mouse cerebral cortex. Both viruses were driven by a CaMKIIα promoter, allowing us to achieve cell-type-specificity by targeting excitatory neurons. Control animals receive equivalent injections of empty vectors. After 4 weeks of virus expression, an optical fiber ferrule was implanted, and fiber photometry was performed after 1 week of postoperative recovery (Fig. 23A). Immunofluorescence staining confirmed the specific co-expression of E-cadherin and GCaMP6s in the M1 region (Fig. 23B).

Under isoflurane anesthesia, with the gas inflow rate held constant to ensure a consistent anesthetic depth across both experimental groups (a measure to control for its potential influence on neuronal excitability), mice were stimulated with US treatment, and each intensity was repeated 5 times. Before US stimulation, both groups showed comparable baseline fluorescence levels ($\Delta F/F_0 \approx 0.4$ %, Fig. 23C, D). After applying 0.25 MPa US stimulation, neurons in the E-cadherin group were specifically activated (2.0 ± 0.3% vs. 0.6 ± 0.2% in the Ctrl group) (Fig. 23C, D), and the Ca^{2+} response amplitude in E-cadherin mice was positively correlated with the stimulation intensity (2.3 ± 0.3% at 0.55 MPa), significantly higher than that in the Ctrl group (1.0 ± 0.3%). These results further confirm that E-cadherin enhances the responsiveness of neurons in the motor cortex (M1) to ultrasonic stimulation at the *in vivo* level.

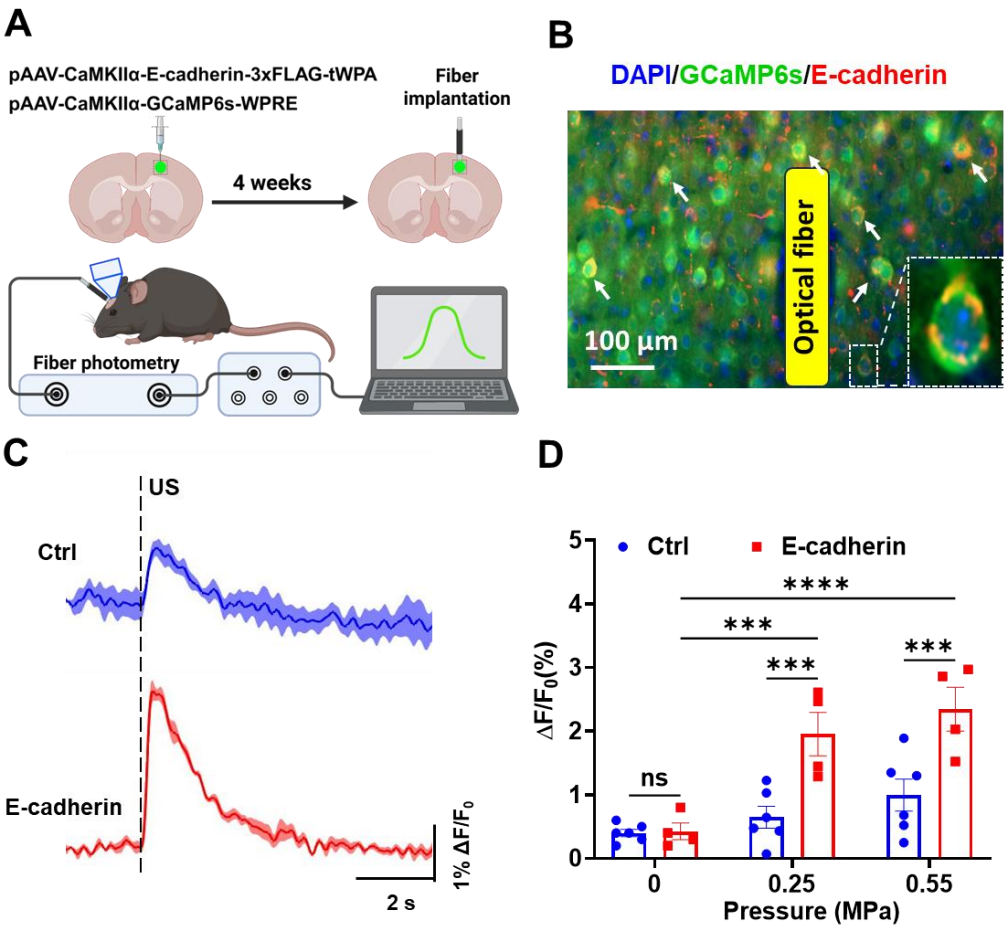

Figure 23. E-cadherin potentiates ultrasound-evoked cortical neuron Ca^{2+} response. **(A)** Viral injection (GCaMP6s + Ctrl/E-cadherin) in right mouse cortex M1 for fiber photometry, Optical fibers were implanted 4 weeks post-viral injection. After allowing a 1-week adaptation period for the mice, fiber photometry recordings were conducted. The US probe was positioned at a 45-degree tilt angle relative to the optical fiber axis and applied to the right cerebral hemisphere. **(B)** E-cadherin (red) and GCaMP6s (green) colocalization in M1. **(C)** Representative fiber photometry traces ($\Delta F/F_0$) of Ca^{2+} signal in Ctrl (blue) and E-cadherin (red) mice at 0.25 MPa acoustic intensities. **(D)** Summarized the amplitude ($\Delta F/F_0$) of Ca^{2+} signals induced by US stimulation. The US parameters were as follows: frequency: 1.0 MHz, duty cycle: 50%, duration: 500 ms, 10-s intervals, five repetition for each group. n = 6 Ctrl, n = 5 E-cadherin, mean ± SEM, ***P < 0.001, ****P < 0.0001 by two-way ANOVA with Tukey's test.

5.2.2 Increased synchronized contralateral forelimb twitching in E-cadherin mice after US stimulation

Building upon the established functional connectivity between the primary motor cortex (M1) and locomotor output [143], we next investigated ultrasound-evoked behavioral modulation in awake mice. We injected the E-cadherin virus with the CaMKIIα promoter and the control virus into the right cerebral cortex (M1) of 8 - week - old mice, which allowed us to achieve cell - type specificity by targeting excitatory neurons. Four weeks after the injection, we used electromyogram (EMG) to measure the response of the contralateral (left) triceps brachii muscle. The US transducer was placed directly above the targeted cortical area, and the stimulation parameters were the same as those described above (Fig. 24A). Consistent with the above observations in Fig.23B, immunofluorescence staining confirmed that E-cadherin expression was restricted to the motor cortex (M1) in mice (Fig. 24B).

Before US application, the EMG signals of both groups of mice remained at the baseline level of approximately 25.0 μV (21.9 ± 21.9 μV in E-cadherin mice vs. 28.1 ±

12.8 μV in Ctrl mice; Fig. 24C, D). When the EMG signals from the mouse limbs were stable, 0.25 MPa US stimulation was randomly applied (variable time intervals). E-cadherin mice showed obvious and reproducible EMG signals (256.9 ± 37.7 μV), which were 4 times that of the Ctrl mice (64.4 ± 17.6 μV) (Fig. 24C, D).

When the US intensity increased to 0.55 MPa, the EMG signals of the E-cadherin mice induced by US were enhanced compared to those at 0.25 MPa, while there was no significant change in the Ctrl mice (Fig. 24D). There was no significant difference in the latency of the EMG response induced by US stimulation between the two groups, which was approximately 150 ms (Fig. 24E), consistent with the results of *in vivo* experiments [91, 144]. Hence, our data show that US stimulation of E-cadherin-expressing neurons could trigger limb twitching in mice, and the amplitude of response was dependent upon the US intensity applied. Taking the above results together, E-cadherin could effectively mediate the specific sonogenetic activation of excitatory neurons in the mouse motor cortex and trigger muscular twitching.

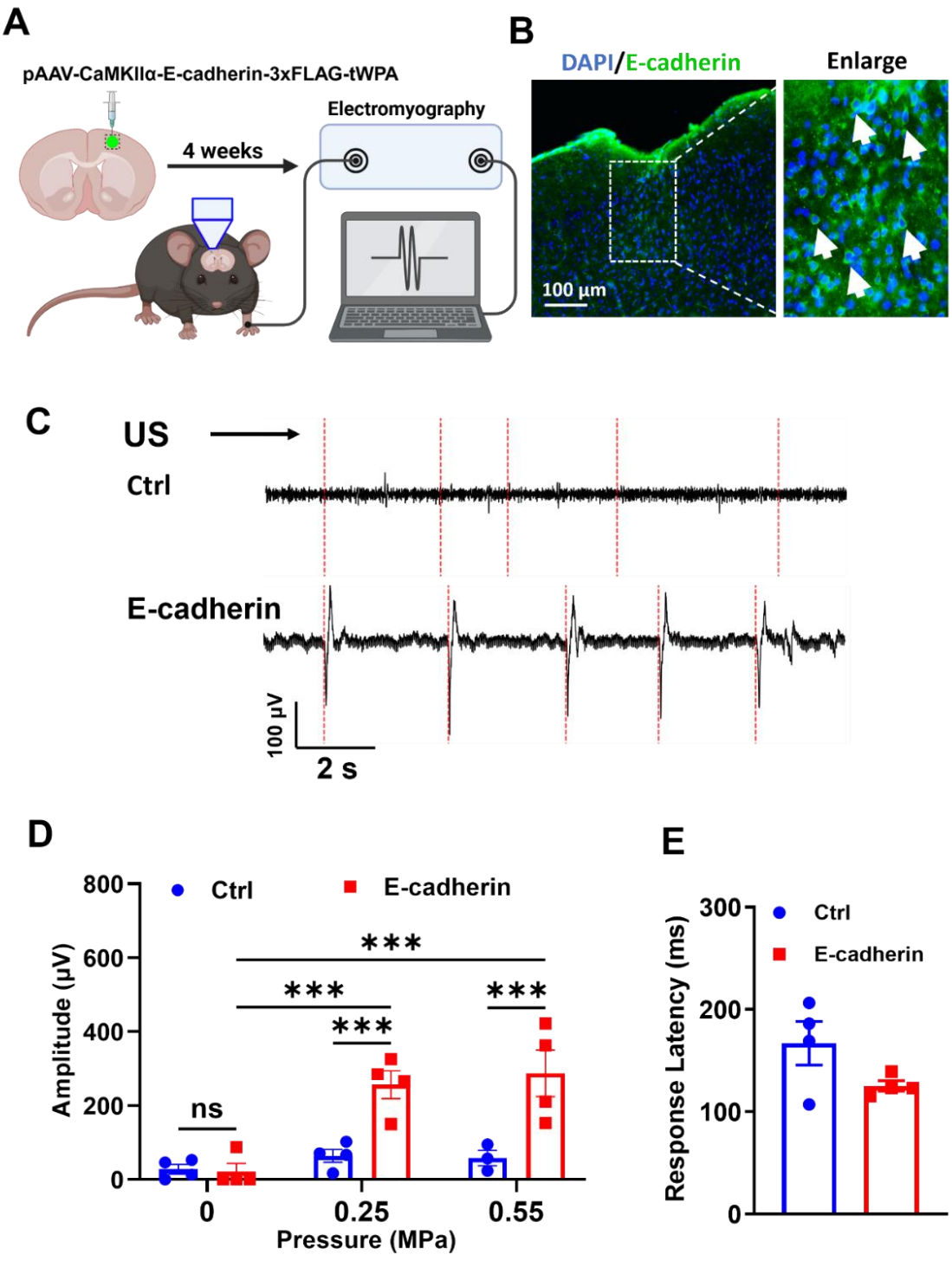

Figure 24. E-cadherin potentiates ultrasound-evoked cortical neuron activation. **(A)** Schematic illustration of the EMG recording experimental strategy. Briefly, viruses were injected into the right mouse cortex M1, and 4 weeks later EMG recording was performed on a left forelimb muscle under US (0.5 MHz, 1 kHz PRF, 50% duty cycle, 300 ms duration). **(B)** Immunofluorescence images of E-cadherin (green) in M1 brain region. White

arrows indicate E-cadherin-positive neurons. **(C)** Representative EMG traces of left forelimb responses under 0.25 MPa acoustic pressure. **(D)** Summarized EMG amplitude at varying acoustic pressures. **(E)** Summarized EMG amplitudes at varying acoustic pressures. n for Ctrl group = 3-4, E-cadherin = 4. mean ± SEM shown; ***P < 0.001 by two-way ANOVA with Tukey's test.

5.2.3 E-cadherin expression did not induce overt neuroinflammation.

To comprehensively evaluate the *in vivo* safety of E-cadherin expression within neural circuits, we specifically investigated whether virus-mediated expression of E-cadherin in the primary motor cortex (M1) elicits a detectable neuroinflammatory response (Fig. 25 A)—a critical determinant of translational safety for neuromodulatory interventions. Neuroinflammation, characterized by glial activation, is a common pathological response following exogenous protein expression or viral vector delivery in the CNS, which can severely compromise neuronal function and survival. Assessing glial reactivity is therefore a crucial indicator of biocompatibility.

Mice were allowed normal housing for one week after the completion of EMG recordings to eliminate any potential interference of EMG procedures with neuroinflammatory responses. A subset of mice was then re-exposed to ultrasound (0.25 MPa, with a 10-second interval) for a duration of 40 minutes. We performed rigorous histological analyses using immunofluorescent staining to quantify established neuroinflammatory biomarkers within the relevant brain regions. We focused on the activation status and morphological phenotypes of two primary glial cell types: Astrocytes were identified using glial fibrillary acidic protein (GFAP) labeling, while microglia were marked with ionized calcium-binding adapter molecule-1 (Iba-1). These markers are highly sensitive indicators of CNS inflammation [145, 146]. Quantitative

analyses revealed that, compared to Ctrl groups, the E-cadherin expression group did not exhibit histologically evident upregulation of astrocytic or microglial activation, nor any morphological alterations (Fig. 25 B-E). These data indicate that induced E-cadherin expression in the mouse motor cortex does not elicit neuroinflammation.

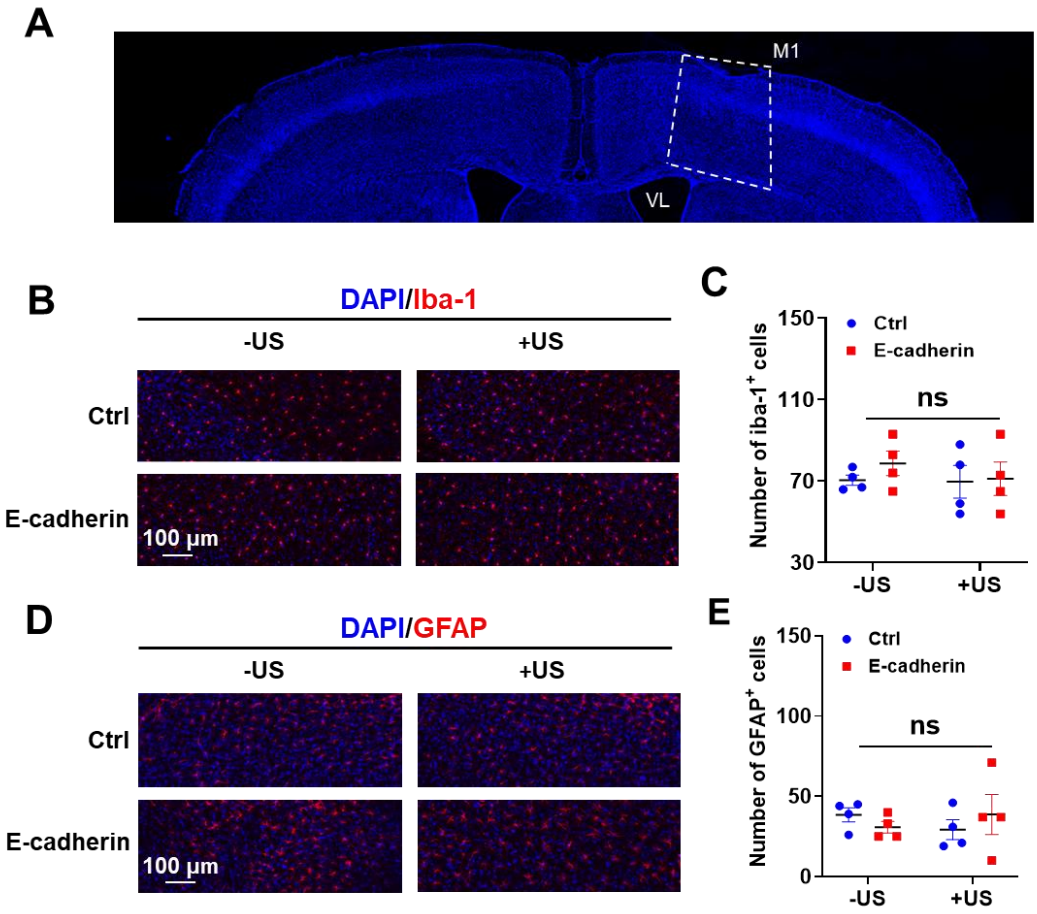

Figure 25. Neuroinflammation evaluation of E-cadherin expression in cortical neurons. **(A)** Brain slice images show DAPI at low magnification, The white dashed trapezoid outlines the motor cortex (M1) targeted for virus injection sides. **(B)** Quantification of Iba1 levels shown in **(A)**. **(C)** Representative immunofluorescence images showing GFAP expression levels and cell morphologies in the M1, with or without US. **(D)** Quantification of GFAP levels shown in (A). For (A)-(E), US treatment was administered for 40 minutes to mice expressing E-cadherin or Ctrl viruses in their M1 cortices, with parameters as follows: frequency, 0.5 MHz; duty cycle, 50%;

duration, 500 ms; 10-s intervals. Each point in **(B)** and **(D)** represents the average Iba-1 or GFAP count (at 20× magnification) of at least three slices from an individual mouse; n = 4. mean ± SEM, ns, non-significant different by two-way ANOVA with Tukey's test.

CHAPTER 6 E-cadherin enables specific sonogenetic activation of mouse motor behaviors

6.1 Materials and methods

6.1.1 Experimental animals

The US stimulation experiments in vivo employed 8-week-old male C57BL/6J mice sourced from The Chinese University of Hong Kong. Animals were group-housed (6 mice/cage) under controlled environmental conditions (22 ± 1°C, 55 ± 5% humidity, 12 h light/dark cycle) with ad libitum access to irradiated rodent chow and acidified water. Subjects were randomly allocated to experimental cohorts using computer-generated randomization sequences. All procedures strictly complied with ethical regulations specified in the Animals (Control of Experiments) Ordinance (Cap. 340) administered by the Department of Health, Hong Kong Special Administrative Region Government, China. Veterinary oversight was maintained throughout the study period.

6.1.2 Viral vector injection and US probe adapter installation

Following anesthesia induction via intraperitoneal injection of ketamine (100 mg/kg) and xylazine (10 mg/kg), mice were secured in a stereotaxic frame. The cranial skin was shaved and ophthalmic ointment applied to prevent corneal desiccation. Through a <1 mm^2 craniotomy, 1.0 μl of recombinant AAV (rAAV-D1-E-cadherin-3FLAG-WPRE-hGHPA or control rAAV-D1-EGFP-WPRE-hGHPA, both from BrainVTA) was microinjected into the dorsomedial striatum (DMS; coordinates: AP +0.50 mm, ML -1.50 mm, DV -3.00 mm relative to bregma) targeting dopamine receptor D1-expressing neurons.

Viral delivery proceeded at 0.1 μl/min using a Nanoliter 2010 injector (WPI Ltd.). Post-injection, the needle remained in situ for 5 min before slow retraction to minimize reflux. The surgical site was disinfected with povidone-iodine and sutured. A miniaturized cranial adapter (Fig. 26B) was affixed with dental cement, with 20 min polymerization time. Pericement skin was re-disinfected prior to returning animals to their home cages.

6.1.3 Immunofluorescence staining

Following transcardial perfusion with ice-cold 4% paraformaldehyde (PFA), harvested brain tissues underwent post-fixation by PFA immersion at 4°C for 24 hours. After three 10 minutes PBS washes, 40-μm coronal sections were prepared using a Leica VT1200 vibratome under continuous PBS cooling (4°C). Brain sections and primary neuronal cultures were incubated for 2 hours at 25°C in a blocking buffer composed of PBS containing 10% normal goat serum, 5% BSA, and 0.3% Triton X-100. Subsequently, samples were incubated with primary antibodies overnight at 4°C.

After PBS washes (5 min each), samples were incubated with species-appropriate secondary antibodies (Alexa Fluor-conjugated, 1:1000) for 1.5 hours at 25°C. Post-staining, sections were mounted in DAPI and imaged using a Nikon Eclipse Ti2 microscope equipped with 20 × objective and NIS-Elements AR 5.30 software.

Primary antibodies E-cadherin (mouse, #14472S), c-Fos (rabbit, #2250s), were diluted at 1:500, and all purchased from Cell Signaling Technology. Secondary antibodies were used Cross-Adsorbed Goat anti-Mouse IgG (H+L) Secondary Antibody, Alexa Fluor™ 488 (A-11001) and Cross-Adsorbed Goat anti-Rabbit IgG (H+L) Secondary Antibody, Alexa Fluor™ 555 (A-21428) and purchased from Invitrogen, diluted at 1:

1000 in a blocking buffer. The number of c-Fos$^+$ in brain slices was counted by single-blinded, quantified by an experimenter who did not identify the groups beforehand.

6.1.4 Open field locomotor analysis

The mice were anesthetized with isoflurane (1.0 to 2.5% in O_2) and an US mini transducer were embedded in an adapter on the mouse's head. The mice were then placed in a cylindrical open-field arena (30 cm diameter, 50 cm height) lined with bedding and housed within a sound-attenuating chamber to minimize external disturbance during a 30-min acclimation period. Behavior was recorded with a commercial digital camera (Logitech), and total distance traveled as well as movement speed were quantified using ToxTrac software.

6.1.5 Statistical analysis

All data were compiled in GraphPad Prism and analyzed using two-way ANOVA followed by Tukey's post hoc test for multiple comparisons. Results were subsequently visualized in graphical form. A significance threshold was set at $p < 0.05$, and ns indicates non-significant findings.

6.2 Results and discussion

6.2.1 Enhancement of motor behavior in E-cadherin mice following US stimulation

We next evaluated our sonogenetic approach's spatial resolution and functional efficacy in deep brain structures. Previous studies have demonstrated that both

magnetothermal and optogenetic activation of the DMS induce increased locomotor activity in mice, revealing the DMS as a critical hub for motor control and a promising target for neuromodulation therapy [147] [148].

Therefore, we selected locomotor behavior as the experimental readout in our study. E-cadherin or Ctrl viruses were delivered into the DMS of mice (Fig. 26A). Fluorescence imaging at 3 weeks post-injection confirmed E-cadherin expression in DMS (Fig. 26A). A miniature US adapter was installed directly above the corresponding skull at the virus injection site (Fig. 26A). After 1 week of adaptation, the mice were placed in a cylindrical arena with a diameter of 30 cm (with bedding at the bottom) for 30 minutes of adaptation and then subjected to US stimulation (0.8 MHz, 1 kHz PRF, 50% duty cycle, 300 ms duration, 5 s interval). A high-speed camera was used to record the mouse's movement behavior throughout the process (Fig. 26B).

Behavioral analysis showed that both groups of mice were almost stationary before US stimulation (2.9-4.4 mm/s) (Fig. 26C, D). However, applying 0.45 MPa US significantly enhanced the motor activity of the E-cadherin group, with a mobile average speed of 31.8 ±3.2 mm/s, significantly higher than 10.4 ± 3.3 mm/s in the Ctrl group (Fig. 26E). The total movement distance was nearly 5 times that of the Ctrl group (Fig. 26C - F). Notably, after cessation of US, the movement speed of mice from both groups rapidly decreased until they finally stopped (Fig. 26D). Upon increasing acoustic intensity to 0.65 MPa, the movement of both groups increased, showing that the US-induced movement was dose-dependent upon the acoustic intensity delivered (20.8 ± 5.6 mm/s in the Ctrl group vs 43.1 ± 6.6 mm/s in the E-cadherin group; Fig. 26E, F). Crucially, however, both the speed and total distance travelled by mice in the E-cadherin group was significantly higher than those of Ctrl mice at all US intensities tested, underscoring again the sonogenetic enhancement effect shown by E-cadherin expression in our experiments.

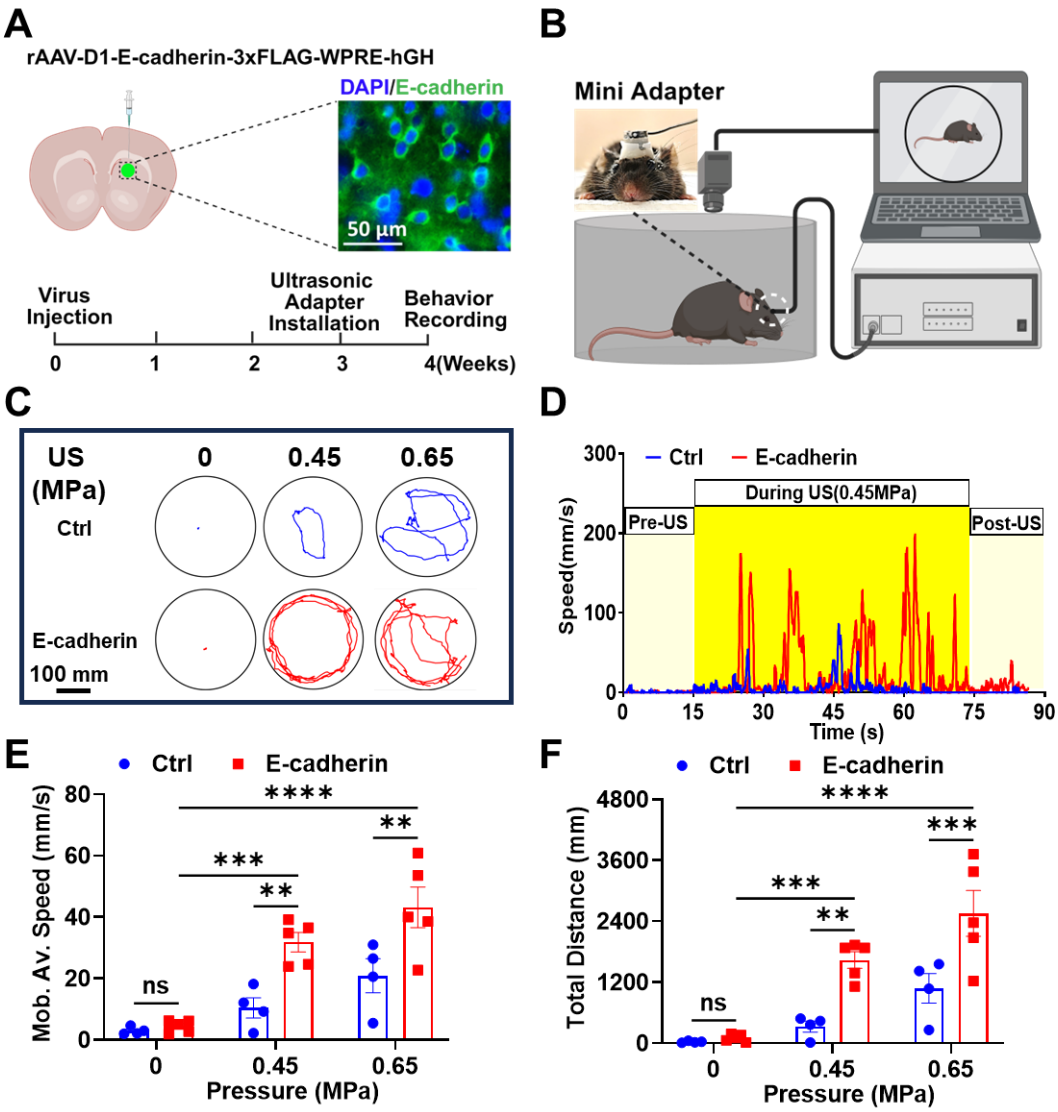

Figure 26. E-cadherin modulates ultrasound-induced motor behaviors. **(A)** Explanation of our locomotor experimental scheme. Top: Mice were injected with either AAV-D1-E-cadherin or AAV-D1-MCS (Ctrl) viruses in the right dorsal striatum (DMS) targeting dopamine D1-neuron. Fluorescence imaging shows E-cadherin (green) and DAPI (blue) in the DMS. Bottom: Three weeks after the virus injection, a mini head adapter was implanted above the injection site on the skull. After a 1-week habituation period, high-speed video recording was performed to record locomotor behavior. **(B)** Schematic of the high-speed behavioral recording setup at week 4: An US probe (0.8 MHz) was embedded in the miniature head adapter, coupled with US gel. Mice were placed in a cylindrical open field for 20 min of acclimation, followed by US stimulation (0.8 MHz, 1 kHz PRF, 50% duty cycle, 300 ms duration, 5 s interval). **(C)** The

movement traces of representative E-cadherin/Ctrl mice in 1 minute under varying US intensities in an open-field arena. US stimulation was sequentially applied at intensities of 0, 0.45, and 0.65 MPa, with each stimulus lasting 1 min and separated by 1-min intervals. **(D)** Real-time velocity of E-cadherin/Ctrl mice pre-, during, and post-US stimulation (0.45 MPa). The mobile average speed of **(E)** and total distance traveled by **(F)** E-cadherin and Ctrl mice with 0, 0.45, 0.65 MPa US. n for Ctrl = 4, E-cadherin = 5. mean ± SEM shown; **P < 0.01, ***P < 0.001, ****P < 0.0001 by two-way ANOVA with Tukey's test.

6.2.2 Upregulation of neuronal activation markers in DMS of E-cadherin mice after US stimulation

To determine whether the observed behavioral changes were related to the activation of neurons in the DMS, the brains of US-treated mice were collected 90 minutes after US stimulation for c-Fos immunostaining. We found that following 0.45 MPa US stimulation, the percentage of c-Fos$^+$ neurons in the DMS of the E-cadherin group was significantly higher than that in the Ctrl group (E-cadherin = 13.9% ± 4.9% vs Ctrl = 2.4% ± 0.3%), while both groups remained at the baseline level (<4.5%) under unstimulated conditions (Fig. 27A, B). Thus, we found that the E-cadherin group showed a significantly elevated level of neuronal activation in the DMS following US, as well as significantly increased locomotor behavior. These results demonstrate, from the molecular to the behavioral level, that E-cadherin can effectively mediate the sonogenetic activation of striatal neurons to precisely regulate mouse motor behaviors.

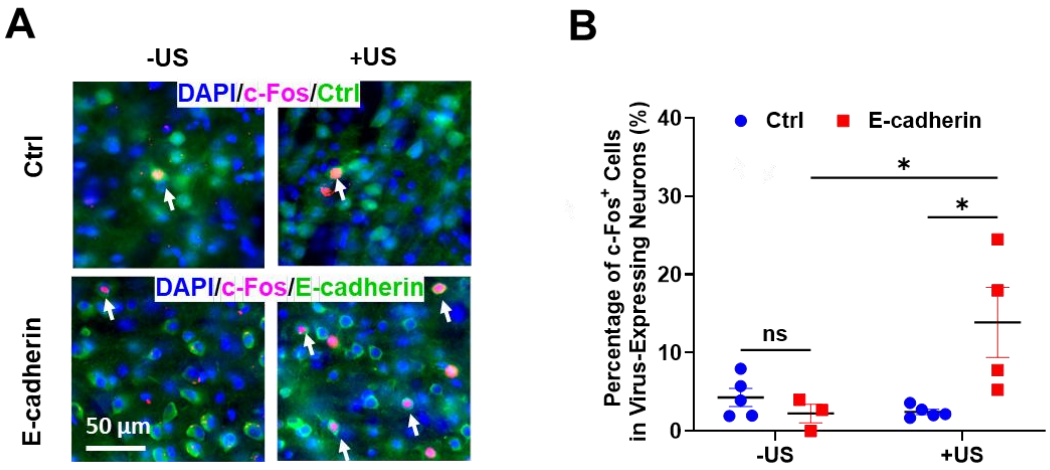

Figure 27. E-cadherin mediates ultrasound-induced c-Fos activation in mouse DMS brain region. (A) Representative immunofluorescence images in the DMS, with or without US stimulation. c-Fos (red), Ctrl/E-cadherin (green) and DAPI (blue), **(B)** Quantification of percentage of c-Fos$^+$ cells in the groups shown in **(A)**. The percentage of c-Fos$^+$ cells in virus-expressing neurons was quantified in at least three brain sections for each mouse, with each point n representing the mean value per mouse. mean ± SEM shown; *P < 0.05 by two-way ANOVA with Tukey's test. Ctrl

CHAPTER 7 Conclusions and future perspectives

This study systematically screened non-ion channel mechanosensitive molecules by combining ultrasonic stimulation with calcium imaging, revealing for the first time the potential of E-cadherin as an optimal non-ion channel mechanosensitive molecule in mediating sonogenetic regulation. *In vitro* experiments demonstrated that HEK293T cells expressing E-cadherin exhibited stronger ultrasound-induced calcium responses compared to cells expressing other proteins (integrin β2, VEGFR2, or GPCR68). Notably, E-cadherin, as a non-ion channel protein, lacks the intrinsic ability to mediate calcium ion transmembrane flux [149]. Intriguingly, when E-cadherin was co-transfected with mechanosensitive channels (Piezo1, TRPC1, or TRPA1) in CHO cells (which barely express endogenous mechanosensitive channels), we found that E-cadherin could enhance the responsiveness of Piezo1 to ultrasonic stimulation, thereby mediating sonogenetic regulation. Importantly, Piezo1, as a mechanosensitive channel, is widely expressed in brain tissue [150]. In primary cortical neurons, E-cadherin expression significantly increased neuronal responsiveness to US and induced c-fos upregulation. In anesthetized mice, E-cadherin expression markedly enhanced calcium responses in excitatory neurons of the motor cortex (M1) to ultrasound, accompanied by contralateral forelimb twitching. In freely moving mice, E-cadherin expression in the striatum significantly potentiated ultrasound-induced locomotor behaviors. These results establish E-cadherin as a novel sonogenetic tool that enables efficient neuromodulation without relying on genetic modification of traditional MSCs, thereby advancing ultrasound-mediated neuromodulation technologies.

7.1 Advantages of non-channel protein-mediated ultrasonic neuromodulation

The paradigm of non-channel protein-mediated ultrasonic neuromodulation expands the sonogenetic toolbox and offers several potential advantages: First, current sonogenetic techniques primarily depend on genetic modification of MSCs (e.g., Piezo1) in target cells [74]. However, some channel proteins are too large for efficient neuronal overexpression and may exhibit off-target effects. E-cadherin, as an ideal alternative, circumvents these limitations. Second, co-expression of mechanosensitive ion channels and non-channel proteins may produce synergistic effects—not only enhancing cellular sensitivity to US (e.g., stronger ultrasound-induced calcium responses were observed with Piezo1 and E-cadherin co-transfection compared to Piezo1 alone) but also reducing interference with normal cellular physiology by lowering the expression level of a single channel.

Finally, unlike optogenetics, which strictly relies on light-sensitive proteins [151], ultrasound's unique mechanical wave properties enable activation of a broader spectrum of mechanosensitive molecules, providing a distinct advantage for large-scale screening of novel regulatory molecules.

7.2 Large-scale screening and optimization of non-Ion channel proteins

The development of ultrasonic neuromodulation technologies offers new possibilities for treating neurological disorders. As a non-invasive stimulation method with deep tissue penetration, US exhibits unique advantages in neuromodulation. To improve the specificity of US stimulation for target cells or regions, researchers have explored various enhancement strategies, including biomaterials [152-155] and

mechanosensitive ion channels [73, 74, 87, 89-94]. This study identified E-cadherin as a key enhancer of cellular responsiveness to ultrasound. As a critical cell adhesion molecule, E-cadherin mediates mechanical signal transduction and participates in diverse physiological processes [114]. Although E-cadherin expression did not cause significant abnormalities in neuronal spontaneous activity or immune responses, indicating good biosafety, its long-term effects on synaptic plasticity, neural network activity, and *in vivo* behavior require further validation. Moreover, while this study focused on motor cortex neuromodulation, future work should assess the generalizability of E-cadherin in other brain regions (e.g., hippocampus, amygdala), as differences in cell subtypes and microenvironments may influence E-cadherin-dependent US responses.

Subsequent studies should prioritize optimizing E-cadherin expression strategies, including the selection of tissue-specific promoters and precise control of expression levels. Additionally, elucidating the molecular mechanisms underlying E-cadherin-mediated US responses—such as downstream signaling pathways and effector molecules—is essential. Given that US vibrations may interfere with traditional electrophysiological recordings (e.g., patch-clamp), developing interference-resistant recording methods (e.g., high-resolution voltage probes or molecular sensors) is necessary to comprehensively analyze dynamic molecular changes. Molecular biology approaches could also clarify the structural basis of E-cadherin mechanotransduction.

This study screened four widely reported non-channel membrane proteins responsive to mechanical stimuli (shear force) using calcium imaging, identifying E-cadherin as the optimal sonogenetic regulator. Given its safety and efficacy, future large-scale screening of non-channel proteins could identify even more effective candidates. Notably, beyond membrane proteins, other ultrasound-responsive molecules (e.g., transcription factors) may serve as potential sonogenetic elements [156].

7.3 Optimization of US stimulation parameters

In cellular experiments, combining US stimulation with calcium imaging and the intracellular calcium probe Fura-2, we observed that E-cadherin-expressing primary cortical neurons exhibited significantly elevated ultrasound-induced calcium signals, whereas most cells in the Ctrl group showed weak responses. Increasing US intensity enhanced both the number of responsive neurons and the amplitude of calcium signals. *In vivo*, integrating US stimulation with fiber photometry and the genetically encoded calcium indicator GCaMP6s revealed that E-cadherin activation in the motor cortex (M1) of lightly anesthetized mice elicited robust calcium transients in excitatory neurons, whereas Ctrl mice displayed minimal responses. Higher US intensities also increased calcium signal amplitudes, consistent with prior *in vitro* findings [74, 87]. In anesthetized Ctrl mice, high-intensity US evoked limb twitching with latencies (100–200 ms) matching our earlier data [91], suggesting potential activation of endogenous mechanosensitive channels like Piezo1 [72] or TRPV1 [157]. Thus, low-intensity stimulation or shorter durations may improve specificity.

Existing studies indicate that optimizing intensity, frequency, duration, and intervals can minimize thermal effects [68, 158]. Our *in vivo* parameters (0.8 MHz, 1 kHz PRF, 50% duty cycle, 300 ms duration, 5 s interval, peak intensity 0.65 MPa) theoretically raised brain tissue temperature by <2°C, below the thermal damage threshold. Given variations in neuronal subtypes and brain region depths, systematic exploration of parameter space is needed to refine sonogenetic protocols for higher efficiency.

7.4 Potential applications of co-expressing MSCs and non-ion channel proteins in sonogenetics

The successful application of E-cadherin-based sonogenetics in mammals validates a key proof of concept: systematic screening of non-channel mechanosensitive molecules can yield effective neuromodulatory tools. This strategy opens multiple promising avenues for basic and clinical research. In neuroscience, E-cadherin-mediated sonogenetics could elucidate novel neural circuits. For translational development, synergistic effects between E-cadherin and existing MSC methods may inspire combination therapies for Parkinson's disease, depression, and other neurological disorders. Future work should focus on (1) establishing high-throughput screening platforms to discover safer, more efficient sonogenetic molecules and (2) exploring clinical translation pathways for non-channel protein-mediated ultrasonic neuromodulation, particularly for deep brain regions (e.g., basal ganglia). These advances will propel sonogenetics from bench to bedside, offering breakthroughs in neurological disease treatment.

7.5 Cross-Species applicability and developmental stage-specific Regulation

While the current study has validated the efficacy of E-cadherin-mediated sonogenetic modulation in rodent models, its applicability in higher mammals (e.g., non-human primates) remains to be systematically evaluated. Cross-species differences may influence the ultimate effectiveness of E-cadherin-mediated sonogenetic regulation, necessitating comparative studies on ultrasound response thresholds and kinetic characteristics in neurons from different species following E-cadherin genetic modification.

Additionally, the expression and function of mechanosensitive channels in mammalian neurons vary across developmental stages. Given that E-cadherin-mediated sonogenetic regulation relies on mechanosensitive channels for its effects, future research should investigate the stage-specific roles of E-cadherin-dependent ultrasonic neuromodulation in animals of different ages. This exploration may provide novel insights into interventions for developmental neurological disorders.

References:

1. Herculano-Houzel, S., *The remarkable, yet not extraordinary, human brain as a scaled-up primate brain and its associated cost.* Proc Natl Acad Sci U S A, 2012. **109 Suppl 1**(Suppl 1): p. 10661-8.
2. Lotharius, J. and P. Brundin, *Pathogenesis of Parkinson's disease: dopamine, vesicles and alpha-synuclein.* Nat Rev Neurosci, 2002. **3**(12): p. 932-42.
3. Theodore, W.H. and R.S. Fisher, *Brain stimulation for epilepsy.* Lancet Neurol, 2004. **3**(2): p. 111-8.
4. Martin, J.L., et al., *Transcranial magnetic stimulation for treating depression.* Cochrane Database Syst Rev, 2002. **2002**(2): p. Cd003493.
5. Groiss, S.J., et al., *Deep brain stimulation in Parkinson's disease.* Ther Adv Neurol Disord, 2009. **2**(6): p. 20-8.
6. Flora, E.D., et al., *Deep brain stimulation for essential tremor: a systematic review.* Mov Disord, 2010. **25**(11): p. 1550-9.
7. Gabriëls, L., et al., *Deep brain stimulation for treatment-refractory obsessive-compulsive disorder: psychopathological and neuropsychological outcome in three cases.* Acta Psychiatr Scand, 2003. **107**(4): p. 275-82.
8. Jankovic, J., *Complications and limitations of drug therapy for Parkinson's disease.* Neurology, 2000. **55**(12 Suppl 6): p. S2-6.
9. Breit, S., J.B. Schulz, and A.L. Benabid, *Deep brain stimulation.* Cell Tissue Res, 2004. **318**(1): p. 275-88.
10. Lozano, A.M., et al., *Deep brain stimulation: current challenges and future directions.* Nat Rev Neurol, 2019. **15**(3): p. 148-160.
11. Temel, Y., et al., *Deep brain stimulation of the thalamus can influence penile erection.* Int J Impot Res, 2004. **16**(1): p. 91-4.

12. Filali, M., et al., *Stimulation-induced inhibition of neuronal firing in human subthalamic nucleus.* Exp Brain Res, 2004. **156**(3): p. 274-81.

13. Batsikadze, G., et al., *Effects of cerebellar transcranial direct current stimulation on cerebellar-brain inhibition in humans: A systematic evaluation.* Brain Stimul, 2019. **12**(5): p. 1177-1186.

14. Ciechanski, P. and A. Kirton, *Transcranial Direct-Current Stimulation Can Enhance Motor Learning in Children.* Cereb Cortex, 2017. **27**(5): p. 2758-2767.

15. Orrù, G., et al., *Motor stroke recovery after tDCS: a systematic review.* Rev Neurosci, 2020. **31**(2): p. 201-218.

16. Palm, U., et al., *tDCS for the treatment of depression: a comprehensive review.* Eur Arch Psychiatry Clin Neurosci, 2016. **266**(8): p. 681-694.

17. De Smet, S., et al., *Determinants of sham response in tDCS depression trials: a systematic review and meta-analysis.* Prog Neuropsychopharmacol Biol Psychiatry, 2021. **109**: p. 110261.

18. Woodham, R., et al., *Is tDCS a potential first line treatment for major depression?* Int Rev Psychiatry, 2021. **33**(3): p. 250-265.

19. Brunoni, A.R., et al., *Understanding tDCS effects in schizophrenia: a systematic review of clinical data and an integrated computation modeling analysis.* Expert Rev Med Devices, 2014. **11**(4): p. 383-94.

20. Caiani, G., et al., *Anatomical Characteristics Predict Response to Transcranial Direct Current Stimulation (tDCS): Development of a Computational Pipeline for Optimizing tDCS Protocols.* Bioengineering (Basel), 2025. **12**(6).

21. Poreisz, C., et al., *Safety aspects of transcranial direct current stimulation concerning healthy subjects and patients.* Brain Res Bull, 2007. **72**(4-6): p. 208-14.

22. Grover, S., et al., *A meta-analysis suggests that tACS improves cognition in healthy, aging, and psychiatric populations.* Sci Transl Med, 2023. **15**(697): p. eabo2044.

23. Nissim, N.R., et al., *The impact of gamma transcranial alternating current stimulation (tACS) on cognitive and memory processes in patients with mild cognitive impairment or Alzheimer's disease: A literature review.* Brain Stimul, 2023. **16**(3): p. 748-755.

24. Motamedi, G.K., et al., *Transcranial Alternating Current Stimulation (tACS) as a Treatment for Insomnia.* Can J Neurol Sci, 2023. **50**(3): p. 446-449.

25. Zhou, J., et al., *Effect of add-on transcranial alternating current stimulation (tACS) in major depressive disorder: A randomized controlled trial.* Brain Stimul, 2024. **17**(4): p. 760-768.

26. Haslacher, D., et al., *In vivo phase-dependent enhancement and suppression of human brain oscillations by transcranial alternating current stimulation (tACS).* Neuroimage, 2023. **275**: p. 120187.

27. Klomjai, W., R. Katz, and A. Lackmy-Vallée, *Basic principles of transcranial magnetic stimulation (TMS) and repetitive TMS (rTMS).* Ann Phys Rehabil Med, 2015. **58**(4): p. 208-213.

28. Sonmez, A.I., et al., *Accelerated TMS for Depression: A systematic review and meta-analysis.* Psychiatry Res, 2019. **273**: p. 770-781.

29. Koutsomitros, T., et al., *Advances in transcranial magnetic stimulation (TMS) and its applications in resistant depression.* Psychiatriki, 2021. **32**(Supplement I): p. 90-98.

30. Hamid, P., B.H. Malik, and M.L. Hussain, *Noninvasive Transcranial Magnetic Stimulation (TMS) in Chronic Refractory Pain: A Systematic Review.* Cureus,

2019. **11**(10): p. e6019.

31. Bai, Z., J. Zhang, and K.N.K. Fong, *Effects of transcranial magnetic stimulation in modulating cortical excitability in patients with stroke: a systematic review and meta-analysis.* J Neuroeng Rehabil, 2022. **19**(1): p. 24.

32. Li, R., et al., *Enhancing the effects of transcranial magnetic stimulation with intravenously injected magnetic nanoparticles.* Biomater Sci, 2019. **7**(6): p. 2297-2307.

33. Lee, J.U., et al., *Non-contact long-range magnetic stimulation of mechanosensitive ion channels in freely moving animals.* Nat Mater, 2021. **20**(7): p. 1029-1036.

34. Stultz, D.J., et al., *Transcranial Magnetic Stimulation (TMS) Safety with Respect to Seizures: A Literature Review.* Neuropsychiatr Dis Treat, 2020. **16**: p. 2989-3000.

35. Martinez-Nunez, A.E., et al., *Emerging therapies for neuromodulation in Parkinson's disease*. Neurotherapeutics. 2023 Dec 28;21(3):e00310. doi: 10.1016/j.neurot.2023.e00310. eCollection 2024 Apr.

36. Boyden, E.S., et al., *Millisecond-timescale, genetically targeted optical control of neural activity.* Nat Neurosci, 2005. **8**(9): p. 1263-8.

37. Liu, X., et al., *Optogenetic stimulation of a hippocampal engram activates fear memory recall.* Nature, 2012. **484**(7394): p. 381-5.

38. Warlow, S.M., E.E. Naffziger, and K.C. Berridge, *The central amygdala recruits mesocorticolimbic circuitry for pursuit of reward or pain.* Nat Commun, 2020. **11**(1): p. 2716.

39. Xu, M., et al., *Basal forebrain circuit for sleep-wake control.* Nat Neurosci, 2015. **18**(11): p. 1641-7.

40. Valverde, S., et al., *Deep brain stimulation-guided optogenetic rescue of parkinsonian symptoms.* Nat Commun, 2020. **11**(1): p. 2388.

41. Bentley, J.N., et al., *Optogenetics in epilepsy.* Neurosurg Focus, 2013. **34**(6): p. E4.

42. Osawa, S.I. and T. Tominaga, *Application of Optogenetics in Epilepsy Research.* Adv Exp Med Biol, 2021. **1293**: p. 557-562.

43. Busskamp, V., B. Roska, and J.A. Sahel, *Optogenetic Vision Restoration.* Cold Spring Harb Perspect Med, 2024. **14**(8).

44. Chen, Z., et al., *Wireless Optogenetic Modulation of Cortical Neurons Enabled by Radioluminescent Nanoparticles.* ACS Nano, 2021. **15**(3): p. 5201-5208.

45. Inglut, C.T., et al., *Predictors and Limitations of the Penetration Depth of Photodynamic Effects in the Rodent Brain.* Photochem Photobiol, 2020. **96**(2): p. 301-309.

46. Zhang, Q., et al., *Application of Optogenetics in Neurodegenerative Diseases.* Cell Mol Neurobiol, 2024. **44**(1): p. 57.

47. Urban, D.J. and B.L. Roth, *DREADDs (designer receptors exclusively activated by designer drugs): chemogenetic tools with therapeutic utility.* Annu Rev Pharmacol Toxicol, 2015. **55**: p. 399-417.

48. Florido, A., et al., *Sex differences in neural projections of fear memory processing in mice and humans.* Sci Adv, 2024. **10**(28): p. eadk3365.

49. Robinson, H.L., et al., *Comparison of three DREADD agonists acting on Gq-DREADDs in the ventral tegmental area to alter locomotor activity in tyrosine hydroxylase:Cre male and female rats.* Behav Brain Res, 2023. **455**: p. 114674.

50. Hare, B.D. and R.S. Duman, *Prefrontal cortex circuits in depression and anxiety: contribution of discrete neuronal populations and target regions.* Mol Psychiatry,

2020. **25**(11): p. 2742-2758.

51. Muir, J., J. Lopez, and R.C. Bagot, *Wiring the depressed brain: optogenetic and chemogenetic circuit interrogation in animal models of depression.* Neuropsychopharmacology, 2019. **44**(6): p. 1013-1026.

52. Roth, B.L., *DREADDs for Neuroscientists.* Neuron, 2016. **89**(4): p. 683-94.

53. Woodcock, J.P., *Doppler ultrasound in clinical diagnosis.* Br Med Bull, 1980. **36**(3): p. 243-8.

54. Kooiman, K., et al., *Ultrasound-Responsive Cavitation Nuclei for Therapy and Drug Delivery.* Ultrasound Med Biol, 2020. **46**(6): p. 1296-1325.

55. Church, C.C., *Thermal dose and the probability of adverse effects from biomedical ultrasound.* The Journal of the Acoustical Society of America, 2006. **119**(5_Supplement): p. 3376-3376.

56. ter Haar, G., *High Intensity Focused Ultrasound for Cancer Therapy—harnessing its non-linearity.* AIP Conference Proceedings, 2008. **1022**(1): p. 427-431.

57. ter Haar, G., *Ultrasound bioeffects and safety.* Proc Inst Mech Eng H, 2010. **224**(2): p. 363-73.

58. Miller, D.L., *Overview of experimental studies of biological effects of medical ultrasound caused by gas body activation and inertial cavitation.* Prog Biophys Mol Biol, 2007. **93**(1-3): p. 314-30.

59. Li, S., G.S.P. Mok, and Y. Dai, *Lipid bilayer-based biological nanoplatforms for sonodynamic cancer therapy.* Adv Drug Deliv Rev, 2023. **202**: p. 115110.

60. Apfel, R.E., *Sonic effervescence: A tutorial on acoustic cavitation.* The Journal of the Acoustical Society of America, 1997. **101**(3): p. 1227-1237.

61. Jiang, Z., W. Xiao, and Q. Fu, *Stimuli responsive nanosonosensitizers for sonodynamic therapy.* J Control Release, 2023. **361**: p. 547-567.

62. Duncan, B., et al., *Ultrasound-Mediated Ocular Drug Delivery: From Physics and Instrumentation to Future Directions.* Micromachines (Basel), 2023. **14**(8).

63. Liu, Q., et al., *The effect of low frequency and low intensity ultrasound combined with microbubbles on the sonoporation efficiency of MDA-MB-231 cells.* Ann Transl Med, 2020. **8**(6): p. 298.

64. Lum, I., et al., *Effects of superimposed ultrasound on deformation of gold.* Journal of Applied Physics, 2009. **105**(2): p. 024905.

65. Liu, X., et al., *Review of Noninvasive or Minimally Invasive Deep Brain Stimulation.* Front Behav Neurosci, 2021. **15**: p. 820017.

66. Quarato, C.M.I., et al., *A Review on Biological Effects of Ultrasounds: Key Messages for Clinicians.* Diagnostics (Basel), 2023. **13**(5).

67. Shankar, H. and P.S. Pagel, *Potential adverse ultrasound-related biological effects: a critical review.* Anesthesiology, 2011. **115**(5): p. 1109-24.

68. Tyler, W.J., et al., *Remote excitation of neuronal circuits using low-intensity, low-frequency ultrasound.* PLoS One, 2008. **3**(10): p. e3511.

69. Khraiche, M.L., et al., *Ultrasound induced increase in excitability of single neurons.* Annu Int Conf IEEE Eng Med Biol Soc, 2008. **2008**: p. 4246-9.

70. Lee, J., et al., *A MEMS ultrasound stimulation system for modulation of neural circuits with high spatial resolution in vitro.* Microsyst Nanoeng, 2019. **5**: p. 28.

71. Coste, B., et al., *Piezo proteins are pore-forming subunits of mechanically activated channels.* Nature, 2012. **483**(7388): p. 176-81.

72. Zhu, J., et al., *The mechanosensitive ion channel Piezo1 contributes to ultrasound neuromodulation.* Proc Natl Acad Sci U S A, 2023. **120**(18): p. e2300291120.

73. Sorum, B., et al., *Ultrasound activates mechanosensitive TRAAK K(+) channels through the lipid membrane.* Proc Natl Acad Sci U S A, 2021. **118**(6).

74. Qiu, Z., et al., *The Mechanosensitive Ion Channel Piezo1 Significantly Mediates In Vitro Ultrasonic Stimulation of Neurons.* iScience, 2019. **21**: p. 448-457.

75. Qi, L., et al., *Low-intensity focused ultrasound stimulation promotes stroke recovery via astrocytic HMGB1 and CAMK2N1 in mice.* Stroke Vasc Neurol, 2024. **9**(5): p. 505-518.

76. Zhong, Y.X., et al., *Low intensity focused ultrasound: a new prospect for the treatment of Parkinson's disease.* Ann Med, 2023. **55**(2): p. 2251145.

77. Lee, W., et al., *Image-Guided Focused Ultrasound-Mediated Regional Brain Stimulation in Sheep.* Ultrasound Med Biol, 2016. **42**(2): p. 459-70.

78. Dallapiazza, R.F., et al., *Noninvasive neuromodulation and thalamic mapping with low-intensity focused ultrasound.* J Neurosurg, 2018. **128**(3): p. 875-884.

79. Folloni, D., et al., *Ultrasound modulation of macaque prefrontal cortex selectively alters credit assignment-related activity and behavior.* Sci Adv, 2021. **7**(51): p. eabg7700.

80. Legon, W., et al., *Transcranial focused ultrasound neuromodulation of the human primary motor cortex.* Sci Rep, 2018. **8**(1): p. 10007.

81. Lee, W., et al., *Transcranial focused ultrasound stimulation of human primary visual cortex.* Sci Rep, 2016. **6**: p. 34026.

82. Sanguinetti, J.L., et al., *Transcranial Focused Ultrasound to the Right Prefrontal Cortex Improves Mood and Alters Functional Connectivity in Humans.* Front Hum Neurosci, 2020. **14**: p. 52.

83. Hameroff, S., et al., *Transcranial ultrasound (TUS) effects on mental states: a pilot study.* Brain Stimul, 2013. **6**(3): p. 409-15.

84. Meng, Y., et al., *Is there a role for MR-guided focused ultrasound in Parkinson's disease?* Mov Disord, 2018. **33**(4): p. 575-579.

85. Tyler, W.J., S.W. Lani, and G.M. Hwang, *Ultrasonic modulation of neural circuit activity.* Curr Opin Neurobiol, 2018. **50**: p. 222-231.

86. Xu, K., et al., *TRPV1-mediated sonogenetic neuromodulation of motor cortex in freely moving mice.* J Neural Eng, 2023. **20**(1).

87. Yoo, S., et al., *Focused ultrasound excites cortical neurons via mechanosensitive calcium accumulation and ion channel amplification.* Nat Commun, 2022. **13**(1): p. 493.

88. Ibsen, S., et al., *Sonogenetics is a non-invasive approach to activating neurons in Caenorhabditis elegans.* Nat Commun, 2015. **6**: p. 8264.

89. Huang, Y.S., et al., *Sonogenetic Modulation of Cellular Activities Using an Engineered Auditory-Sensing Protein.* Nano Lett, 2020. **20**(2): p. 1089-1100.

90. Ye, J., et al., *Ultrasonic Control of Neural Activity through Activation of the Mechanosensitive Channel MscL.* Nano Lett, 2018. **18**(7): p. 4148-4155.

91. Qiu, Z., et al., *Targeted Neurostimulation in Mouse Brains with Non-invasive Ultrasound.* Cell Rep, 2020. **32**(7): p. 108033.

92. Sorum, B., et al., *Tension activation of mechanosensitive two-pore domain K+ channels TRAAK, TREK-1, and TREK-2.* Nat Commun, 2024. **15**(1): p. 3142.

93. Sorum, B., et al., *Pressure and ultrasound activate mechanosensitive TRAAK K (+) channels through increased membrane tension.* bioRxiv, 2023.

94. Duque, M., et al., *Sonogenetic control of mammalian cells using exogenous Transient Receptor Potential A1 channels.* Nat Commun, 2022. **13**(1): p. 600.

95. Roeterink, R.M.A., et al., *Force versus Response: Methods for Activating and Characterizing Mechanosensitive Ion Channels and GPCRs.* Adv Healthc Mater, 2024. **13**(31): p. e2402167.

96. Syntichaki, P. and N. Tavernarakis, *Genetic models of mechanotransduction: the*

nematode Caenorhabditis elegans. Physiol Rev, 2004. **84**(4): p. 1097-153.

97. Mao, L., et al., *The role of integrin family in bone metabolism and tumor bone metastasis.* Cell Death Discov, 2023. **9**(1): p. 119.

98. Wen, L., M. Moser, and K. Ley, *Molecular mechanisms of leukocyte β2 integrin activation.* Blood, 2022. **139**(24): p. 3480-3492.

99. Morikis, V.A., et al., *β(2)-Integrin Adhesive Bond Tension under Shear Stress Modulates Cytosolic Calcium Flux and Neutrophil Inflammatory Response.* Cells, 2022. **11**(18).

100. Zhou, X., J. Li, and D.F. Kucik, *The microtubule cytoskeleton participates in control of beta2 integrin avidity.* J Biol Chem, 2001. **276**(48): p. 44762-9.

101. Ezzo, M. and B. Hinz, *Novel approaches to target fibroblast mechanotransduction in fibroproliferative diseases.* Pharmacol Ther, 2023. **250**: p. 108528.

102. Salzer, I., et al., *Nociceptor Signalling through ion Channel Regulation via GPCRs.* Int J Mol Sci, 2019. **20**(10).

103. Xu, J., et al., *GPR68 Senses Flow and Is Essential for Vascular Physiology.* Cell, 2018. **173**(3): p. 762-775.e16.

104. Ji, R., et al., *Proton-sensing ion channels, GPCRs and calcium signaling regulated by them: implications for cancer.* Front Cell Dev Biol, 2024. **12**: p. 1326231.

105. He, X., et al., *GPR68 supports AML cells through the calcium/calcineurin pro-survival pathway and confers chemoresistance by mediating glucose metabolic symbiosis.* Biochim Biophys Acta Mol Basis Dis, 2025. **1871**(1): p. 167565.

106. Shibuya, M., *Vascular endothelial growth factor (VEGF)-Receptor2: its biological functions, major signaling pathway, and specific ligand VEGF-E.* Endothelium, 2006. **13**(2): p. 63-9.

107. Shaw, P., et al., *VEGF signaling: Role in angiogenesis and beyond.* Biochim

Biophys Acta Rev Cancer, 2024. **1879**(2): p. 189079.

108. Abhinand, C.S., et al., *VEGF-A/VEGFR2 signaling network in endothelial cells relevant to angiogenesis.* J Cell Commun Signal, 2016. **10**(4): p. 347-354.

109. Jin, Z.G., et al., *Ligand-independent activation of vascular endothelial growth factor receptor 2 by fluid shear stress regulates activation of endothelial nitric oxide synthase.* Circ Res, 2003. **93**(4): p. 354-63.

110. de Castro, L.F., et al., *VEGF Receptor 2 (VEGFR2) Activation Is Essential for Osteocyte Survival Induced by Mechanotransduction.* J Cell Physiol, 2015. **230**(2): p. 278-85.

111. LaValley, D.J., et al., *Matrix Stiffness Enhances VEGFR-2 Internalization, Signaling, and Proliferation in Endothelial Cells.* Converg Sci Phys Oncol, 2017. **3**.

112. Tian, Y., et al., *Activation of Vascular Endothelial Growth Factor (VEGF) Receptor 2 Mediates Endothelial Permeability Caused by Cyclic Stretch.* J Biol Chem, 2016. **291**(19): p. 10032-45.

113. Vion, A.C., et al., *Endothelial Cell Orientation and Polarity Are Controlled by Shear Stress and VEGF Through Distinct Signaling Pathways.* Front Physiol, 2020. **11**: p. 623769.

114. Leckband, D.E. and J. de Rooij, *Cadherin adhesion and mechanotransduction.* Annu Rev Cell Dev Biol, 2014. **30**: p. 291-315.

115. Daulagala, A.C., M.C. Bridges, and A. Kourtidis, *E-cadherin Beyond Structure: A Signaling Hub in Colon Homeostasis and Disease.* Int J Mol Sci, 2019. **20**(11).

116. Raftopoulos, I. and G. Kouraklis, *Dysfunction of the E-cadherin/catenin cell adhesion cascade in epithelial cancers (Review).* Oncol Rep, 1996. **3**(4): p. 793-803.

117. Bhattacharyya, S., et al., *Cell-cell adhesions in embryonic stem cells regulate the stability and transcriptional activity of β-catenin.* FEBS Lett, 2022. **596**(13): p. 1647-1660.

118. Mège, R.M. and N. Ishiyama, *Integration of Cadherin Adhesion and Cytoskeleton at Adherens Junctions.* Cold Spring Harb Perspect Biol, 2017. **9**(5).

119. Schmalhofer, O., S. Brabletz, and T. Brabletz, *E-cadherin, beta-catenin, and ZEB1 in malignant progression of cancer.* Cancer Metastasis Rev, 2009. **28**(1-2): p. 151-66.

120. Labernadie, A., et al., *A mechanically active heterotypic E-cadherin/N-cadherin adhesion enables fibroblasts to drive cancer cell invasion.* Nat Cell Biol, 2017. **19**(3): p. 224-237.

121. Bush, M., et al., *An ensemble of flexible conformations underlies mechanotransduction by the cadherin-catenin adhesion complex.* Proc Natl Acad Sci U S A, 2019. **116**(43): p. 21545-21555.

122. Retailleau, K. and F. Duprat, *Polycystins and partners: proposed role in mechanosensitivity.* J Physiol, 2014. **592**(12): p. 2453-71.

123. Parker, E.M., et al., *Impacts of CACNB4 overexpression on dendritic spine density in both sexes and relevance to schizophrenia.* Transl Psychiatry, 2024. **14**(1): p. 484.

124. Bai, J., et al., *[Overexpression of TRPV1 after periphery nerve injury attenuates nerve regeneration in rats].* Zhonghua Bing Li Xue Za Zhi, 2017. **46**(12): p. 847-852.

125. Caterina, M.J., et al., *The capsaicin receptor: a heat-activated ion channel in the pain pathway.* Nature, 1997. **389**(6653): p. 816-24.

126. Giancotti, F.G. and E. Ruoslahti, *Integrin signaling.* Science, 1999. **285**(5430): p.

1028-32.

127. Balcioglu, H.E., et al., *The integrin expression profile modulates orientation and dynamics of force transmission at cell-matrix adhesions.* J Cell Sci, 2015. **128**(7): p. 1316-26.

128. Guo, Y., et al., *Nanotopographic micro-nano forces finely tune the conformation of macrophage mechanosensitive membrane protein integrin β(2) to manipulate inflammatory responses.* Nano Res, 2023: p. 1-15.

129. Miller, B. and M.K. Sewell-Loftin, *Mechanoregulation of Vascular Endothelial Growth Factor Receptor 2 in Angiogenesis.* Front Cardiovasc Med, 2021. **8**: p. 804934.

130. Tzima, E., et al., *A mechanosensory complex that mediates the endothelial cell response to fluid shear stress.* Nature, 2005. **437**(7057): p. 426-31.

131. Tian, G.E., et al., *Mechanoresponse of stem cells for vascular repair.* World J Stem Cells, 2019. **11**(12): p. 1104-1114.

132. Maneshi, M.M., et al., *Mechanical stress activates NMDA receptors in the absence of agonists.* Sci Rep, 2017. **7**: p. 39610.

133. Alenghat, F.J. and D.E. Ingber, *Mechanotransduction: all signals point to cytoskeleton, matrix, and integrins.* Sci STKE, 2002. **2002**(119): p. pe6.

134. Shafrir, Y. and G. Forgacs, *Mechanotransduction through the cytoskeleton.* Am J Physiol Cell Physiol, 2002. **282**(3): p. C479-86.

135. Janmey, P.A., *The cytoskeleton and cell signaling: component localization and mechanical coupling.* Physiol Rev, 1998. **78**(3): p. 763-81.

136. Lewis, A.H., et al., *Transduction of Repetitive Mechanical Stimuli by Piezo1 and Piezo2 Ion Channels.* Cell Rep, 2017. **19**(12): p. 2572-2585.

137. Delgado, R., et al., *Mechanical force activates the light-dependent channels TRP*

and TRPL in excised patches from the rhabdomere of Drosophila photoreceptors. Neuroscience, 2024. **555**: p. 23-31.

138. van Roy, F. and G. Berx, *The cell-cell adhesion molecule E-cadherin.* Cell Mol Life Sci, 2008. **65**(23): p. 3756-88.

139. Wang, J., et al., *Tethering Piezo channels to the actin cytoskeleton for mechanogating via the cadherin-β-catenin mechanotransduction complex.* Cell Rep, 2022. **38**(6): p. 110342.

140. Nieuwenhuis, B., et al., *Optimization of adeno-associated viral vector-mediated transduction of the corticospinal tract: comparison of four promoters.* Gene Ther, 2021. **28**(1-2): p. 56-74.

141. Sheng, M. and M.E. Greenberg, *The regulation and function of c-fos and other immediate early genes in the nervous system.* Neuron, 1990. **4**(4): p. 477-85.

142. Ghosh, A., et al., *Calcium regulation of gene expression in neuronal cells.* J Neurobiol, 1994. **25**(3): p. 294-303.

143. Griffin, D.M., D.S. Hoffman, and P.L. Strick, *Corticomotoneuronal cells are "functionally tuned".* Science, 2015. **350**(6261): p. 667-70.

144. King, R.L., J.R. Brown, and K.B. Pauly, *Localization of ultrasound-induced in vivo neurostimulation in the mouse model.* Ultrasound Med Biol, 2014. **40**(7): p. 1512-22.

145. Amalia, L., *Glial Fibrillary Acidic Protein (GFAP): Neuroinflammation Biomarker in Acute Ischemic Stroke.* J Inflamm Res, 2021. **14**: p. 7501-7506.

146. Hoogland, I.C., et al., *Systemic inflammation and microglial activation: systematic review of animal experiments.* J Neuroinflammation, 2015. **12**: p. 114.

147. Munshi, R., et al., *Magnetothermal genetic deep brain stimulation of motor behaviors in awake, freely moving mice.* Elife, 2017. **6**.

148. Yang, Y., et al., *Sonothermogenetics for noninvasive and cell-type specific deep brain neuromodulation.* Brain Stimul, 2021. **14**(4): p. 790-800.

149. Nagar, B., et al., *Structural basis of calcium-induced E-cadherin rigidification and dimerization.* Nature, 1996. **380**(6572): p. 360-4.

150. Zheng, Q., et al., *Mechanical properties of the brain: Focus on the essential role of Piezo1-mediated mechanotransduction in the CNS.* Brain Behav, 2023. **13**(9): p. e3136.

151. Towne, C. and K.R. Thompson, *Overview on Research and Clinical Applications of Optogenetics.* Curr Protoc Pharmacol, 2016. **75**: p. 11.19.1-11.19.21.

152. Tran, T.A., et al., *Characterization of cell membrane response to ultrasound activated microbubbles.* IEEE Trans Ultrason Ferroelectr Freq Control, 2008. **55**(1): p. 43-9.

153. Hou, X., et al., *Nanobubble-actuated ultrasound neuromodulation for selectively shaping behavior in mice.* Nat Commun, 2024. **15**(1): p. 2253.

154. Lea-Banks, H., et al., *Ultrasound-sensitive nanodroplets achieve targeted neuromodulation.* J Control Release, 2021. **332**: p. 30-39.

155. Scarcelli, T., et al., *Stimulation of hippocampal neurogenesis by transcranial focused ultrasound and microbubbles in adult mice.* Brain Stimul, 2014. **7**(2): p. 304-7.

156. Kim, H., et al., *Increased intracellular diffusivity of macromolecules within a mammalian cell by low-intensity pulsed ultrasound.* Ultrason Sonochem, 2023. **100**: p. 106644.

157. Storozhuk, M.V., O.F. Moroz, and A.V. Zholos, *Multifunctional TRPV1 Ion Channels in Physiology and Pathology with Focus on the Brain, Vasculature, and Some Visceral Systems.* Biomed Res Int, 2019. **2019**: p. 5806321.

158. O'Brien, W.D., Jr., *Ultrasound-biophysics mechanisms.* Prog Biophys Mol Biol, 2007. **93**(1-3): p. 212-55.